Modelling of PEMFC Catalyst Layer Mass Transport and Electro-Chemical Reactions Using Multi-scale Simulations

by

Philip Wardlaw

A thesis submitted in partial fulfillment of the requirements for the degree of

Master of Science

Department of Mechanical Engineering
University of Alberta

Abstract

The focus of this work is on improving understanding of mass transport limiting phenomena occurring within the micro-structure of Polymer Electrolyte Fuel Cell (PEFC) Catalyst Layers (CL). Micro-scale models, namely agglomerates, are employed within multi-scale CL framework, to examine many phenomena, such as the conductivity of protons in Nafion ionomer, non homogeneous catalyst distributions, oxygen dissolution in ionomer thin films, polydisperse agglomerate structures, and proton transport mechanisms within water filled carbon porous media. Catalyst distribution within CL micro structures, oxygen dissolution in Nafion described as a non-equilibrium process, and the mechanism by which protons are transported within water filled carbon pores are all found to be significant and potential explanations for PEMFC mass transport limited behaviour. The developed simulation framework presented in this work, as part of OpenFCST, the Open source Fuel Cell Simulations Toolbox, can be used in conjunction with experimental methods to improve understanding of said phenomena, improving understanding and design of PEMFCs.

Keywords: polymer electrolyte fuel cells, finite element method, open-source, simulation, membrane electrode assembly, multi-scale, micro structure, agglomerates

To my parents for their eternal love and support.

Acknowledgements

I would like to thank my supervisor Dr. Marc Secanell for the opportunity to pursue research of cutting edge technologies. His guidance, time and support were invaluable throughout the course of this work. His teachings on electrochemistry, mathematics, philosophy, and programming have been amongst my most valuable lessons so far, shaping the scientific method that I will use throughout the rest of my life.

I would like to thanks my parents for their eternal love, support, and encouragement in everything I do. Thank you for supporting me in all my endeavours, and encouraging me to achieve something great.

I would like to thank Kailyn Domican, for his companionship and cooperation over the last two years. Having someone to share the journey with has made everything easier and more enjoyable.

I would like to thank Derek Paxman, for his companionship. Our light hearted conversations helped keep the work place an enjoyable environment.

I would like to thank all the members of the ESDL for their support and friendship, specifically Madhur Bhaiya, Michael Moore, Valentin Zingan, and Shantanu Shukla for generously taking time to help me understand many things.

I would like to Acknowledge the financial support of the Automotive Fuel Cell Corporation (AFCC) and the Catalysis Research for Polymer Electrolyte Fuel Cells Network (CARPE-FC).

Table of Contents

List of Tables

List of Figures

Nomenclature

English Letters

ϕ	Potential, V
ϕ_m	Membrane/electrolyte potential, V
ϕ_s	Solid potential, V
$\vec{v}$	Velocity, m/s
A_v	Active catalyst surface area per unit volume, cm^2/cm^3
a_w	Activity of water
$A_{v,\,i}$	Graded active catalyst area, cm^2/cm^3
$A_{v,agg}$	Active area per volume of agglomerate, cm^2/cm^3
C_i	Ratio of concentration of species i with reference concentration of species i
c_i	Concentration of species i, mol/cm^3
D_{ij}	Binary diffusion coefficient for species i in species j, cm^2/s
E	Cell potential, V
e	Electron volt, V
E^{eq}	Equilibrium potential, V
E_r	Effectiveness factor of a porous particle
E_{rev}	Reversible cell potential, V
EW	Effective weight, g/mol
F	Faraday's constant, 96485.3365 C/mol

$H_{i,j}$ Henry's coefficient of gaseous species i adsorbing into solid/liquid phase j, $Pa \cdot cm^3/mol$

i Current density per unit volume, A/cm^3

i_{ideal} Ideal current density, A/cm^3

i_{tot} Total current density, combination of poly disperse micro structures, A/cm^3

j Current density per unit of active catalyst surface area, A/cm^2

j_{0H} Reference Heyrovsky-Volmer current density, A/cm^2

j_{0T} Reference Tafel-Volmer current density, A/cm^2

k_c Molar reaction rate

k_t Adsorption/desorption time constant

k_{O_2} Dissolution reaction rate constant of oxygen, m/s

n_d Electro-osmotic drag coefficient

N_i Species flux, $mol/(s \cdot cm^2)$

n_w Number of weights

P Pressure, Pa

R Universal gas constant, 8.3144 $J/(mol \cdot K)$

R_i Source term of species i, $mol/(s \cdot cm^3)$

r_{agg} Agglomerate core radius, nm

R_{O_2} Reactant consumption per unit area of surface, $mol/s \cdot cm^2$

T Temperature, K

V_{Pt} Platinum mass loading per unit volume in the catalyst layer, $g \cdot cm^{-3}$

W Cumulative weight

x_i Molar fraction of species i

z_i Charge of species i

Abbreviations

2D Two Dimensional

3D Three Dimensional

ACL Anode Catalyst Layer

AGDL Anode Gas Diffusion Layer

AMPL Anode Microporous Layer

BC Boundary Conditions

BPP Bi-polar Plates

BVP Boundary value problem

CCL Cathode Catalyst Layer

CGDL Cathode Gas Diffusion Layer

CL Catalyst Layer

CMPL Cathode Microporous Layer

DA Dissociative Adsorption

DOF Degrees of Freedom

FC Fuel Cell

FCS Fuel Cell Vehicles

FEM Finite Element Method

FIB Focused Ion Beam

GDL Gas Diffusion Layer

HCD High current density

HOR Hydrogen Oxidation Reaction

ICCP Ionomer Covered Catalyst Particle

LCD Low current density

LHS Left hand side

MEA Membrane Electrode Assembly

ML Membrane Layer

MPL Microporous Layer

nanoCT nano-focus Computed Tomography

OCV Open Cell Voltage

ORR Oxygen Reduction Reaction

PEFC Polymer Electrolyte Fuel Cell

PEM Polymer Electrolyte Membrane

PTFE Polytetrafluoroethylene

RA Reductive Adsorption

RD Reductive Desorption

RH Relative humidity

RHS Right hand side

RT Reductive Transition

SEM Scanning Electron Microscopy

TEM Transmission Electron Microscopy

Greek Letters

β Reaction symmetry factor

δ_{agg} Agglomerate film radius, nm

ϵ_{agg} Agglomerate porosity

η Overpotential, V

γ Reaction order

λ Sorbed water factor

μ	Network constant
ϕ_L	Thiele's modulus
ρ	Density, g/cm^3
σ	Conductivity, S/cm
Θ	Heavy side step function
θ_i	Coverage fraction of species i
ε	Porosity
ε_N	Electrolyte phase volume fraction
ε_S	Solid phase volume fraction
ε_V	Void phase volume fraction

Subscripts and Superscripts

0	Reference state
a	Anode
ads	Adsorbed species
agg	Agglomerate
e^-	Electron
eff	Effective value
eq	Equilibrium
g	Gas
H^+	Proton
I	Ionic species
i	Species index
N	Nafion
N	Nafion

SO_3^-	Sulphonic acid
th	Threshold

Chapter 1

Introduction

1.1 Motivation

A fuel cell (FC) is an electrochemical energy conversion device, which can be used to produce electrical energy. From a purpose and utilization stand point, a FC can be thought of much the same as a typical internal combustion engine: when supplied appropriate reactants a FC produces energy, which can in turn be used to power numerous different applications. However, compared to conventional combustion engines, fuel cells have many advantages: greater efficiencies, as high as 80% in combined heat and power applications, and no local emissions of greenhouse gases and other pollutants when powered by hydrogen. Like conventional engines, fuel cells can be used to power many applications such as automobiles, personal electronics, and back up power systems just to name a few! Therefore fuel cells are a key area of interest for industry and consumers alike.

There are many different types of fuel cells, depending on the fuels they consume, and the materials they are composed of. Polymer electrolyte fuel cells (PEFC) are one of the most attractive options for the purpose of powered transportation. PEFCs are a suitable power source for automobiles since they offer high power densities at relatively low operating conditions ($\approx 80^{\circ}C$) with minimal local environmental impact. Hydrogen FC powered cars will soon be a commercially available commodity, as major car manufacturers, such as BMW, Daimler, Ford, Honda, Hyundai, Nissan, and Toyota have pledged to release consumer hydrogen FC vehicles by 2017 [8].

PEFCs have been steadily developing since the early 1960s. Initially, due to their high costs, PEFCs were only used in highly specialized applications such as powering aircraft axillary, and the Gemini series space crafts. Throughout the late 80's and

early 90's several breakthroughs such as low platinum loadings and thin electrodes enabled more widespread use of PEFCs due to reduced costs. Testing and development of fuel cells today is still a crucial topic, as of 2009 the cost of PEFCs was $61 per kW [9], this value needs to be reduced to enable fuel cells to economically compete with other energy conversion devices. To this effect, great experimental efforts are being made by industry and academia alike.

Many aspects of experimental FC research are costly and time consuming. Several phenomena of interest take place at locations and scales which are difficult or currently impossible to experimentally observe. To this effect numerical modelling of PEFC can be performed in order to gain a better understanding of key phenomena, complimenting experimental efforts. PEFC models can be used to study the effects of key phenomena, and as a design and optimization tool in PEFC development.

In order to describe PEFC operational behaviour, mathematical models are required to describe inter-dependent mass transport and electrochemical physics within the PEFC domain. Individual models may be developed to explore different aspects of PEFC physics, however by this method key inter-dependencies may be omitted. The FC simulation tool set, OpenFCST [10], developed initially by Secanell [11], with many contributing developers [3, 5, 7, 12], and further improved in this work, aims to describe the most significant PEFC phenomena in a consistent manner. Specifically, this work aims to improve scientific understanding of micro structural phenomena, and their significance in PEFC design.

This thesis describes work towards the development of a multi-scale PEFC catalyst layer (CL) model, and its integration in a membrane electrode assembly (MEA) model. In the proceeding sections of this chapter the structure and operation of a PEFC is explained, a literature review on CL and CL micro structure models is performed, and key contributions of this work are outlined. In Chapter 2, numerical models which describe the electrochemical reactions and mass transport phenomena occurring within an operational FC are developed. In Chapter 3 the developed models are utilized to explore the effects of micro-scale mass transfer and electrochemical processes on the operating behaviours and efficiencies of PEFCs. Finally, in Chapter 4, conclusions are drawn based on the work carried out in Chapters 2 and 3.

1.2 PEFC Background

In a hydrogen fuel cell, gaseous hydrogen H_2 and oxygen O_2 react to form water H_2O. During this reaction electrical energy can be harnessed and used to perform work. Unlike in a combustion engine, the gaseous reactants do not react directly in combustion. Instead the reaction is divided into two sub electrochemical reactions. The electrochemical reaction consists of an individual reduction reaction and individual oxidation reaction.

$$\begin{aligned} H_2 &\rightleftharpoons 2H^+ + 2e^- \\ \frac{1}{2}O_2 + 2H^+ + 2e^- &\rightleftharpoons H_2O \\ H_2 + \frac{1}{2}O_2 &\rightleftharpoons H_2O \end{aligned} \tag{1.1}$$

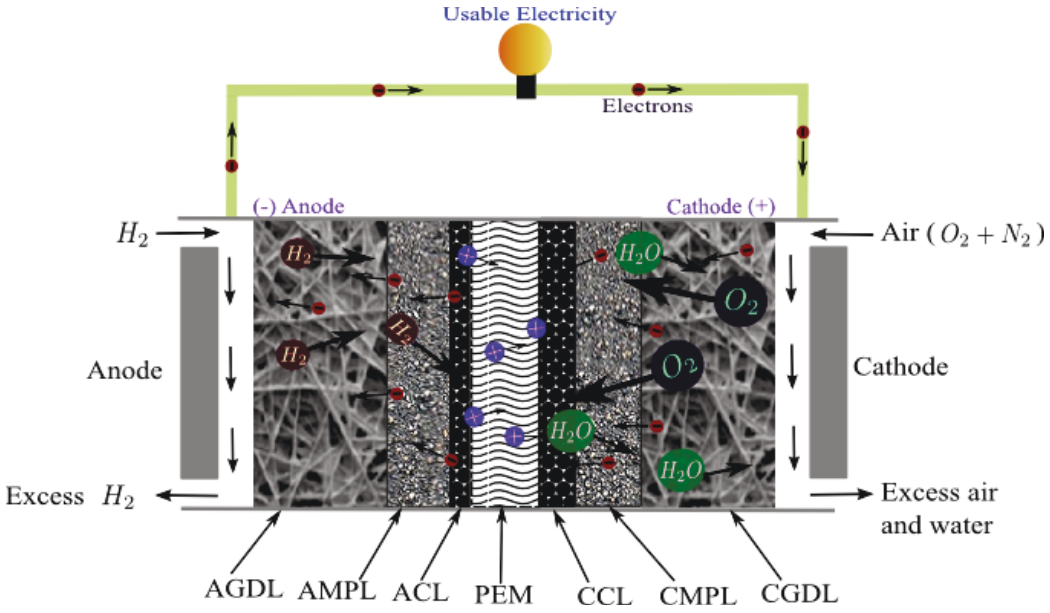

Figure 1.1 – The structure of a membrane electrode assembly (MEA), and the transport of reactants and products within. 'A' denotes the anode layers and 'C' denotes the cathode layers. Image reproduced from reference [3].

During fuel cell operation, hydrogen is oxidized at the anode, where it produces protons and electrons, corresponding the first stoichiometric relationship (1.1). This is know as the Hydrogen Oxidation Reaction (HOR). The produced protons travel from the left to the right hand side through the membrane layer. The produced

electrons travel from the anode to the cathode through an external circuit driven by a potential difference between the electrodes. At the cathode electrode oxygen is reduced with electrons and protons to produce water, corresponding to the second stoichiometric relationship (1.1). This is known as the Oxygen Reduction Reaction (ORR). The combination of the two half reactions; the oxidation of hydrogen at the anode, and reduction of oxygen at the cathode results in the final stoichiometric relationship (1.1). See visualization of reaction process in Figure 1.1.

As shown in Figure 1.1, the PEFC membrane electrode assembly (MEA) consists of several layers, each layer having a specific function. The gas diffusion layer (GDL) is a porous structure, consisting of interlinked carbon fibres. This layer facilitates the transport of gaseous reactants, and provides electrical conduction so that electrons can flow from the anode to the cathode via an external circuit. The micro porous layer (MPL), consisting of a porous carbon network, has similar functionality to the GDL, and facilitates transport of reactants and products from the GDL to the catalyst layer(CL). The cathode and anode catalyst layers, where the reduction and oxidation reactions take place respectively, are an isotropic mixture of electron conducting carbon, proton conducting Nafion® ionomer, pore space facilitating gaseous transport, and catalyst on which reactions take place, typically platinum. The platinum catalyst is used to catalyse the HOR and ORR, increasing the rate of reaction, allowing more power to be harnessed. Finally the polymer electrolyte membrane, located between the anode and cathode, facilitates proton transport from the anode to the cathode, whilst preventing transport of hydrogen, oxygen, and electrons.

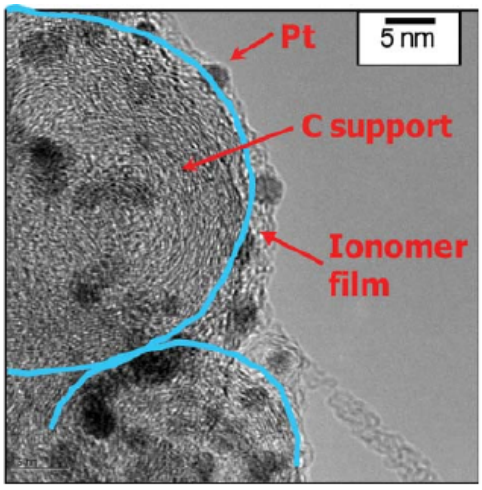

Figure 1.2 – High resolution TEM image of PEFC CL micro-structure showing catalyst support agglomerations [4]. Image reproduced from reference [5].

The micro structure of the CL consists of a mixture of Nafion® ionomer and platinum loaded carbon. Figure 1.2 shows aggregation of carbon particles surrounded by ionomer. The HOR anodic and cathodic reactions occur within these micro structures, therefore it is important to understand the mass transport and electrochemical processes occurring within this structure in order to accurately simulate PEFC operation. The focus of this project is on developing a modelling framework to facilitate the study of proposed micro structure models, and understanding the significance of the mass transport and electrochemical reaction phenomena occurring within.

Experimentally, FC operation is characterized using polarization curves, which describes the current:voltage operating characteristics of a MEA. An example of a polarization curves is given in Figure 1.3. The phenomena which dominate FC performance varies depending on reaction rate and operating potential: at low reaction rates, kinetic phenomena dominate. At moderate reaction rates the effect of ionic transport within the Nafion®ionomer phase is dominant. At high reaction rates, mass transport processes such as the dissolution of gaseous oxygen in Nafion, or pore blockage due to the presence of liquid water, dominate FC performance leading to a sharp decline in FC efficiency. The focus of this work, on PEFC CL micro structure, will improve characterization of the mass transport limited operating region.

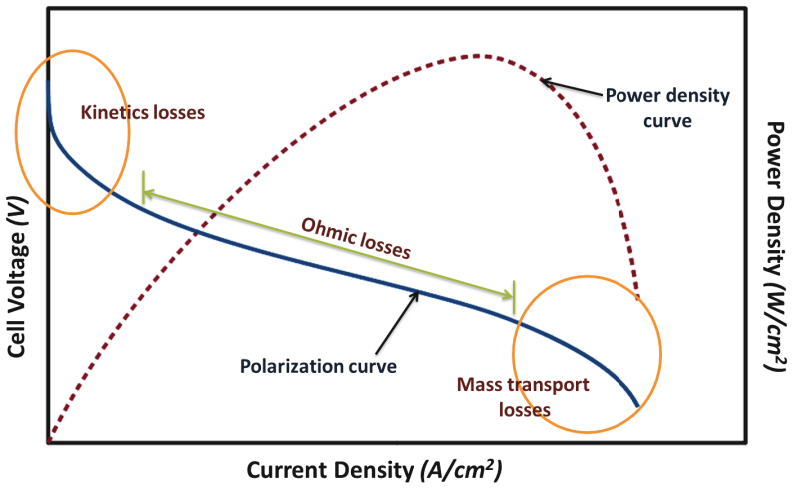

Figure 1.3 – A polarization curves describing the current:voltage relationship of a PEFC. Typical FC operation can be categorized into 3 regions: the kinetic, ohmic and mass transport regions, named after the phenomena which dominate FC performance at respective operating conditions. Image used with permission from Bhaiya [3].

1.3 Literature Review

As mentioned in Section 1.1, modelling of PEFC CLs is a beneficial area of research because it enables understanding of electrochemical and mass transport phenomena occurring at locations and scales difficult or impossible to experimentally observer. To date CL modelling approaches can be categorized into the following major groups:

- interface models, where the layers are modelled as infinitely thin interfaces, represented mathematically via boundary conditions [13–17]
- macrohomogeneous models, where reactant transport and electrochemical reactions occur across continuous domains with averaged effective properties [3, 18–20]
- agglomerate models, where reactant transport and electrochemical reactions are simulated throughout conceptual CL micro structure representations [1, 5, 11, 12, 21–29]. These models are often coupled with homogeneous model in a multi-scale approach
- reconstructed domains - micro-scale CL morphology reconstructed, typically three dimensional, based on CL descriptions obtained by FIB-SEM or nanoCT techniques [30–33]. Simulations on reconstructed micro-scale domains have been performed to determine effective electrochemical and mass transport properties [31–33]

The latter approaches provide greater detail and accuracy, as they include more geometric information, but consequently are also more computationally demanding.

The aim of this work is to improve understanding of fuel cell mass limited behaviour due to transport phenomena occurring within CL micro structure. To this effect a multi-scale simulation approach, which simultaneously considers inter-dependent macro and micro-scale mass transport processes, is the most appropriate modelling technique. In multi-scale CL models macro scale transport phenomena are typically described using a macrohomogenous model, whilst micro-scale mass transport and electrochemical phenomena are described using an agglomerate model. Agglomerate models are appropriate for use within multi-scale CL models, as they provide a description of CL micro structure whilst being computationally feasible.

Agglomerate models are a typical description of PEFC CL micro structure, commonly used to describe the mass transport limiting effects occurring during FC operation. Iczkowski and Cutlip [28] were the first to account for micro-scale oxygen limiting transport losses with an agglomerate model. Many studies have been carried out since based on the agglomerate concept. Agglomerates are assumed to be small, with radii less than $1\mu m$, formed during the catalyst ink fabrication process due inter particle attraction, and consist of groups of platinum loaded carbon particles surrounded by a ionomer thin film. At present agglomerate-based models are seen by some as the state of the art model for describing CL micro structure [22, 27].

Multi-scale models have been used to improve understanding, and also perform CL design and optimization. Secanell et al. [11, 24] developed a 2D CL + GDL model, with embedded 1D analytical agglomerate based on work by Sun et al. [29]. Secanell developed a framework which related micro structural properties with macro scale structural properties, adding consistency in mass conservation not widely used before [11]. Jain et al. [21] performed PEFC CL optimization using a 1D agglomerate model embedded in a 2D CL + GDL model, similar to work done by Secanell et al. [24]. Using the 2D(1D) model Jain investigated the effects of platinum loading and through plane platinum grading of the CL.

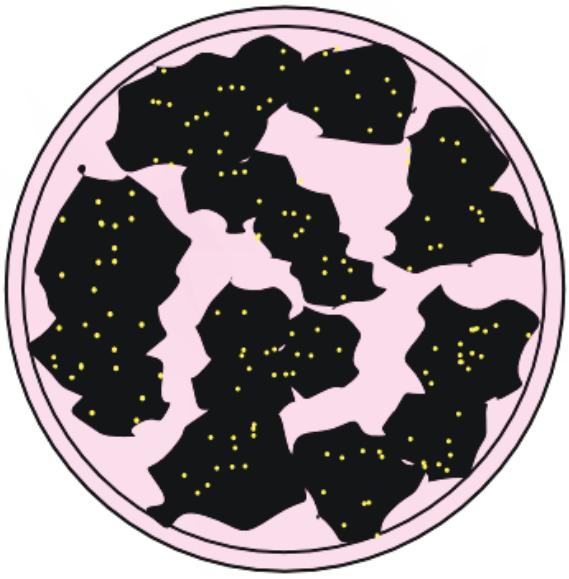

Figure 1.4 – Ionomer filled agglomerate consisting of platinum loaded carbon core, surrounded by thin ionomer film.

Agglomerate are typically depicted as in Figure 1.4; a collection of platinum loaded carbon particles bound by a thin ionomer film, with the primary pores of the agglomerate core filled either by ionomer [1, 5, 11, 12, 21–24, 34] or water [5, 12, 25, 26]. Experimentally it is difficult to determine whether the primary pore space within the porous agglomerates is water filled or ionomer filled. Recent studies suggest that the primary pores are void filled [35, 36], which become water filled during fuel cell operation due to the production of water [5, 25]. Both micro structure morphologies are considered in this work.

As mentioned previously many examples of the ionomer filled agglomerate model exist in literature. A review on previous agglomerate models can be found in references [5, 27, 37, 38]. More recently Sun et al. [29] developed a one dimensional analytical expression for current density produced by an ionomer filled agglomerate, base on the assumptions that the reaction is oxygen transport limited and that the oxygen reaction order is equal to one. Sun et al. [29] used the developed agglomerate model in a two-dimensional cathode model which was used to study the influence of catalyst layer structural parameters. Sun et al. [29] note that at high current density platinum utilization within ionomer filled agglomerate is extremely poor.

Dobson [5] modified the analytical expression presented by Sun et al. [29], correcting for active area scaling factors. Dobson highlighted limitations of the traditional analytical solution for the ionomer filled agglomerate problem, such as limiting assumption of oxygen reaction order, and ignoring of proton charge transport mechanisms. To improve upon these limitations Dobson developed numerical agglomerate models, solving using BVP solver COLDAE [39]. Within Nafion® ionomer it is assumed that proton concentration is constant and equal to the concentration of sulphonic acid groups. This is a key difference between the ionomer and water filled assumptions, which leads to radically different proton concentration and electrolyte potentials within respective agglomerate cores, as will be discussed later.

Moore et al. [40] utilized the model developed by Dobson [5] to investigate the effects of micro-scale proton conductivity, non-equilibrium boundary conditions, and different kinetic models on PEFC performance. Moore et al. [40] reports that for the ionomer filled agglomerate proton transport mechanisms are insignificant, and kinetic parameters proposed by Neyerlin et al. [41, 42] cause over prediction of current. Analysis carried out in reference [40] was performed by the author of this work, and is also present in this work.

Song et al. [43] developed an analytical ionomer filled agglomerate agglomerate. Song et al. [43] used said model to optimize and analyze the impact of material property combinations on cathode catalyst which was subdivided into several sub layers. Song et al. [43] notes that the most crucial sub layer of the CL for optimization was the layer adjacent to the membrane.

Recently, some variants of the spherical agglomerate model have been introduced. Kamarajugadda and Mazumder [37] modelled the PEFC CL micro structures using overlapping ionomer filled agglomerate of unequal radii. Agglomerate geometry (core and ionomer thin film dimensions) was found to be significant when the equivalent spherical radius of the agglomerate were larger than 600 nm, but these effects became insignificant for agglomerates smaller than 200 nm. The authors notes that per volume current density is improved by the higher surface to volume ratios of the irregular overlapping agglomerates.

Agglomerate dimensions are commonly used as a model input parameter in order to fit simulation results to experimental data. Dobson [5] performed a literature review of agglomerate dimensions used in theoretical models, reporting radii varying from 50 nm to 1μm. These dimensional parameters are inconsistent with experimental literature, which suggests agglomerate radii ranging from 25-200 nm [1, 44–46]. Fitting of agglomerate dimensional parameters should be avoided as it provides a false explanation for mass transport limited behaviour.

Cetinbas et al. [27] states that conventional agglomerate models which represent the agglomerate core as a homogeneous mixture of catalyst, catalyst support, and electrolyte, are incapable of accurately describing oxygen diffusion losses that arise from a reduction in catalyst loading. The author states that limiting current of current agglomerate models is due to thin film reactant transport limitations. The author presents a cylindrical agglomerate model with discrete platinum particles embedded in an ionomer core. Cetinbas et al. [27] reports that the inclusion of individual discrete catalyst particles induces significant mass transport, especially in the mass transport limited operating region. Cetinbas et al. [27] agglomerate analysis was not integrated within a multi-scale framework, therefore it does not consider numerous other significant mass transport and electrochemical phenomena occurring within a PEFC. Additionally agglomerate dimensional parameters used by Cetinbas et al. [27] are much larger than experimentally observed. Therefore the topic of micro-scale

catalyst distribution warrants further research efforts.

Typically the dissolution of gaseous oxygen into Nafion® films is assumed to be an equilibrium process and therefore described using Henry's law [5, 11, 12, 21, 22, 24, 29]. Islam et al. [47] states that under steady state diffusion flux, surface dissolution is a non-equilibrium process. Suzuki et al. [48] developed an agglomerate model which incorporates a non-equilibrium dissolution mechanism from the gaseous to the ionomer phase. Suzuki et al. [48] report that the inclusion of non equilibrium interface model is significant when the ionomer thin film thickness is less than 100 nm, and the inclusion of the non-equilibrium model improves the ability of the agglomerate model to correctly represent CL performance.

Due to its simplicity and significant assumptions, the validity of agglomerate models are commonly disputed in literature. Kulikovsky [49] questions whether agglomerate models are still necessary for modelling of modern catalyst layers, citing the improvements in catalyst ink fabrication which has reduced the size of observed agglomerations in CLs from the order of ~ 1 μm to ~ 100 nm. Kulikovsky reports that when agglomerate radii $\leq$100 nm, significant disagreement with the macro homogenous CL model only occurs at cell potentials ≤ 0.1 V. This is contrary to findings of many previous works [5, 40], therefore the significance of the existing micro-scale models against the macrohomogeneous model should be thoroughly evaluated.

Yoon and Weber [23] using the ionomer filled assumption comprehensively investigated the impact of typical modeling assumptions of the ionomer filled spherical agglomerate model including constant electrolyte potential, and uniform oxygen transport pathways. Yoon and Weber [23] reports that the assumption of constant electrolyte potential is acceptable, and that non uniform distribution of reaction sites within the agglomerate core leads to reduced reaction rates due to increased reactant pathways.

Many PEFC numerical studies address issues of cell degradation due to the production of free radicals and presence of impurities. Free radical H_2O_2, which can form at the anode and cathode, attack the polymer causing membrane thinning and pinhole formation [50]. Ziegler et al. [50] simulated H_2O_2 concentrations inside PEFC using an agglomerate model for the electrode. They note that reducing oxygen permeability in the ionomer is the most important and effective method to reduce the formation of H_2O_2.

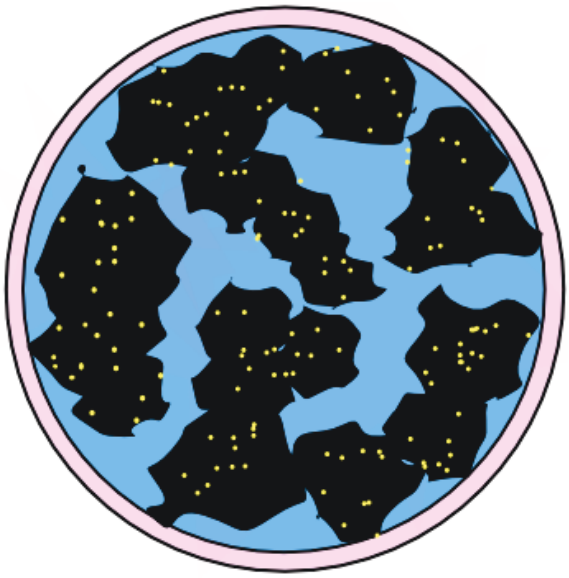

Figure 1.5 – Water filled agglomerate consisting of platinum loaded carbon core, surrounded by thin ionomer film.

Figure 1.5 shows the water filled agglomerate model, which is similar in description to the ionomer filled model. Assumptions of agglomerate composition determine the effective transport mechanisms occurring within, resulting in significantly different transport behaviours. As mentioned, for the ionomer filled case it is assumed that protons are evenly distributed throughout the ionomer phase. However proton transport mechanisms differ between the ionomer filled and water filled agglomerate assumptions. Within the water filled domain protons are transported depending on difference in chemical potentials, and Coulombic interactions with electrolyte and charge surfaces.

Wang et al. [25] developed a water filled agglomerate model describing proton transport using the Nernst-Plank equation coupled with Poisson's equation of electrostatic potential. Wang et al. [25] reports drastically different proton concentration and over potential profiles within the agglomerate core, as compared to the ionomer filled model. Using this model Dobson [5] studied the difference between the water filled and ionomer filled assumption using a multi-scale approach. Dobson reports that there is little difference in PEFC performance for either assumption, but numerical challenges prevented Dobson from performing a full investigation of the water filled versus ionomer filled assumption. Comparison results are unclear, therefore further

comparison of the water filled and ionomer filled agglomerate models is warranted.

Additionally the formation of ionic double layers on charge carbon surfaces in water filled pores has been studied. Chan and Eikerling [51] developed a pore scale model, employing the Stern model to relate the surface charge density at the pore walls to the electrode potential.

Sadeghi et al. [26] proposed a water filled agglomerate model, consisting of conical water filled pores, which describes double layer boundary formation using Nernst-Plank-Poisson theory, in order to describe a more accurate representation of proton transport mechanisms within the CL micro structure. Sadeghi et al. [26] reports that the proposed water filled agglomerate model predicts agglomerate effectiveness similar to experimental observations.

Primarily agglomerate and homogeneous catalyst layer models are used to study the cathode catalyst layer, but several works have also used these models to study the anode. Karan [52] studied transport limited catalyst utilization of the anode using an agglomerate model. Karan found that hydrogen oxidation reaction is limited at two scales: at the agglomerate scale the reaction is restricted to the outer 20 % of the agglomerate core (corresponding to a 50% core volume fraction) due to limited hydrogen diffusivity in Nafion, and at the catalyst layer scale reaction was restricted due to poor proton conductivity and electronic potential gradients. Secanell et al. [2] carried out similar analysis using an anode multi-scale CL + GDL model, also citing anode catalyst layer conductivity as a main cause for poor platinum utilization.

Epting and Litster [1] states that typically a single representative size of agglomerate radius is assumed for catalyst layer models. Epting et al. [46] analyzed nanoCT data to obtain size distribution information for agglomerates within PEFC CLs. Based on this work Epting developed a model describing a catalyst layer slice (with constant oxygen pressure and overpotential) considering a poly disperse agglomerate diameter distribution. Epting reports that the poly disperse structure had significant effect on simulated CL performance as compared to the traditional modelling assumption of agglomerate size mono dispersion. Epting and Litster [1] however did not consider poly dispersion within a multi-scale framework, therefore the effects of poly dispersion on predicted MEA are still unknown.

Additionally many experimental characterizations of PEFC CLs [46, 53] report the presence of structures approaching the dimension of primary platinum loaded carbon particles, therefore the use of agglomerates to describe all catalyst layer micro structure morphology may be a invalid.

Typically agglomerate models proposed in literature use the Tafel kinetics model to predict ORR rates [5, 11, 21, 22, 25, 26, 29], however it has been shown that the double trap kinetics is a more accurate description of the ORR [7, 54].

Based on this discussion, it can be seen that certain aspects of PEFC CL literature can be improved, such as the description of catalyst distribution throughout the micro structure, description of oxygen dissolution mechanism in thin ionomer films, the use of the improved kinetics models, and the consideration of poly disperse micro structural formations. Whilst many of these aspects of CL micro-structure, mass transport, and electrochemical reactions, have been studied individually at the agglomerate scale, in order to assess their true impact on PEFC performance, they must be considered within a multi-scale CL model, and compared in a consistent manner. Utilizing OpenFCST's framework this is possible. In the following section, the contributions of this work towards these discussed topics are described.

1.4 Thesis Contributions

The contributions made in this work to PEFC modelling literature are:

1. Improvement of existing CL micro-scale models by developing the following:
    (a) modification of proton conductivity within Nafion® ionomer, in order to gain appreciation for the mechanism of micro-scale proton charge transport on PEFC performance
    (b) dissolution mechanisms of oxygen in Nafion® thin films as described in reference[48], to investigate the capability of this phenomena in better describing mass transport limited PEFC behaviour
    (c) improved description of platinum distributions within micro structure, to assess the effects of catalyst accessibility within CL micro structures
    (d) improved numerical stability of models, allowing the analysis of PEFC over a wider range of operating conditions than possible before

(e) description of micro-scale geometric poly dispersion within a multi-scale MEA framework, in order to assess the validity of the traditional modelling assumption of a mono disperse micro-scale geometry.

2. Comprehensive comparison of water and ionomer filled model, which could not previously be achieved [5]

3. Modification of double trap Kinetics Model [7, 54] to include sensitivity to proton concentrations, in order to study micro structure models with varying proton concentrations

4. Creation of new micro structural model to describe PEFC CL formations similar in dimension to primary platinum loaded carbon particles

Chapter 2

Numerical Modelling

2.1 Introduction

In this section the mathematical models used in this work are explained. First the fundamental governing equations used to describe electrochemical phenomena occurring within fuel cells layers are described. Kinetic models are reviewed, and the double trap kinetic model [7] is reformulated to include sensitivity to proton concentration. Finally CL micro-scale models are developed, and improvements implemented as part of this work are explained.

2.2 Membrane Electrode Assembly Model

2.2.1 Introduction

An outline of the electrochemical reaction a mass transport processes occuring within a PEFC are described in Section 1.2. In this section a multi-scale FEM mathematical model which is used to simulated said electrochemical and transport phenomena occurring within PEFCs is developed.

In literature there are several commonly used approaches to modelling PEM fuel cells. Reduced dimension models employ empirically derived relationships describing fuel cell performance. These reduced dimension models are relatively computationally inexpensive and are typically used for modelling full stack scale behaviour. Another category of FC models are MEA models which consider the transport and consumption of reactants in a 2D or 3D domain allowing researchers to assess the impact of materials and porous layer structures in greater detail.

In this work the latter type of model is used. The across the channel MEA model presented in this work, developed by Secanell [11], has been extensively used and expanded by several studies [3, 5, 7, 12, 55]. The model describes steady state

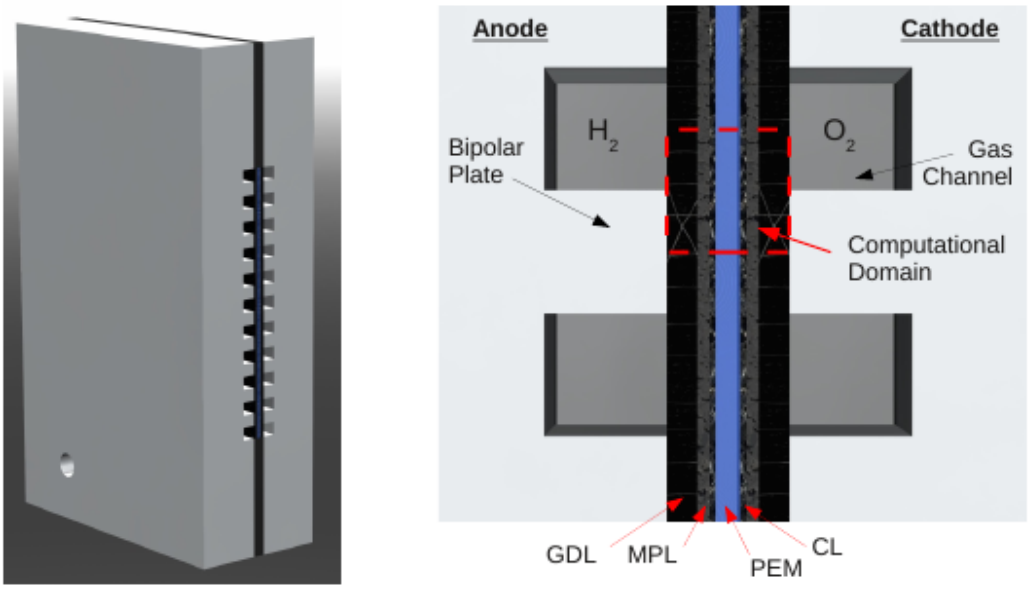

(a) CAD Drawing showing bipolar plate assembly encasing MEA

(b) 2D closeup of MEA cross section

Figure 2.1 – MEA diagrams showing bipolar plates and MEA, from reference [5]

transport and consumption of various species throughout the GDL, MPL, CL, and ML layers of the MEA. Due to domain symmetry simulations are performed on a reduced domain as seen in Figure 2.1(b) for computational efficiency.

In this work a multi-scale catalyst layer model developed by Dobson [5] is used, in which macro scale mass and charge transport are resolved using a macro-homogeneous catalyst layer model described in Section 2.2.4, and reaction source terms are resolved using micro-scale models described in Section 2.4. This multi-scale relationship can be seen in Figure 2.2. In this work the multi-scale catalyst layer model is further developed, allowing investigation of additional electrochemical and transport phenomena. The numerical stability of the multi-scale catalyst model is improved, allowing investigation of PEFC performance operating at conditions which previously could not be simulated.

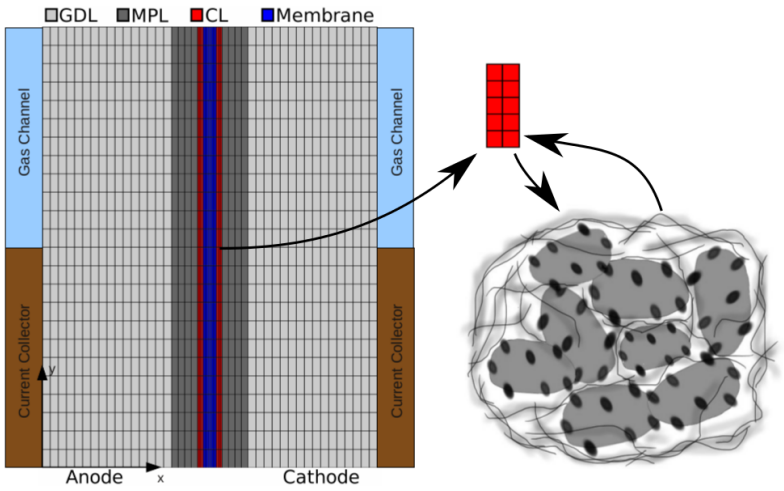

Figure 2.2 – The MEA computational domain. The macro:micro-scale coupling is as follows: species transport in the multi-scale catalyst layer is resolved using a macro-homogeneous model (left) whilst reaction rates are resolved using micro-scale models.

2.2.2 Assumptions

The following assumptions are inherent in the formulation of the MEA model presented in this work.

1. The fuel cell operates at steady state
2. The fuel cell operates at constant temperature and pressure
3. The cathode is fed with a mixture of water vapour, nitrogen, and oxygen. Oxygen and water vapour in the cathode are considered as infinitely dilute species in nitrogen
4. The anode is fed with a mixture of water vapour and hydrogen. Water vapour in the anode is considered as an infinitely dilute species in hydrogen
5. Gaseous species behave as ideal gasses
6. Convection is not considered: due to the domain size diffusive fluxes are dominant, and throughout the porous media there exist only small pressure gradients, resulting in low fluid velocities
7. The membrane layer blocks the transport of gaseous species and electrons

8. Transport of sorbed water and protons occurs within ionomer phase of the membrane and catalyst layers

9. Proton concentrations in ionomer are assumed to be constant and equal to the concentration of sulphonic groups

10. Electron transport only occurs in the solid phase of the catalyst, micro porous, and gas diffusion layers

11. Proton and electron charge transport are described using Ohms law

12. Transport of gaseous species is described using Fick's law

13. The GDL is a random anisotropic mixture of carbon fibre and pore space

14. The CL is a random isotropic mixture of ionomer, platinum loaded carbon, and pore space

15. The MPL is a random isotropic mixture of solid carbon and pore space

16. The ML is an isotropic solid layer composed of ionomer electrolyte material

17. The presence of liquid water is not considered, therefore humidity results may exceed 100 % RH, these results are not physical [1]

2.2.3 Membrane Layer

The membrane layer facilitates the transport of protons and sorbed water. Transport of ionoic species in electrolye media can be described using the Nernst-Plank equation. The Nernst-Plank equation describes the transport of a charged species in an dilute electrolyte due to differences in concentraion, electrostatic interactions, and convective flow, and is as follows:

$$\vec{N_i} = -D_{ij}\vec{\nabla}c_i - \frac{z_i D_{ij} F}{RT} c_i \vec{\nabla}\phi + c_i \vec{v} \tag{2.1}$$

where diffusive, electrostatic, and convective mechanism are described by their relative terms on the right hand side of equation (2.1) respectively, D_{ij} is the binary

[1] Simulation results reporting humidity values greater than 100% will be represented in polarization curve figures as a dashed line.

diffusion coefficient for species i in species j, c_i is the concentration of specie i, z_i is the charge of species i, F is Faraday's constant, R is the universal gas constant, T is temperature, ϕ is the potential of the medium, and $\vec{v}$ the velocity of the fluid.

Typically when applying equation (2.1) to describe the transport of charged species in a system of interest, certain mechanisms may be neglected, depending on their relevance. For the membrane layer convective fluxes may be neglected, since $\vec{v} \approx 0$. Additionally due to the homogeneous presence of sulphonic acid groups SO_3^- troughout Nafion® ionomer, a constant proton concentration throughout the membrane layer is assumed. Constant proton concentration implies that $\vec{\nabla} c_{H^+} = 0$, therefore diffusive fluxes may be neglected. By making these simplifications, the Nernst-Plank equation is reduced to Ohm's law. Therefore proton charge transport is described as follows:

$$\vec{N}_{H^+} = -\frac{\sigma_m^{eff}}{z_{H^+} F} \vec{\nabla} \phi_m = -\frac{\sigma_m^{eff}}{F} \vec{\nabla} \phi_m \tag{2.2}$$

where σ_m^{eff} is the effective proton conductivity of the layer, and z_{H^+} is the associated charge of individual protons, equal to +1. Since the membrane layer is composed of bulk Nafion, bulk conductivity values may be used, i.e. $\sigma_m^{eff} = \sigma_m$. Proton conductivity σ_m is calculated as follows:

$$\sigma_m = \frac{z_{H^+}^2 F^2 D_{H^+} c_{H^+}}{RT} \tag{2.3}$$

Proton conductivity values for bulk Nafion® NRE-211 were reported by BekkTech [56], and fitted with a polynomial expression by Dobson [5]. This expression is used to describe proton conductivity within the ML, and is as follows:

$$\sigma_m = \left(-1.0125 \times 10^{-4} \lambda^2 + 0.01052\lambda - 0.020634\right) e^{751.5412\left(\frac{1}{303} - \frac{1}{T}\right)} \tag{2.4}$$

Sorbed water transported throughout the membrane layer due to electro-osmotic drag and back diffusion is described using the mathematical model outline by Springer et al. [18]. Electro-osmotic drag occurs when water molecules are attracted to protons, which move through the membrane due to Coulombic interactions. Similar to Ohm's law, electro-osmotic is described as follows:

$$\vec{N}_{\lambda,\text{drag}} = -n_d \frac{\sigma_m^{eff}}{F} \vec{\nabla} \phi_m \tag{2.5}$$

where n_d is the electro-osmotic drag coefficient, experimentally observed to be 1 [57, 58], and λ is the amount of sorbed water in ionomer relative to the sulphonic concentration.
λ is described as follows:

$$\lambda = \frac{c_{H_2O}}{c_{SO_3^-}} \tag{2.6}$$

where $c_{SO_3^-}$ is the concentration of sulphonic groups in ionomer, calculate as follows:

$$c_{SO_3^-} = \frac{\rho_{m,dry}}{EW} \tag{2.7}$$

where $\rho_{m,dry}$ is the density of ionomer, and EW is its effective weight (unit mass per mol of $c_{SO_3^-}$).

Water is also transported within the electrolyte media due to chemical potentials. Species flux due to differences in chemical potentials is commonly described using Fick's law. Fick's law may be exclussively used to describe reactant flux if it is the sole dominant transport mechanism, and other mechanisms such as convective flow are negligible (i.e. in a fluid pressure is constant, velocities are zero). Fick's law is as follows:

$$\vec{N}_i = -D_{ij}\vec{\nabla}c_i \tag{2.8}$$

where D_{ij} is the binary diffusion coefficient for species i in species j.

Water flux due to differing concentration is therefore described using Fick's law (2.8), rearranged with using the expressions of λ (2.6) and $c_{SO_3^-}$ (2.7):

$$\vec{N}_{\lambda,\text{diffusion}} = -\frac{\rho_{dry}}{EW}D_\lambda^{eff}\vec{\nabla}\lambda \tag{2.9}$$

where D_λ^{eff} is the effective diffusion of sorbed water within the given media, for bulk Nafion® , $D_\lambda^{eff} = D_\lambda$. Combining equations (2.5) and (2.9) the following expression for sorbed water transport is obtained:

$$\vec{N}_\lambda = -n_d\frac{\sigma_m^{eff}}{F}\vec{\nabla}\phi_m - \frac{\rho_{m,dry}}{EW}D_\lambda\vec{\nabla}\lambda \tag{2.10}$$

Diffusion coefficients for sorbed water in ionomer D_{λ}^{eff} were experimentally determined by Motupally et al. [59] for Nafion® 115 membrane, and are given as:

$$D_{\lambda} = \begin{cases} 3.10 \times 10^{-3} \lambda(-1 + e^{0.28\lambda}) \exp\left(\dfrac{-2436.0}{T}\right) & \text{if} \quad 0 < \lambda \leq 3 \\ 4.17 \times 10^{-4} \lambda(1 + 161 e^{-\lambda}) \exp\left(\dfrac{-2436.0}{T}\right) & \text{if} \quad 3 < \lambda \leq 17 \end{cases} \tag{2.11}$$

According to assumption 7, the membrane layer blocks the transport of gaseous* water vapour, hydrogen, oxygen, nitrogen, and electrons. Therefore within the ML the following is true:

$$\vec{N}^{*}_{H_2O} = \vec{N}_{H_2} = \vec{N}_{N_2} = \vec{N}_{e^-} = 0 \tag{2.12}$$

2.2.4 Catalyst Layers

The catalyst layer is a porous media, throughout which electrochemical reactions and species transport takes place. For simplicity when describing gaseous species, concentrations of reactants and products are described using molar fractions:

$$c_i = c_T \, x_i = \frac{P_T}{RT} \, x_i \tag{2.13}$$

where x_i is the molar fraction of species i, c_T is the concentration of the total mixture, and P_T is the total gas pressure.

In the anode catalyst layer gaseous hydrogen and water vapour diffuse through the porous catalyst layer structure. Hydrogen is dissolved and transported within the catalyst layer micro structure where it is reacted at the electrochemically active platinum catalyst - this is described in greater detail in Section 2.4. Gaseous species transport in the anode CL is modelled using Fick's law (2.8). Since the mixture of hydrogen and water vapour is a binary mixture, it is only necessary to describe the transport of water vapour, as the molar fraction of hydrogen is simply the complement of water vapour, i.e. $x_{H_2} = 1 - x_{H_2O}$. Assuming isobaric and isothermal conditions, the flux of water vapour is therefore as follows:

$$\vec{N}_{H_2O} = -\frac{P_T}{RT} D^{eff}_{H_2O,H_2} \vec{\nabla} x_{H_2O} = -D^{eff}_{H_2O,H_2} \vec{\nabla} c_{H_2O} \tag{2.14}$$

Within the cathode catalyst layer, transport for gaseous species oxygen, nitrogen, and water vapour occurs. A multi-component gaseous mixture therefore exists within the cathode. Multi-component diffusive gaseous transport is typically described using the Maxwell-Stefan equation, however this equation introduces a great deal of non linearity into the system of equations. If the components of interest in a multi-component mixture are sufficiently dilute within another component then assumption 3 is valid, and Fick's law may be used to model gas transport in the cathode. The transport of only two species rather than 3 need be described Nitrogen molar fraction can be described as $x_{N_2} = 1 - x_{H_2O} - x_{O_2}$. Transport of gaseous oxygen is as follows:

$$\vec{N}_{O_2} = -\frac{P_T}{RT} D^{eff}_{O_2,N_2} \vec{\nabla} x_{O_2} \tag{2.15}$$

Similar to the anode, water vapour transport in the cathode is modelled using equation (2.14), however the diffusion coefficient $D^{eff}_{H_2O,H_2}$, is replaced with a value for water vapour in nitrogen $D^{eff}_{H_2O,N_2}$.

It is assumed that the catalyst layers are isotropic porous mixtures of ionomer and platinum loading carbon, therefore the effective diffusivities $D^{eff}_{H_2O,H_2}$, $D^{eff}_{H_2O,N_2}$, and $D^{eff}_{O_2}$ are calculated for both the anode and cathode using percolation theory (2.16). Percolation can be used to calculate effective transport properties of porous media, based on the porosity and orientation of the media. Additionally percolation theory predicts that reaction transport is impossible below a threshold porosity, due to the presence of a discontinuous pore network. Using percolation theory effective diffusion is described as follows:

$$D^{eff}_{i,j} = D_{i,j} \left(\frac{\varepsilon - \varepsilon^{th}}{1 - \varepsilon^{th}} \right)^{\mu} \Theta(\varepsilon - \varepsilon^{th}) \tag{2.16}$$

where ε^{th} is the experimentally determined threshold porosity, below which diffusion does not occur, μ is the network constant depending on the orientation of the porous media, and Θ is the heavy side step function, given as:

$$\Theta(\varepsilon - \varepsilon^{th}) = \begin{cases} 0 \text{ for } (\varepsilon - \varepsilon^{th}) < 0 \\ 1 \text{ for } (\varepsilon - \varepsilon^{th}) \geq 0 \end{cases} \tag{2.17}$$

Electrons and protons are produced in the anode catalyst layer, and consumed in the cathode catalyst layer. Electron transport is described using Ohm's law (2.2) as follows:

$$\vec{N}_{e^-} = -\frac{\sigma_s^{eff}}{z_{e^-}F}\vec{\nabla}\phi_s = \frac{\sigma_s^{eff}}{F}\vec{\nabla}\phi_s \tag{2.18}$$

where σ_s^{eff} is the electron conductivity of the layer,z_{e^-} is the associated charge of individual electrons , equal to -1 . Electrons are transported through the platinum loaded carbon porous network of the catalyst layers. Effective conductivity is described using percolation theory (2.16).

Similar to the ML, proton charge transport is described using Ohm's law (2.2). Effective proton conductivity values are calculated from experimental data reported by Iden et al. [60]. Effective proton conductivity values are reported for different RH values. Domican et al. [61] fitted data from Iden et al. [60], producing the following expression:

$$\sigma_m^{eff} = \varepsilon_N^{1.5}\left(1.931\times10^{-7}a_w^3 - 6.735\times10^{-6}a_w^2 + 0.00075a_w - 0.008\right)e^{751.5412\left(\frac{1}{353}-\frac{1}{T}\right)} \tag{2.19}$$

where ε_N is the electrolyte volume fraction, and a_w is the water activity given as follows:

$$a_w = \frac{p_T\ x_{H_2O}}{p_{sat}(T)} \tag{2.20}$$

Similar to the ML, water transport within the catalyst layers is described by the model proposed by Springer et al. [18]. Effective sorbed water diffusivity is again given by Motupally et al. [59], corrected for porous media using the Bruggeman correlation[62]:

$$D_{i,j}^{eff} = D_{i,j}\ \varepsilon^{1.5} \tag{2.21}$$

The Bruggemann correlation states that diffusion will always be possible provided $\varepsilon \neq 0$. Therefore for sorbed water transport through the CL, effective diffusivity is as follows:

$$D_\lambda^{eff} = D_\lambda\ \varepsilon_N^{1.5} \tag{2.22}$$

For the macro homogeneous CL model current density i, A/cm^3_{CL}, is calculated as follows:

$$i = jA_v \tag{2.23}$$

where j is the reaction rate predicted using with the Tafel kinetics model or double Trap kinetics model for the ORR, or the dual path Kinetics model for the HOR, in units of A/cm^2_{Pt}, and A_v is the active area factor, in units of cm^2_{Pt}/cm^3_{CL}, describing the experimentally measured electrochemically active platinum surface area per unit volume of the catalyst layer. An assumption of the macro homogeneous CL model is that gaseous reactants dissolve into the ionomer phase in order to be reacted on the platinum catalyst surface. The concentrations of reactants within the ionomer phase is described using Henry's law:

$$c_i = \frac{P_i}{H_{i,j}} \tag{2.24}$$

where P_i is pressure of gaseous species i, and $H_{i,j}$ is the Henry's coefficient of gaseous species i adsorbing into solid/liquid phase j.

For the multi-scale catalyst layer model, current density i are calculated using micro-scale models as described in Section 2.4. The micro-scale models resolve current density i for boundary conditions supplied by the multi-scale catalyst layer model, such as $\{P_{O_2}, P_{H_2}, \phi_s, \phi_m, \lambda\}$, as well as various material and kinetic properties.

Couplings between species flux (2.15) and (2.2), and sink terms (2.23) are described in Section 2.2.8.

2.2.5 Micro Porous Layer

Within the void phase of micro porous layers there exists transport of gaseous hydrogen and water vapour (anode MPL), and nitrogen, oxygen and water vapour (cathode MPL). Throughout the solid phase of the micro porous layer there exists electron transport through the solid carbon conducting phase.

Transport of gaseous species is described using Fick's law, similar to (2.14). Effective transport properties for gases travelling through the isotropic MPL are calculated using percolation theory (2.16).

Transport of electrons through the MPL is modelled as before, using Ohm's law (2.18). Effective electron conductivity of the MPL is calculated using percolation theory (2.16).

No ionomer phase exists in the MPL, therefore no mechanisms for proton and sorbed water transport exist, hence fluxes are are equal to zero:

$$\vec{N_{H^+}} = \vec{N_\lambda} = 0 \tag{2.25}$$

The implications of equation (2.25) are that protons and sorbed water are restricted to the CLs and ML.

2.2.6 Gas Diffusion Layer

Within the GDL there exists transport of charged and gaseous species identical to the MPL, with the same set of equations being used to describe transport of gaseous and charged species, i.e. equation (2.15) and (2.18).

The GDL is assumed to be an anisotropic mixture of carbon fibres, therefore the effective diffusivity and electrical conductivity of the GDL are calculated using Percolation theory (2.16). The GDL is an anisotropic material. For anisotropic materials, Tomadakis and Sotirchos [63, 64] modified equation (2.16) as follows:

$$D_{g,i}^{eff} = D_g \, \varepsilon \left(\frac{\varepsilon - \varepsilon^{th}}{1 - \varepsilon^{th}} \right)^{\mu^i} \Theta(\varepsilon - \varepsilon^{th}) \tag{2.26}$$

where i corresponds to the in-plane or through plane direction, $D_{g,i}^{eff}$ is the effective diffusivity of gas g through the porous media in direction i, and D_g is the bulk diffusion coefficient of gas g.

2.2.7 Boundary Conditions

The computational domain in which electrochemical reactants, and species transport are simulated for, is shown in Figure 2.2. The bipolar plate assembly is represented in this domain by the inclusion of several boundary conditions. For the cathode current

collector, zero normal flux of the following species relative the collector surface is imposed:

$$\vec{n} \cdot \vec{N}_{O_2} = \vec{n} \cdot \vec{N}_{H_20} = 0 \tag{2.27}$$

Additionally the electrical cell potential is applied to the cathode current collector:

$$\phi_s = V_{cell} \tag{2.28}$$

At the cathode gas channel, the net normal flux of electrons must be zero, therefore:

$$\vec{n} \cdot \vec{N}_{e^-} = 0 \tag{2.29}$$

Additionally input oxygen and water concentrations are imposed at the cathode channel interface:

$$x_{O_2} = x^0_{O_2} \tag{2.30}$$

$$x_{H_2O} = x^0_{H_2O,c} \tag{2.31}$$

At the anode current collector, zero normal flux of water vapour relative to the collector surface is imposed:

$$\vec{n} \cdot \vec{N}_{H_20} = 0 \tag{2.32}$$

Additionally a ground electrical potential equal to zero is applied to the anode current collector:

$$\phi_S = 0 \tag{2.33}$$

Similar to the cathode, at the anode gas channel normal flux of electrons is zero, i.e. equation (2.29). Additionally, a water vapour fraction is imposed at the channel interface:

$$x_{H_2O} = x^0_{H_2O,a} \tag{2.34}$$

A symmetric boundary condition between the top and bottom of the domain is imposed. At the symmetric boundary, the fluxes of all components are equal to zero.

2.2.8 Source Terms and Couplings

The consumption and production of hydrogen, electrons, protons, oxygen and water are all dependent on the electrochemical reaction rates within the CL micro structures. Reaction rates are resolved as current density i, in units A/cm^3. Consumption of reactant i, is determined by the normalization $\frac{i}{n_i F}$, where $\frac{1}{n_i F}$ is ratio of a reactant consumed per unit of current density, corresponding to the stoichiometric relationship (1.1). The following relationships are developed:

$$R_{O_2} = \begin{cases} \frac{i}{4F} & \text{In the CCL} \\ 0 & \text{In all other layers} \end{cases} \tag{2.35}$$

$$R_H = \begin{cases} \frac{i}{F} & \text{In the ACL} \\ 0 & \text{In all other layers} \end{cases} \tag{2.36}$$

$$R_{H_20} = \begin{cases} -\frac{i}{2F} & \text{In the CCL} \\ 0 & \text{In all other layers} \end{cases} \tag{2.37}$$

$$R_{H^+} = \begin{cases} \frac{i}{F} & \text{In the CCL} \\ -\frac{i}{F} & \text{In the ACL} \end{cases} \tag{2.38}$$

$$R_{e^-} = \begin{cases} \frac{i}{F} & \text{In the CCL} \\ -\frac{i}{F} & \text{In the ACL} \end{cases} \tag{2.39}$$

The adsorption/desorption of water vapour into the ionomer phase within the MEA is described as follows [11]:

$$R_\lambda = -k_t \frac{\rho_{dry}}{EW}(\lambda_{eq} - \lambda) \tag{2.40}$$

where k_t is a adsorption/desorption time constant, set to 10000, in order to provide a strong coupling between the membrane and the CL [11]. λ_{eq}, the equilibrium membrane water content, is described by Liu et al. [65] as follows:

$$\lambda_{eq} = \left[1 + 0.2352 a_w^2 \left(\frac{T - 303.15}{30}\right)\right] (14.22 a_w^3 - 18.92 a_w^2 + 13.41 a_w) \tag{2.41}$$

where p_{sat} is the water saturation pressure described by Springer et al. [18]:

$$\begin{aligned} log_{10}\left(P_{sat}\right) = &- 2.1794 + 0.02953\left(T - 273.15\right) - 9.1837 \times 10^{-5}\left(T - 273.15\right)^2 \\ &+ 1.4454 \times 10^{-7}\left(T - 273.15\right)^3 \end{aligned} \tag{2.42}$$

Due to the production of water within the cathode catalyst layer the water source term (2.40) is modified. The water sorption source terms for the system are as follows:

$$R_\lambda = \begin{cases} \frac{i}{2F} - k_t \frac{\rho_{dry}}{EW}(\lambda_{eq} - \lambda) & \text{In the CCL} \\ -k_t \frac{\rho_{dry}}{EW}(\lambda_{eq} - \lambda) & \text{In the ACL} \end{cases} \tag{2.43}$$

Mass conservation for any species is described as follows:

$$\frac{\partial c_i}{\partial t} = -\vec{\nabla} \cdot \vec{N}_i + R_i \tag{2.44}$$

where c_i is the concentration of a given reactant, $\vec{N}_i$ is corresponding flux of the reactant, and R_i is the source term for the reactant representing consumption or production. At steady state, the time dependent term is equal to zero, resulting in the following relationship:

$$\vec{\nabla} \cdot \vec{N}_i = R_i \tag{2.45}$$

Given the steady state mass transport and consumption relationship (2.45), the species flux terms described in Sections 2.2.3 to 2.2.6, and the source terms as described in this section, the following coupled which describe the electrochemical operation of the MEA are assembled as follows:

$$\begin{aligned}
-\vec{\nabla}\cdot\left(\frac{p_T}{RT}\, D^{eff}_{O_2,N_2}\vec{\nabla}x_{O_2}\right) &= R_{O_2} \\
-\vec{\nabla}\cdot\left(\frac{p_T}{RT}\, D^{eff}_{H_2O,N_2 \text{ or } H_2}\vec{\nabla}x_{H_2O}\right) &= R_{H_2O} - R_\lambda \\
-\vec{\nabla}\cdot\left(\frac{\sigma^{eff}_m}{F}\vec{\nabla}\phi_m\right) &= R_{H^+} \\
\vec{\nabla}\cdot\left(\frac{\sigma^{eff}_s}{F}\vec{\nabla}\phi_s\right) &= R_{e^-} \\
-\vec{\nabla}\cdot\left(n_d\frac{\sigma^{eff}_m}{F}\vec{\nabla}\phi_m + \frac{\rho_{dry}}{EW}D^{eff}_\lambda\vec{\nabla}\lambda\right) &= R_\lambda
\end{aligned} \tag{2.46}$$

Table 2.1 shows at which area of the MEA domain each equation is solved.

Table 2.1 – Table of solution variables considered in isothermal MEA model.

Solution variable	AGDL	AMPL	ACL	ML	CCL	CMPL	CGDL
Oxygen molar fraction, x_{O_2}					✓	✓	✓
Water molar fraction, x_{H_2O}	✓	✓	✓		✓	✓	✓
Solid potential, ϕ_s	✓	✓	✓		✓	✓	✓
Electrolyte potential, ϕ_m			✓	✓	✓		
Membrane water content, λ			✓	✓	✓		

The system of equations (2.46) is linearized using Newtown's method, and discretized using the Bubnov-Galerkin Finite Element Method (FEM). The linear system is solved using UMFPACK. Numerical method is explained in reference [11]. The system of equations is implemented and openly available in OpenFCST [10].

2.3 Kinetics Models

Several kinetics models are implemented in OpenFCST, i.e. the Tafel kinetics model, the double trap kinetics model, the dual path kinetics model, and finally the Butler Volmer kineitcs model. The Tafel kinetics model is commonly used to describe the ORR, and is as follows:

$$j = j_0^{ref} \left(\frac{c_{O_2}}{c_{O_2}^{ref}} \right)^{\gamma_{O_2}} \left(\frac{c_{H_+}}{c_{H_+}^{ref}} \right)^{\gamma_{H_+}} \exp \left[\frac{\alpha_c F}{RT} \Big(E_{eq} - (\phi_s - \phi_m) \Big) \right], \tag{2.47}$$

where i is the reaction rate in A/cm^2_{Pt}, i_0^{ref} is the experimentally measured reference current density, c_i and c_i^{ref} are the local and reference species concentrations, γ_i is the corresponding species reaction order, α_c is the cathodic transfer coefficient, E_{eq} is the experimentally measure equilibrium potential, and ϕ_s and ϕ_m are the electric and protonic potentials.

The dual path kinetics model, developed by Wang et al. [66], is used throughout this work to resolve HOR rates. Wang et al. [66] proposed that the HOR can be described as the contribution of two dominant pathways, the Tafel-Volmer (TV) pathway and the Heyrovsky-Volmer (HV) pathway. Assuming minimal coverages and negligible backwards reaction step, the following expression for current density is used:

$$j = j_{0T} \left(1 - e^{-2F\eta/\gamma RT} \right) + j_{0H} \left(e^{F\eta/2RT} - e^{-F\eta/\gamma RT} e^{-F\eta/2RT} \right) \tag{2.48}$$

where j_{0T} and j_{0H} are the reference current densities for the TV and HV steps respectively, $\eta = E - E^{eq}$, $E = \phi_s - \phi_m$, and γ is the potential range constant.

Kinetic parameters used in this work are described in Table 2.2. The double trap kinetic model, which is used and modified extensively in this work, is explained in detail in the following section.

2.3.1 Double Trap Kinetics Model

Evidence for the existence of a double Tafel slope has been found experimentally and studied extensively over several decades [7]. Despite the extensive research describing the changing Tafel slopes, the majority of researchers do not account for the losses from the change when performing fuel cell simulations. Wang et al. [6] proposed a kinetic model for the ORR, consisting of 4 intermediate reaction steps, each step's rate depending on associated free energies of activation. This model exhibits the

double Tafel slope behaviour, as well as predicting high coverage of oxides at low current densities and low coverage in the high current densities.

Moore [7] reformulated the double trap kinetics model developed by Wang et al. [6], correcting for the assumption of constant oxygen concentration, performing a parameter estimation of the kinetic free energies of the intermediate steps, and integrating the kinetic model with the two dimensional MEA model developed by Secanell [11]. In this work, key theory of the double trap kinetics model is described, neglecting certain details. For the full derivation please see Section 2.2.1 in reference [7].

Wang et al. [54] assumed that the ORR consists of four intermediate reaction steps. These intermediate reaction steps produce and consume two adsorbed species; O_{ads} and OH_{ads}. The four intermediate reactions are as follows:

$$1/2O_2 \Leftrightarrow O_{ads} \qquad \text{Dissociative Adsorption (DA)} \tag{2.49}$$

$$1/2O_2 + H^+ + e^- \Leftrightarrow OH_{ads} \qquad \text{Reductive Adsorption (RA)} \tag{2.50}$$

$$O_{ads} + H^+ + e^- \Leftrightarrow OH_{ads} \qquad \text{Reductive Transition (RT)} \tag{2.51}$$

$$OH_{ads} + H^+ + e^- \Leftrightarrow H_2O \qquad \text{Reductive Desorption (RD)} \tag{2.52}$$

In the first reaction (2.49), known as the Dissociative Adsorption (DA) step, oxygen is dissociatively adsorbed onto the catalyst surface, creating product and intermediate reactant O_{ads}. No electron transfer occurs, therefore this is not an electrochemical reaction and is not affected by solid or electrolyte potentials. In the second reaction (2.50), the Reductive Adsorption step (RA), oxygen is adsorbed onto the catalyst surface and reduced with protons, producing the adsorbed hydoxyl (OH_{ads}). In the third step (2.51), the Reductive Transition step (RT), O_{ads} from the DA step reacts with protons to create OH_{ads} . In the forth and final step, the Reductive Desorption step (RD), OH_{ads} is reduced with protons to form water.

Steps 2 - 4 (RA, RT, RD) are electrochemical reactions and therefore are dependent on local solid and electrolyte potentials. As for reactant dependencies: the DA step is dependent on the local concentration of oxygen, the RA step is dependent on the local concentrations of oxygen and protons, the RT step is dependent on the coverages of adsorbed oxygen and local concentration of protons, and finally, the RD step is dependent of the coverages of adsorbed hydoxyl and local concentration of protons.

Due to the reactants and products of each of the four described intermediate steps, there exists two potential pathways for the ORR as shown in Figure 2.3. The dominant pathway may change depending on overpotential and species coverages.

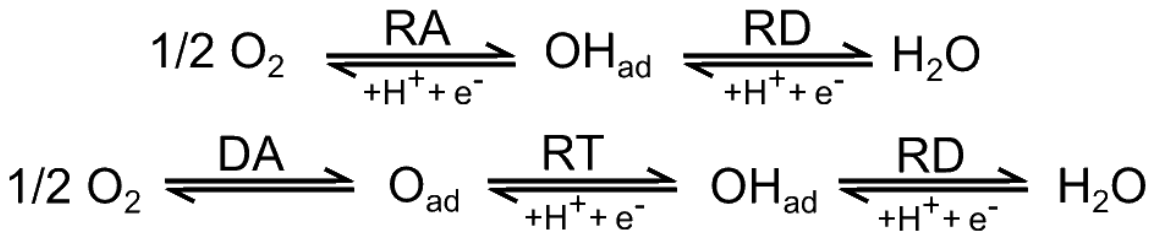

Figure 2.3 – The assumed paths and intermediate species of the ORR [6]. Figure reproduced with permission from reference [7].

The current produced by the overall ORR is composed of the rates of the intermediate electrochemical reactions:

$$j_k = F(\nu_{RA} + \nu_{RT} + \nu_{RD}) \tag{2.53}$$

In order for the RD step to occur, one of the two hydoxyl producing steps (RA, RT) must also occur. Therefore according to reaction stoichiometry every time the RD reaction occurs there has been transfer of two electrons, thus reaction current can be expressed as follows:

$$j_k = 2F\nu_{RD} = 2j_{RD} \tag{2.54}$$

Moore [7]'s derivation of the double trap kinetics model, omitted terms of proton concentration. This omission was justified by Moore [7] by assuming that proton concentration is constant within Nafion® electrolyte phase. This assumption is typically appropriate for ionomer filled agglomerates, however for water filled agglomerates proton concentration typically differs from the reference values, as it will be later shown in Section 3.4. Therefore to consider water filled agglomerates correctly using the double trap kinetics model, the formulation is derived in this work to include terms of proton concentration.

The rates of the individual reaction steps are calculated as follows:

$$j_{DA} = j^* \left(\frac{c_{O_2}}{c_{O_2}^{ref}} \right)^{\frac{1}{2}} e^{-\Delta G^*_{DA}/kT} \theta_{Pt} - j^* e^{-\Delta G^*_{-DA}/kT} \theta_O \tag{2.55}$$

$$j_{RA} = j^* \left(\frac{c_{O_2}}{c_{O_2}^{ref}} \right)^{\frac{1}{2}} \left(\frac{c_{H^+}}{c_{H^+}^{ref}} \right) e^{-\Delta G^*_{RA}/kT} \theta_{Pt} - j^* e^{-\Delta G^*_{-RA}/kT} \theta_{OH} \tag{2.56}$$

$$j_{RT} = j^* \left(\frac{c_{H^+}}{c_{H^+}^{ref}} \right) e^{-\Delta G^*_{RT}/kT} \theta_O - j^* e^{-\Delta G^*_{-RT}/kT} \theta_{OH} \tag{2.57}$$

$$j_{RD} = j^* \left(\frac{c_{H^+}}{c_{H^+}^{ref}} \right) e^{-\Delta G^*_{RD}/kT} \theta_{OH} - j^* e^{-\Delta G^*_{-RD}/kT} \theta_{Pt} \tag{2.58}$$

Where ΔG_i^* are the free energies of activation of each intermediate forward and backward reactions, θ_i are the fractional coverages of intermediate adsorbed species, and j^* is the reference prefactor for the reaction.

The individual free energies are as follows:

$$\Delta G^*_{DA} = \Delta G^{*0}_{DA}, \qquad \Delta G^*_{-DA} = \Delta G^{*0}_{DA} - \Delta G^0_O \tag{2.59}$$

$$\Delta G^*_{RA} = \Delta G^{*0}_{RA}, +\beta e\eta \qquad \Delta G^*_{-RA} = \Delta G^{*0}_{RA} - \Delta G^0_{OH} - \beta e\eta \tag{2.60}$$

$$\Delta G^*_{RT} = \Delta G^{*0}_{RT} + \beta e\eta, \quad \Delta G^*_{-RT} = \Delta G^{*0}_{RT} - \Delta G^0_{OH} + \Delta G^0_O - \beta e\eta \tag{2.61}$$

$$\Delta G^*_{RD} = \Delta G^{*0}_{RD} + \beta e\eta, \quad \Delta G^*_{-RD} = \Delta G^{*0}_{RD} + \Delta G^0_{OH} - \beta e\eta \tag{2.62}$$

The electrochemical reactions consist of a potential dependent term $\beta e\eta$, where e is the charge of a single electron (to convert from volts to electron-volts), β is the reaction symmetry factors (assumed to be 0.5), and η (equal to $E - E^{eq}$, where $E = \phi_s - \phi_m$) is the local overpotential. Each reference energy of free activation ΔG_i^{*0} was calculated by Moore [7] using parametric parameter estimation.

Due to (2.54) the total reaction current is a product of the current produced in the RD step, therefore it can be written as:

$$j_k = 2\, C_{H^+} j^* e^{-\Delta G^*_{RD}/kT} \theta_{OH} - 2 j^* e^{-\Delta G^*_{-RD}/kT} \theta_{Pt} \tag{2.63}$$

where C_{H^+} considers local proton concentration, and is equal to $\left(\frac{c_{H^+}}{c_{H^+}^{ref}} \right)$.

It is assumed that the reactions are at steady state, therefore for the two possible pathways as shown in Figure 2.3, the following relationships between coverages and intermediate reaction rates are valid:

$$\frac{\mathrm{d}\theta_O}{\mathrm{d}t} = \nu_{DA} - \nu_{RT} = 0 \tag{2.64}$$

$$\frac{\mathrm{d}\theta_{OH}}{\mathrm{d}t} = \nu_{RA} + \nu_{RT} - \nu_{RD} = 0 \tag{2.65}$$

By substituting equations (2.55) to (2.58) into the above steady state relationships (2.64) and (2.65), expressions for the coverages of intermediate species are obtained:

$$C_{O_2} g_{DA} \theta_{Pt} - g_{-DA} \theta_O - C_{H^+} g_{RT} \theta_O + g_{-RT} \theta_{OH} = 0 \tag{2.66}$$

$$C_{H^+} C_{O_2} g_{RA} \theta_{Pt} - g_{-RA} \theta_{OH} + C_{H^+} g_{RT} \theta_O + g_{-RT} \theta_{OH} - C_{H^+} g_{RD} \theta_{OH} + g_{-RD} \theta_{Pt} = 0 \tag{2.67}$$

where $g_i = e^{-\Delta G_i^* / kT}$ considers the activation state of the intermediate backward/-forward reaction, and $C_{O_2} = \left(\frac{c_{O_2}}{\frac{ref}{c_{O_2}}} \right)^{1/2}$ considers local oxygen concentration, with a reaction order or 0.5 corresponding to stoichiometry.

In order to obtain expressions for terms θ_{OH} and θ_O, equations (2.66) and (2.67) are rearranged and solved to obtain:

$$\theta_{OH} = \frac{C_{O_2} g_{DA} (C_{H^+} C_{O_2} g_{RA} + g_{-RD} - C_{H^+} g_{RT}) - (C_{H^+} C_{O_2} g_{RA} + g_{-RD})(C_{O_2} g_{DA} + g_{-DA} + C_{H^+} g_{RT})}{(C_{O_2} g_{DA} - g_{-RT})(C_{H^+} C_{O_2} g_{RA} + g_{-RD} - C_{H^+} g_{RT}) - (C_{H^+} C_{O_2} g_{RA} + g_{-RA} + g_{-RT} + C_{H^+} g_{RD} + g_{-RD})} \tag{2.68}$$

$$\theta_O = \frac{C_{O_2} g_{DA} (C_{H^+} C_{O_2} g_{RA} + g_{-RA} + g_{-RT} + C_{H^+} g_{RD} + g_{-RD}) - (C_{H^+} C_{O_2} g_{RA} + g_{-RD})(C_{O_2} g_{DA} - g_{-RT})}{(C_{O_2} g_{DA} + g_{-DA} + C_{H^+} g_{RT})(C_{H^+} C_{O_2} g_{RA} + g_{-RA} + g_{-RT} + C_{H^+} g_{RD} + g_{-RD}) - (C_{H^+} C g_{RA} + g_{-RD} - C_{H^+} g_{RT})(C_{O_2} g_{DA} - g_{-RT})} \tag{2.69}$$

Using equations (2.62), (2.63), (2.68), and (2.69) reaction rates may calculated, based on solid phase and electrolyte potentials, and oxygen concentrations.

2.3.1.1 Effect of Proton Concentration on Double Trap Kinetics Model

A parametric study of the modified double trap kinetics model was performed in order to assess the impact of proton concentration. Kinetic parameters used in this work are described in Table 2.2. Results for two proton concentrations are represented in Figures 2.4 to 2.9, the higher concentration (0.001818 mol/cm^3) corresponds to the reference concentration of sulphonic acid groups in Nafion® as shown in Table 2.2.

Figure 2.4 shows how reduced concentration of protons leads to radically different coverage profiles. For reduced proton concentrations large quantities of O_{ads} and OH_{ads} occupy the catalyst surface, due to reduced rate of the final RD step.

Table 2.2 – Electrochemical parameters for Kinetics Models

Parameter	Value
Tafel Kinetics	
j_0^{ref}, A/cm^2	$1.69278 \times 10^{-10} \exp\left(\frac{-80987.61}{8.314}\left(\frac{1}{T_c} - \frac{1}{303.15}\right)\right)$
E_{eq}, V	$(70650 + 8T_c\ln(T_c) - 92.84T_c)\frac{4.184}{2F} + \ln(5^{0.5})\frac{8.314T_c}{2F}$
α_c	1.0
γ_{O_2}	1.0
$c_{O_2}^{ref}$	$1.6 \times 10^{-5}\ mol/cm^3$
$c_{H^+}^{ref}$	$0.0018\ mol/cm^3$
Double Trap Kinetics Model	[67]
j^*	$1000.0\ A/cm^2$
G_{DA}^0	$0.3907\ eV$
G_{-DA}^0	$0.7337\ eV$
G_{RA}^0	$0.6094\ eV$
G_{-RA}^0	$1.0001\ eV$
G_{RT}^0	$0.5904\ eV$
G_{-RT}^0	$0.9811\ eV$
G_{RD}^0	$0.278\ eV$
G_{-RD}^0	$0.098\ eV$
Dual Path Kinetics Model	[66]
j_{0T}	$0.47\ A/cm^2$
j_{0H}	$0.01\ A/cm^2$
γ	1.2

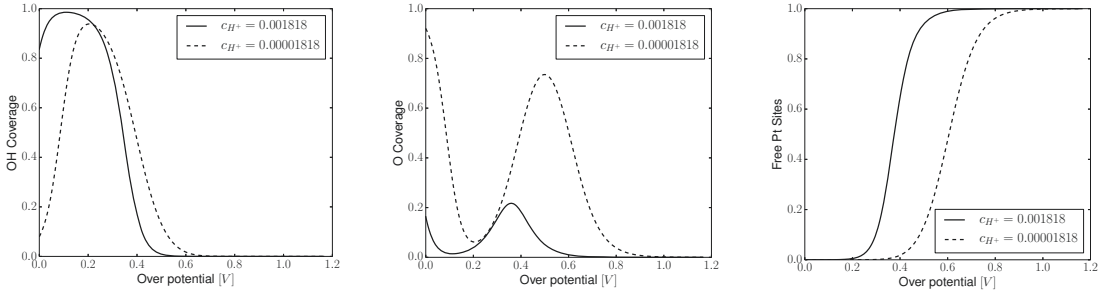

(a) OH_{ads} (b) O_{ads} (c) Free Pt

Figure 2.4 – Intermediate species coverages fractions of platinum catalyst sites calculated using double trap kinetics model, for varying proton concentrations. Units of concentration are in mol/cm^3. Coverage profiles are similar to reference [7]

Figure 2.4 shows that at lower proton concentration, higher O_{ads} coverage is observed. This is due to the reduced rate of consumption of O_{ads} by the forward RT step as seen in Figure 2.6, which is hindered by the lack of protons. The increased coverage of species O_{ads} in turn acts to increase the rate of the backward DA reaction as seen in Figure 2.5. For DA, RA, and RT intermediate reactions, the backward steps are several orders of magnitude smaller than the forward steps and therefore do not play a significant role in the production of adsorbed species, therefore the overall rate of the DA step does not change significantly depending on proton concentration.

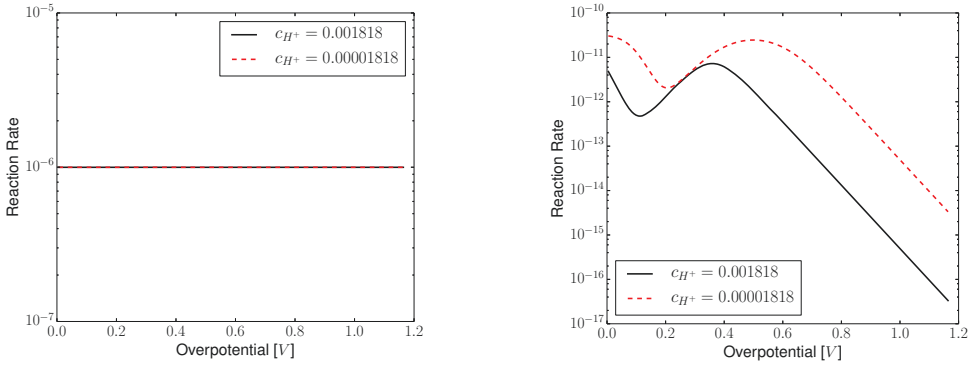

(a) Forward Reaction (b) Backward Reaction

Figure 2.5 – Reaction rates of forward and backwards DA reaction steps.

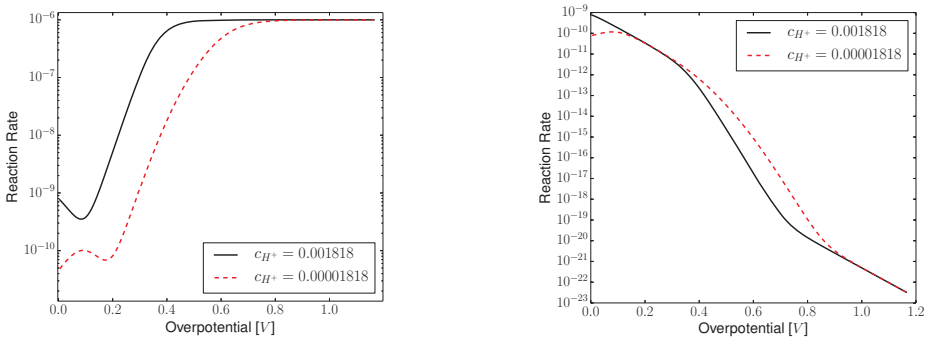

(a) Forward Reaction (b) Backward Reaction

Figure 2.6 – Reaction rates of forward and backwards RT reaction steps.

Figure 2.4 shows that for lower proton concentrations, larger OH_{ads} coverages can be observed at overpotential ranges ≥ 0.4 [V]. This is due to the reduced rate of the combined RD steps, as seen in Figures 2.5 and 2.9. Comparing RA and RT reaction rates shown in Figure 2.7 with Figure 2.6 respectively, at 0.6 [V] overpotential, it can be seen that the RA reaction step for high proton concentrations is dominant, with a higher reaction rate therefore more OH_{ads}, however at lower proton concentrations the RT step becomes more significant. This change occurs due to the following: at high proton concentrations the RT step proceeds fast enough to consume all O_{ads} produced by the DA step resulting in the low O_{ads} coverages as observed in Figure 2.4, ultimately limiting the RT steps forward rate. At low proton concentrations both RA and RT steps are severely hindered by their dependence on proton concentrations, but the rate of RT step is improved by large O_{ads} coverages.

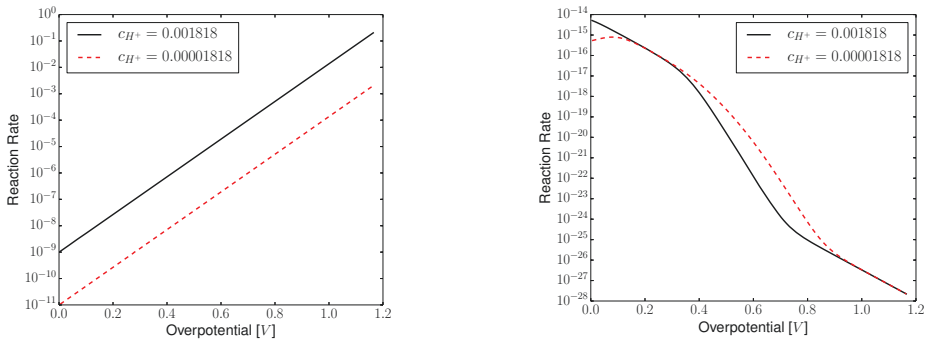

(a) Forward Reaction (b) Backward Reaction

Figure 2.7 – Reaction rates of forward and backwards RA reaction steps.

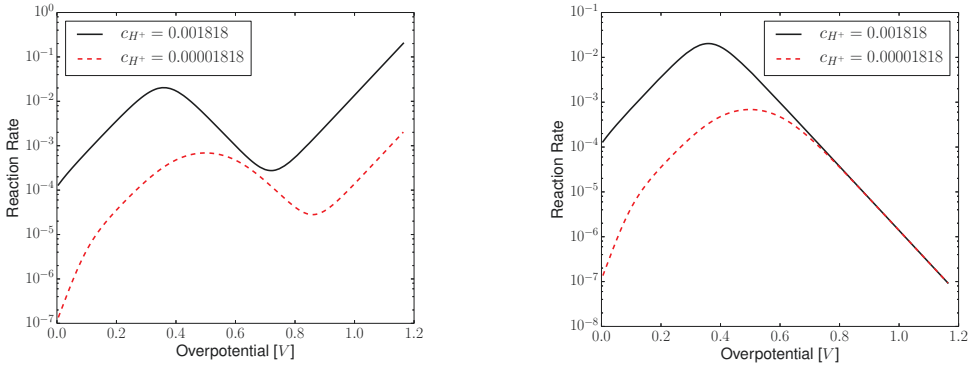

(a) Forward Reaction (b) Backward Reaction

Figure 2.8 – Reaction rates of forward and backwards RD reaction steps.

Figure 2.8 shows the backward and forward rates of the RD step. Figure 2.9 shows the overall rate of reaction, which is directly proportional to the sum of the forward and backward RD steps. It can be seen that the rate of the RD and RT steps predicted using the double trap kinetic model vary in a non linear fashion with respect to change in proton concentration. This non linear behaviour is due to the previously discussed change in dominant pathway, which changes depending on proton concentraion and overpotential. Ultimately with lower proton concentrations, the modified double trap kinetics reaction rate (2.63) produces smaller rates of reaction as seen in Figure 2.9.

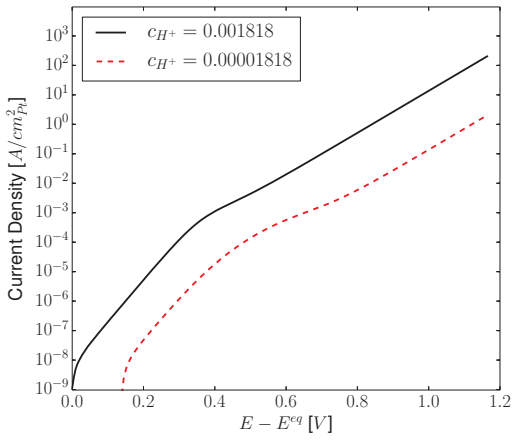

Figure 2.9 – Current density per unit area of platinum calculated using double trap kinetics model, for varying proton concentrations. Units of concentration are in mol/cm^3. **Note:** The reaction rate is given by equation (2.63), and is a combination of the forward and backward RD steps from Figure 2.8. E^{eq} is calculated for reference proton and oxygen conditions.

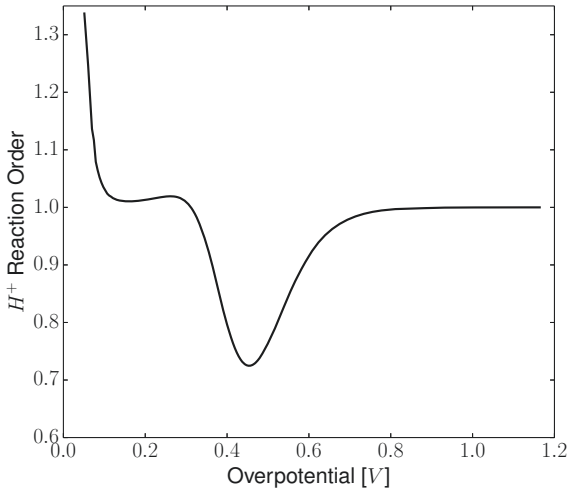

Figure 2.10 – H^+ reaction order calculated using the improved double trap kinetics model and equation (2.71)

Experimentally, the sensitivity of a reaction to a given reactant is estimated by the reaction order, which is present in the Tafel kinetics equation, recall:

$$j = j_0^{ref} \left(\frac{c_{O_2}}{c_{O_2}^{ref}} \right)^{\gamma_{O_2}} \left(\frac{c_{H^+}}{c_{H^+}^{ref}} \right)^{\gamma_{H^+}} \exp \left[\frac{\alpha_c F \eta}{RT} \right], \tag{2.70}$$

where $\gamma_{O_2}, \gamma_{H^+}$ are the reaction orders of oxygen and protons. At constant overpotential, temperature, and oxygen concentration, equation (2.70) can be rewritten as follows:

$$log(j) = log(C) + \gamma_{H^+} log \left(\frac{c_{H_+}}{c_{H^+}^{ref}} \right) \tag{2.71}$$

where C accounts for all constants. By evaluating this equation for different proton concentrations c_{H^+} the reaction order of protons γ_{H^+} can be obtained. Figure 2.10 shows the reaction order of protons over a range of overpotentials, generated using the improved double trap kinetics model. Predicted values of γ_{H^+} are similar to values reported by A. Damjanovic [68], who reported γ_{H^+} equal to 1.5 for low current densities and 1 for high current densities . Sepa et al. [69] notes that for higher proton concentration, the linear region with slope equal to -120 $\delta V/\delta\ log(i)$ is extended to lower overpotentials. The proposed model exhibits similar behaviour, as seen in Figure 2.9, where the linear region with slope $\approx$ -120 $\delta V/\delta\ log(i)$, starting at $\sim$ 0.36 V, is longer at higher proton concentrations.

2.4 Micro Scale Models

2.4.1 Introduction

Modern PEFC catalyst layers, which consist of Nafion® ionomer, and platinum loaded carbon support particles ($\sim 40\ nm$ in diameter [46, 70]), are fabricated using various techniques such as doctor blade method, and ink jet printing. Depending on the ink fabrication procedure, and ink drying process, various micro structures have been observed. For conventional catalyst layers ($\sim 10\ \mu m$ thick) carbon agglomerates are often observed [5].

Carbon agglomerates are porous structures bound together by ionomer thin films. The pore space within the agglomerates, know as primary pore space, is assumed inaccessible to the CL porous network, due to the presence of the ionomer thin film. The primary pores may be potentially filled with ionomer, or void filled [71, 72]. Wang et al. [25] proposed that these void filled primary pores become water filled during fuel cell operation. In order to ensure humidification of pores, the water filled model assumes steady state operation of a fully conditioned cell.

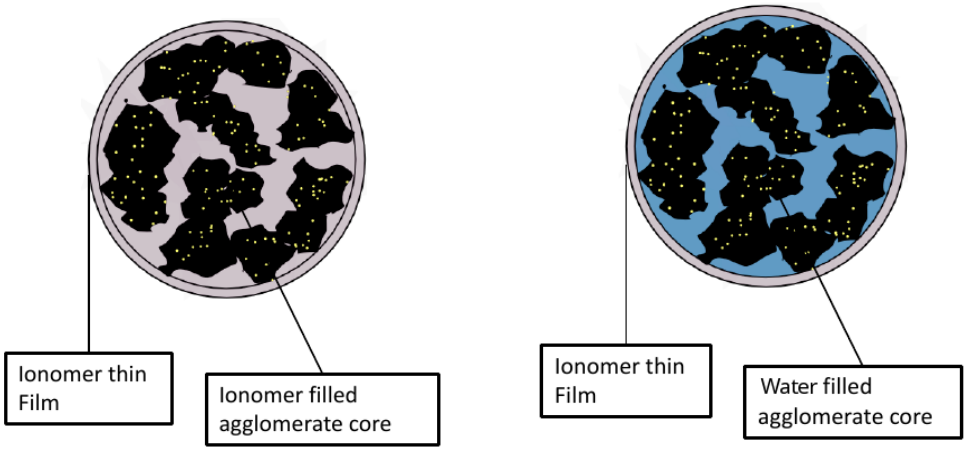

(a) Ionomer filled (b) Water filled

Figure 2.11 – Agglomerate diagrams, demonstrating porous platinum loaded carbon cores, which are filled with either water or ionomer. The core structure is surrounded by an ionomer thin film.

Therefore in PEFC CL micro structure modelling, there exists several examples of ionomer filled [5, 11, 29] and water filled [26, 66] agglomerate models . Agglomerate models developed to describe mass transport and electrochemical processes, typically make the following simplify modelling assumptions:

- Pt|Carbon agglomerates are bound together by thin ($\sim 10\ nm$) ionomer films
- The external surface of the ionomer thin films are exposed to the CL gas filled porous network
- Agglomerates geometries are described using simplified shapes, e.g. cylinders, sphere, and overlapping spheres
- The carbon and platinum within the agglomerate core are connected to a continuous CL carbon network, i.e. they are electrochemically active
- The ionomer present in the agglomerate film and/or core is connected to a continuous CL ionomer network
- The carbon agglomerates are homogeneous mixtures of platinum, carbon, and electrolyte
- Electronic and protonic potentials are constant throughout the agglomerate domain, equal to surface values (typically modelled via boundary conditions)

As mentioned in Section 2.2.4, in the multi-scale catalyst layer model acts as a coupling between the macro scale FEM MEA model developed by [11] and the micro-scale models, developed in this section. The macro scale FEM model provides the micro-scale model with local operating conditions (w.r.t. a specific location in the MEA domain), such as $\{P_{O_2}, P_{H_2}, \phi_s, \phi_m, \lambda\}$, as well as material properties and electrochemical kinetic models. The micro-scale models in turn solve for these provided operating conditions, and return values of volumetric current density to the FEM MEA model.

In this work an additional type of micro-scale model is developed: the ionomer covered catalyst particle (ICCP). Modern CL fabrication techniques result in micro structural dimensions approaching the size of the primary catalyst particles [46], therefore such structures cannot be described as agglomerates. The proposed model is developed in detail in Section 2.4.4.

Other micro-scale descriptions also exist in literature, such as catalyst layer reconstructions, typically based on FIB-SEM data, which attempt to describe CL micro structure geometry in greater detail. These models are significantly more complicated than agglomerate models, and therefore less suitable for integration in MEA simulations, due to increase computational requirements.

In the following sections the micro-scale models are introduced and improvements implemented as part of this work developed. Described micro-scale models are implemented in OpenFCST [10].

2.4.2 Ionomer Filled Agglomerate

2.4.2.1 Analytical expression

The agglomerate model described in this section, developed by Dobson [5], is an ionomer filled agglomerate model, surrounded by a thin ionomer film. During steady state operation oxygen diffuses through the ionomer film and into the agglomerate core, where it reacts. It is assumed that reaction within the agglomerate core is primarily oxygen limited. Proton transport is assumed to be very effective, therefore it is not described in the model, and a constant protonic potential across the domain equal to the surface value is assumed.

The oxygen limited problem in a porous catalyst, is solved using a method summarized by Bird et al. [73]. The rate at which oxygen is consumed within in the porous agglomerate core is as follows:

$$R_{O_2} = E_r k_c c_{O_2,\, f|c} \tag{2.72}$$

where E_r is the effectiveness factor of the core, k_c is the molar reaction rate, and $c_{O_2,\, f|c}$ is the oxygen concentration at the film|core interface. E_r is described using an analytical solution of the oxygen transport in a porous catalyst [73]:

$$E_r = \frac{1}{\phi_L}\left(\frac{1}{\tanh(3\phi_L)} - \frac{1}{3\phi_L}\right) \tag{2.73}$$

where ϕ_L is Thiele's modulus, describing the relationship between reactant consumption rates, and transport properties for a given geometry. For a spherical agglomerate, the Thiele's modulus is as follows:

$$\phi_L = \frac{r_{agg}}{3}\sqrt{\frac{k_c}{D_{O_2}^{eff}}}. \tag{2.74}$$

where $D_{O_2}^{eff}$ is the effective diffusivity of oxygen in the agglomerate core, calculated for the agglomerate core porosity ε_{agg} using the Bruggeman correlation (2.21).

The molar reaction rate k_c, is determined using the Tafel kinetics equation (2.47) as follows:

$$k_c = \frac{A_v i_0^{ref}}{4F\left(1-\varepsilon_V\right)\bar{V}_{agg} c_{O_2}^{ref}} \exp\left[\frac{\alpha_c F}{RT}\Big(E_{eq} - (\phi_s - \phi_m)\Big)\right] \tag{2.75}$$

The above formulation of k_c assumes the oxygen reaction order γ_{O_2} is equal to one, and

that the proton concentration species factor, as seen in equation (2.47), is also one. The terms A_v, $4F$, $(1-\varepsilon_V)$, and $\bar{V}_{agg}$ are applied to the kinetics equation to convert the reaction rate from A/cm^2_{Pt} to $mol/(s\ cm^3)$. A_v is the active area factor, describing the experimentally measured electrochemically active platinum surface area per unit volume of the catalyst layer. ε_v is the porosity of the catalyst layer.

The active area must be scaled correctly: firstly, in order to scale the active area from the porous catalyst layer to the catalyst layers solid phase it is divided by $(1-\varepsilon_V)$. Next, in order to scale the active area from the total agglomerate volume, to the electronically active core, it is divided by $\bar{V}_{agg}$, which is described as follows:

$$\bar{V}_{agg} = \frac{V_{core}}{V_{agg}} = \frac{\frac{4\pi r_{agg}^3}{3}}{\frac{4\pi(r_{agg}+\delta_{agg})^3}{3}} = \frac{r_{agg}^3}{(r_{agg}+\delta_{agg})^3} \tag{2.76}$$

The radius, film thickness, and porosity of a spherical agglomerate are related to CL ionomer volume fractions by the following expression:

$$\varepsilon_N^{CL} = \frac{4}{3}\pi n[r_{agg}^3\varepsilon_{agg} + ((r_{agg}+\delta_{agg})^3 - r_{agg}^3)] \tag{2.77}$$

where n is the number of agglomerates per unit volume of the catalyst layer, calculated as follows:

$$n = \frac{\varepsilon_S^{CL}}{\frac{4}{3}\pi r_{agg}^3(1-\varepsilon_{agg})} \tag{2.78}$$

Two of the following variables $\{r_{agg}, \delta_{agg}, \varepsilon_{agg}\}$ must be supplied as input parameters for equation (2.77), which in turn is solved to find the third unknown. A linear analytical expression for unknown variable $\{\delta_{agg}, \varepsilon_{agg}\}$ cannot be obtained, therefore equation (2.77) must be solved using iterative methods. In this work Newton's method is used to solve the non linear equation.

The concentration of oxygen at the agglomerate core surface $c_{O_2,\,f|c}$, required by equation (2.72), depends on the mass transport limiting effects of the ionomer thin film. For a spherical shell, Fick's law (2.8) may be written as follows:

$$\frac{\mathrm{d}c_{O_2}}{\mathrm{d}r} = \frac{N_{O_2}}{D_{O_2,N}} = \frac{1}{4\pi r^2}\frac{F_{O_2}}{D_{O_2,N}}, \tag{2.79}$$

where N_{O_2} is the flux of oxygen.

For steady state operation, the reactant consumption rate must be matched by the total flux through the film, i.e.:

$$F_{O_2} = N_{O_2} \cdot 4\pi r^2. \tag{2.80}$$

Combining equations (2.80) and (2.79), substituting for N_{O_2}, and integrating over the thin film domain, the concentration of oxygen at agglomerate film|core interface is as follows:

$$c_{O_2,\, f|c} = c_{O_2,\, g|f} - \frac{\delta_{agg}}{r_{agg}\left(r_{agg} + \delta_{agg}\right)} \frac{F_{O_2}}{4\pi D_{O_2,N}}, \tag{2.81}$$

where $c_{O_2,\, g|f}$ is the oxygen concentration at the gas/ionomer film interface at the outer boundary of the agglomerate, and is obtained with using Henry's law (2.24).

Total oxygen consumption within the agglomerate core is described as follows:

$$F_{O_2} = R_{O_2} V_{agg} = E_r k_c c_{O_2,\, f|c} \left(\frac{4\pi r_{agg}^3}{3}\right). \tag{2.82}$$

Combining equations (2.82) and (2.81), an expression for the concentration at the inner boundary is obtained:

$$c_{O_2,\, f|c} = c_{O_2,\, g|f} \left[\frac{\delta_{agg} r_{agg}^2}{3\left(r_{agg} + \delta_{agg}\right)} \frac{E_r k_c}{D_{O_2,N}} + 1\right]^{-1}, \tag{2.83}$$

equation (2.72) is modified to express the total current produced by the agglomerate volume,

$$i_{agg} = 4F\bar{V}_{agg} E_r k_c c_{O_2,\, f|c}. \tag{2.84}$$

Combining equations (2.83) and (2.84), the final expression for the agglomerate current density is obtained as:

$$i_{agg} = 4F\bar{V}_{agg} \frac{P_{O_2}}{H_{O_2,N}} \left[\frac{1}{E_r k_c} + \frac{\delta_{agg} r_{agg}^2}{3\left(r_{agg} + \delta_{agg}\right) D_{O_2,N}}\right]^{-1}. \tag{2.85}$$

In order to quantify the impact of micro-scale mass transport limitations, an effectiveness factor is developed as follows:

$$E = \frac{i_{agg}}{i_{ideal}} \tag{2.86}$$

where i_{ideal} is the current that would be produced by the agglomerate, if the mass transport was infinitely fast, given as:

$$i_{ideal} = 4F\bar{V}_{agg}k_c c_{O_2,\,g|f} \tag{2.87}$$

2.4.2.2 Numerical Model

The analytical agglomerate model presented in Section 2.4.2.1 has several limitations:

- The oxygen reaction order, γ_{O2}, must be equal to 1. Experimentally however, the oxygen reaction order has been observed at values less than 1 [41, 42, 74, 75].
- Transport and electrochemical properties across the agglomerate core must be constant
- Proton transport mechanisms are not modelled, and protonic potential is assumed constant
- Oxygen dissolution from the gas phase to the ionomer thin film is assumed to be an equilibrium process

These limitations inspired the development of a more flexible numerical ionomer filled agglomerate, developed by Dobson [5]. The numerical model addresses the limitation stated above, allowing use of different kinetics models, varying domain properties, analysis of proton transport processes, and non equilibrium boundary conditions. The transport of species $\{O_2, H_2, H^+\}$ are describe using the steady state mass balance (2.45). Determination of individual fluxes is described in proceeding paragraphs.

Protonic charge transport, in the ionomer thin film and ionomer filled core, is described using the Ohms Law, i.e. equation (2.2), since convective transport can be assumed negligible ($\vec{v} \approx 0$), and diffusive flux can be assumed negligible since proton concentration is equal to the concentration of homogeneously distributed sulphonic groups in Nafion® i.e., $c_{H^+} = c_{SO_3^-}$. Therefore proton charge transport in the ionomer filled agglomerate is described as follows:

$$\vec{N}_{H^+} = -\frac{\sigma_m^{eff}}{F}\vec{\nabla}\phi_m, \tag{2.88}$$

where σ_m^{eff} is the proton conductivity, determined using equation (2.19), with values of λ supplied by the macro scale model, modifying the Bruggeman correction to use ε_{agg} (agglomerate porosity) instead of ε_N (macro scale Nafion® volume fraction).

The consumption and production of protons, sorbed oxygen, and sorbed hydrogen, are calculated throughout the agglomerate core domain as follows:

$$R_i = \pm\frac{jA_{v,agg}}{n_i F} \tag{2.89}$$

where current density j A/cm^2_{Pt}, is dependent on a combination of local reactant concentrations $\{c_{H_2}, c_{O_2}, c_{H^+}\}$ and the local electrolyte and solid phase potentials $\{\phi_m, \phi_s\}$, and is calculated using the kinetics models as described in Section 2.3, and $A_{v,agg}$ is the volumetric active platinum surface area scaled to the agglomerate as follows:

$$A_{v,agg} = \frac{A_v}{(1-\varepsilon_V)\,\bar{V}_{agg}} \tag{2.90}$$

Combing proton flux (2.88) and source term (2.89) in the steady state mass balance relationship (2.45), a expression for the change in protonic potential is obtained:

$$-\vec{\nabla}\cdot\left[\sigma_m^{eff}\vec{\nabla}\phi_m\right] = \pm\frac{i}{F}. \tag{2.91}$$

The right hand side of equation (2.91) will be negative for the cathodic reaction (due to the consumption of protons), and positive for the anodic reaction (due to production of protons).

Convective reactant (oxygen or hydrogen) flux is assumed negligible, therefore, flux is described using Fick's Law (2.8). The core consists of a porous platinum loaded carbon network filled with ionomer. Effective transport properties within the core are calculated using Bruggeman relation (2.21). In the ionomer thin film bulk diffusive properties are used. Agglomerate radius, film thickness, and porosity are calculated by the same methods as described for the analytical expression.

Combing Fick's Law (2.8) with the reactant source term (2.89) in the steady state mass balance relationship (2.45), the following expression is obtained to analyze reactant transport,

$$\vec{\nabla} \cdot \left[D_i^{eff} \left(\vec{\nabla} c_i \right) \right] = \frac{i}{z_i F}. \tag{2.92}$$

where reactant i is oxygen for the agglomerates existing in the cathode, and hydrogen for the anode.

Dirchlet boundary conditions are applied for solution $\{c_{O_2}, c_{H_2}, \phi_m\}$. The values are determined using values of $\{P_{O_2}, P_{H_2}, \phi_m\}$ supplied by the multi-scale catalyst layer model. Concentrations of gaseous reactants oxygen and hydrogen which dissolve into the ionomer thin film are typically calculated using Henry's law (2.24). In using Henry's law it is assumed that the dissolution of gaseous species into the ionomer thin film is an equilibrium process, however this may not be truly representative of actual mass transport phenomena occurring at the ionomer thin film interface.

Suzuki et al. [48] proposed a non equilibrium boundary condition, where oxygen dissolution is based on a dissolution kinetic model. An expression for the flux of oxygen between the two phases is as follows:

$$N_{O_2} = -k_{O_2}(c^{eq}_{O_2,\, g|f} - c_{O_2,\, g|f}), \tag{2.93}$$

where N_{O_2} is the flux of oxygen between the two phases, k_{O_2} is the dissolution reaction rate constant, $c^{eq}_{O_2,\, g|f}$ is the equilibrium concentration computed using Henry's Law , and $c_{O_2,\, g|f}$ is the oxygen concentration existing at the gas|film interface. Values for the dissolution reaction rate constant were obtain experimentally by Suzuki et al. [48] by observing oxygen-limited kinetic behaviour of the ORR on planar electrodes.

Solid phase, ϕ_s, is assumed to be constant across the agglomerate, therefore reactant transport and charged species transport, coupled with consumption source terms, is described by by equations (2.91), (2.92), (2.8),(2.88). Due to one dimensional spherical symmetry, the system of equations is expressed in spherical coordinates, as follows:

$$
\begin{aligned}
&\text{Oxygen:} \quad \begin{cases} \dfrac{\partial c_{O_2}}{\partial \hat{r}} &= \dfrac{\hat{N}_{O_2}}{D_{O_2}^{eff}}, \\ \dfrac{\partial \hat{N}_{O_2}}{\partial \hat{r}} &= -\dfrac{2}{\hat{r}}\hat{N}_{O_2} + \dfrac{r_{agg}^2}{4F} i, \end{cases} \\
&\text{Protons:} \quad \begin{cases} \dfrac{\partial \phi_m}{\partial \hat{r}} &= \dfrac{F}{\sigma_m^{eff}}\hat{N}_{H^+}, \\ \dfrac{\partial \hat{N}_{H^+}}{\partial \hat{r}} &= -\dfrac{2}{\hat{r}}\hat{N}_{H^+} \pm \dfrac{r_{agg}^2}{F} i, \end{cases}
\end{aligned}
\tag{2.94}
$$

where $\hat{r} = \frac{r}{R_agg}$, $R_{agg} = r_{agg} + \delta_{agg}$, and $\hat{N}_i = -N_i R_{agg}$. These dimensional transformations are performed in order to increase numerical stability of the entire system.

To solve the system of ordinary differential equations the software package COLDAE[76] is used. COLDAE, developed in FORTAN 77, is a numerical solver capable of solving systems of boundary value mixed order fully implicit boundary-value ODEs. COLDAE uses piecewise polynomial collocation method to solve ODE systems. For the given system of equations (2.94), COLDAE permits fast evaluation, making full scale multi-scale simulations with embedded numerical micro-scale models computationally feasible. Unlike the analytical expression of the ionomer filled agglomerate, the numerical expression contains many implicit terms, which are made possible using a numerical solver.

At high current operating conditions, low values of reactant concentration due to reactant starvation, result in poor numerical stability of the discussed model, due to reduced floating point number accuracy. As mentioned before, several dimensional transformations are applied to the model in order to increase the magnitude of the solution variable. The reformulation significantly improved convergence, however under certain operating conditions convergence issues are still prevalent. To further improve convergence an initial solution framework is implemented, as discussed in Section Appendix A:

Once the solutions for reactant and electric potential have been obtained, post processing is performed to calculate the overall volumetric current density produced by the agglomerate as follows:

$$
i_{agg} = \frac{1}{V_{agg}} \int_0^1 \frac{4}{3}\pi(\hat{r}R_{agg})^3 j(\hat{r}) A_{v,agg}\, d\hat{r} \tag{2.95}
$$

Similar to the analytical ionomer filled agglomerate model, effectiveness E is calculated using equation (2.73), where i_{ideal} is as follows:

$$i_{ideal} = \frac{V_{core}}{V_{agg}} j(\hat{r} = 1) A_{v,agg} \tag{2.96}$$

2.4.2.3 Graded Agglomerates

Typically it is assumed that the platinum active catalyst reaction sites (active area) are homogeneously distributed throughout the agglomerate core. This assumption however is a simplification of the actual micro-scale morphology. Banham et al. [77, 78] reported that platinum may reside on the surface or within the carbon support material as discrete particles, depending on choice of catalyst support material. Cetinbas et al. [27] modelled discrete platinum particles within an ionomer filled agglomerate and reported their inclusion to be significant in predicting performance losses due to low Pt loading, however this work was not performed within a multi-scale framework, and model parameters r_{agg}, δ_{agg} used are unrealistically large, therefore further analysis is warranted.

The previously developed agglomerate models included in this work are based on diffusion through a one dimensional domain and therefore cannot be modified to describe the discrete catalyst particles within the agglomerate core. The existing numerical agglomerate models can however be modified to grade the distributions of active area within the agglomerate core as proposed by Jain et al. [22].

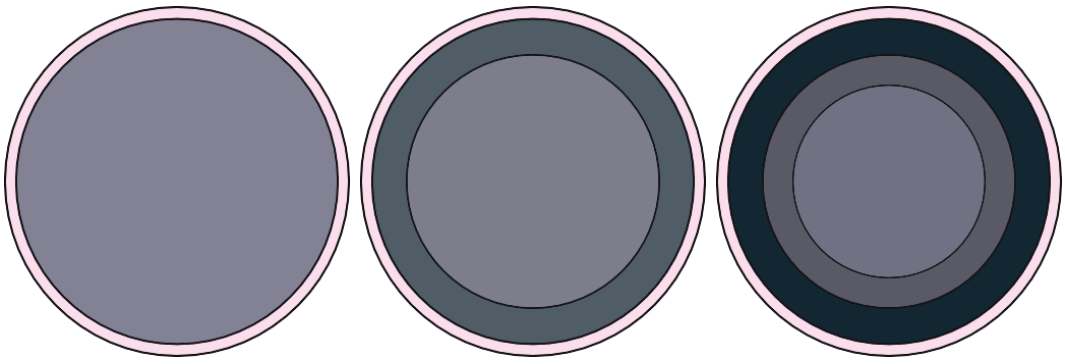

(a) Homogeneous Core (b) 2 Domain Graded Core (c) 3 Domain Graded Core

Figure 2.12 – Graded agglomerate diagrams. Platinum is distributed throughout the domain whilst total amount of platinum is conserved.

In this work the agglomerate core is subdivided into shells, each with different platinum densities, as visualized in Figure 2.12. The reaction source term (2.95) is modified, replacing the constant term of active area A_v, with a location dependent function $A_v(r)$. The density of platinum in each spherical shell is determined by associated weight w_i. Using a set of weights, platinum is redistributed throughout the agglomerate core, whilst conserving the total original amount of active area.

Firstly given a number of platinum loading weights, n_w, the outer radial position of each corresponding shell is calculated as follow:

$$r_i = \frac{r_{agg}}{n_w}\, i \qquad \text{for} \quad i = 1, 2, ..., n_w \tag{2.97}$$

Then a cumulative weight W, based on the list of supplied weight w_i is calculated as follows:

$$W = \sum_{i=1}^{n} w_i \frac{4}{3}\pi(r_i^3 - r_{i-1}^3) \qquad \text{for} \quad i = 1, 2, ..., n. \quad r_0 = 0 \tag{2.98}$$

The cumulative weight W is used to normalize the product of the total active area A_v and the associated weights w_i in order to conserve A_v throughout the agglomerate core. Finally the value for active area in each shell $A_{v,\,i}$, is calculated as follows:

$$A_{v,\,i} = \frac{w_i \cdot A_v \cdot V}{W} \qquad \text{for} \quad i = 1, 2, ..., n \tag{2.99}$$

where V is the volume of the agglomerate core. Now using $A_v(r)$, the value of active area using in equation (2.95) may change depending on radial position r. Model performance for various agglomerate active area gradings is assessed in Section 3.3.3.

2.4.3 Water Filled Agglomerate

2.4.3.1 Numerical Model

The numerical water filled agglomerate model, developed by Wang et al. [25], is similar to the numerical ionomer filled model presented in Section 2.4.2.2. Reactant (oxygen or hydrogen) transport is described using Fick's Law (2.8). Same as the numerical ionomer filled model. Experimentally determined bulk diffusion coefficients are used to describe the transport of reactants in the ionomer thin film, whilst the Bruggeman correlation (2.21) is used to compute effective transport properties within the water filled porous core.

Within the water filled core proton transport is described using the Nernst Plank equation (2.1). =

$$\vec{\nabla} \cdot \left[D^{eff}_{H^+,H_2O} (\vec{\nabla} c_{H^+} + \frac{F}{RT} c_{H^+} \vec{\nabla} \phi m) \right] = \pm \frac{i}{F} \tag{2.100}$$

where convective transport has been assumed negligible. In order to describe the gradient of electrolyte potential within the water filled domain, Poisson's equation is used:

$$\vec{\nabla}^2 \phi_m = \frac{-F}{\varepsilon \varepsilon_0} (c_{I^+} - c_{I^-}) \tag{2.101}$$

where ε_0 is the electrostatic permittivity of free space, ε is the relative permittivity of the medium, in this case water, c_{I^+} and c_{I^-} are the concentration of positively charged and negatively charged ionic species. Within the ionomer thin film the concentration of negative ionic groups is equal to the concentration of sulphonic groups in Nafion, i.e. $c_{I^-} = c_{SO_3^-}$, and within the water filled core this value is typically equal to zero but may be modified to represent the presence of surface charge existing on carbon surfaces [26]. The concentration of positively charged ions throughout the domain is equal to the unknown proton concentration, i.e. $c_{I^+} = c_{H^+}$.

The final system of equations in spherical coordinates is as follows:

$$\begin{aligned}
&\text{Oxygen:} && \begin{cases} \frac{1}{r^2} \frac{\partial}{\partial r} \left(r^2 \vec{N_{O_2}} \right) = \frac{i}{4F}, \\ \vec{N_{O_2}} = D^{eff}_{O_2} \frac{\partial c_{O_2}}{\partial r}, \end{cases} \\
&\text{Protons:} && \begin{cases} \frac{1}{r^2} \frac{\partial}{\partial r} \left(r^2 \vec{N_H} \right) = \frac{i}{F}, \\ \vec{N_H} = D^{eff}_H \left(\frac{\partial}{\partial r} c_H + \frac{F}{RT} c_H \vec{P} \right) + \frac{r^2_{agg}}{F} i, \end{cases} \\
&\text{Protonic Potential:} && \begin{cases} \frac{1}{r^2} \frac{\partial}{\partial r} \left(r^2 \vec{P} \right) = \frac{-F}{\varepsilon \varepsilon_0} \left(c_{H^+} - c_{I-} \right), \\ \vec{P} = \vec{\nabla} \phi_m, \end{cases}
\end{aligned} \tag{2.102}$$

Again the system of equations (2.102) is solved using COLDAE, resolving $\{c_{O_2}, c_{H^+}, N_{O_2}, N_{H^+}, \phi_m, \vec{\nabla}\phi_m\}$ throughout the water filled agglomerate domain. The final current density produced by the agglomerate i_{agg} is calculated using equation (2.95), agglomerate effectiveness E is calculated using equation (2.73), and ideal current density i_{ideal} using equation (2.96).

Improvements made to the numerical ionomer filled agglomerate model (catalyst grading, non-equlibrium boundary condition, initial solution framework, and parallelization) were also implemented for the water filled agglomerate mode. Improvements in convergence allow for a comprehensive characterization of the water filled agglomerate model to be performed in this work - Section 3.4. Finally improvements to the double trap kinetics equation described in Section 2.3 allow for evaluation of the water filled model using Double trap kinetics for the first time.

2.4.4 Ionomer Covered Catalyst Particle

Many recent studies of PEFC CL micro structure report structural dimensions of the order of ~ 50 nm [5, 46]. These dimensions are similar to the size of common catalyst support materials, Vulcan XC-72R ≈ 40 [nm] [46], and Ketjenblack ≈ 40 [nm] [70]. For low surface area carbons, platinum has been observed to reside on the outer surface [77, 78]. Therefore the following PEFC micro structure is proposed. The Ionomer Covered Catalyst Particle (ICCP): an individual carbon support particle, with platinum residing on it's surface, surrounded by a thin ionomer film. The model described in this section is developed to assess such structures.

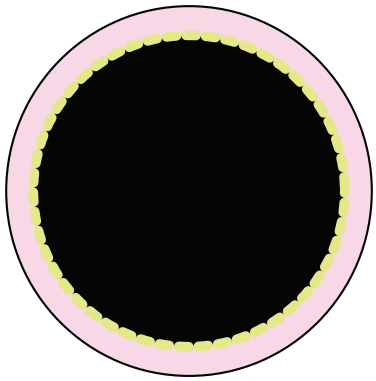

Figure 2.13 – Diagram of ICCP. Assumed structure is spherical carbon particle, with even distribution of platinum on exterior carbon surface, surrounded by a thin ionomer film.

The Ionomer Covered Catalyst Particle model presented in this section assumes a single spherical carbon particle, surrounded by an ionomer thin film. The surface of the sphere is uniformly covered with platinum. Oxygen must diffuse into the ionomer

thin film, to the spherical surface where it will react on the platinum catalyst surface. Volumetric current density of the simple catalyst particle is obtained as follows:

$$i_{agg} = \frac{j(c_{O_2,\,f|c}) \cdot A_s}{V} = \frac{j(c_{O_2,\,f|c}) \cdot A_s}{\frac{4}{3}\pi r_{agg}^3} \tag{2.103}$$

where $j(c_{O_2,\,f|c})$ is the current per unit area of platinum, calculated using kinetics models as discussed in section 2.3, a function of the oxygen concentration at the ionomer film|carbon interface $c_{O_2,\,f|c}$, and A_s is the total active platinum surface area, calculated as follows:

$$A_s = A_v V = A_v \frac{4}{3}\pi r_{agg}^3 \tag{2.104}$$

In order to obtain the current produced by the Ionomer Covered Catalyst Particle, the concentration of oxygen at the catalyst surface must be resolved. As before diffusive flux of oxygen in Nafion® is described using Fick's law in spherical coordinates, assuming spherical symmetry:

$$N_{O_2} = -D_{O_2,N} \frac{dc_{O_2}}{dr} \tag{2.105}$$

At steady state the total consumption of oxygen must be equal to the total flux through the spherical surface, as follows:

$$F_{O_2} = -N_{O_2}.4\pi r^2 \tag{2.106}$$

Therefore the change in concentration in a spherical domain can be described as follows:

$$\frac{dc_{O_2}}{dr} = \frac{1}{4\pi r^2} \frac{F_{O_2}}{D_{O_2,N}} \tag{2.107}$$

Integrating equation (2.107) across the thickness of the ionomer thin film an expression for the difference in oxygen concentrations at the ionomer surface $(r_{agg} + \delta_{agg})$ and Nafion|carbon interface (r_{agg}) is obtained:

$$\int_{r_{agg}}^{(r_{agg}+\delta_{agg})} dc_{O_2} = \frac{F_{O_2}}{4\pi D_{O_2,N}} \int_{r_{agg}}^{(r_{agg}+\delta_{agg})} \frac{1}{r^2} dr \tag{2.108}$$

$$\frac{c_{O_2,\,g|f} - c_{O_2,\,f|c}}{\delta_{agg}} = \frac{1}{r_{agg}(r_{agg} + \delta_{agg})} \frac{F_{O_2}}{4\pi D_{O_2,N}} \tag{2.109}$$

The total oxygen consumption due to the electrochemical reaction is as follows:

$$F_{O_2} = \frac{j(c_{O_2,\,f|c}) \cdot A_s}{4F} \tag{2.110}$$

Finally an expression for the in turnal oxygen concentration is obtained:

$$c_{O_2,\,f|c} = c_{O_2,\,g|f} - \frac{\delta_{agg}}{r_{agg}(r_{agg} + \delta_{agg})} \frac{j(c_{O_2,\,f|c}) \cdot A_s}{16F\pi D_{O_2,N}} \tag{2.111}$$

Equation (2.111) is a non linear equation, since it contains an implicit expression of current density $j(c_{O_2,\,f|c})$. Therefore equation (2.111) must be solved iteratively using Newton's method.

Newtons method is as follows: firstly any equation can be expressed as a residual, as follows:

$$R(u) = 0 \tag{2.112}$$

where u is the solution variable of residual function R. Applying an infinitesimal perturbation and a Taylor expansion the following relationship is obtained:

$$R(u^{n+1}) = R(u^n + \delta T) = R(u^n) + \frac{\partial R(u^n)}{\partial u}(\delta u) + \mathcal{O}(\delta u^2) \tag{2.113}$$

where δu is the variation of the solution. The second order terms are neglected $\mathcal{O}(\delta u^2)$, and since $R(u^{n+1}) = 0$ the linearized equation becomes:

$$\frac{\partial R(u^n)}{\partial u}\,(-\delta u) = R\,(u^n) \tag{2.114}$$

The variation of u, δu, is iteratively solved to find a new solution u^{n+1}, as follows:

$$u^{n+1} = u^n + \delta u \tag{2.115}$$

where

$$\delta u = -\frac{R\,(u^n)}{R'(u^n)} \tag{2.116}$$

The Newton step process, equation (2.115), is repeated until the residual $R(u^{n+1})$ is sufficiently close to zero, i.e. the obtain solution of u satisfies condition (2.112).

The concentration of oxygen at the gas|Nafion® interface $c_{O_2,\,g|f}$ may be obtained using two different assumptions. Firstly if an equilibrium adsorption process of gaseous oxygen into Nafion® is assumed then $c_{O_2,\,g|f}$ may be described using Henry's law - equation (2.24). In this case equations (2.24), (2.103), (2.111) can be solved to determine volumetric current density.

Alternatively the boundary condition proposed by Suzuki et al. [48], discussed in Section 2.4.2.2, can be used, recall:

$$N_{O_2} = -k_{O_2}(c_{O_2} - c_{O_2}^{eq}) \tag{2.117}$$

where k_{O_2} is the experimentally measured dissolution rate coefficient, and $c_{O_2}^{eq}$, the equilibrium oxygen concentration, is obtained using Henry's law. In this case equation (2.111) is valid, however a new expression is needed for $c_{O_2,\,g|f}$.

At steady state the total flux of oxygen through oxygen through the gas |film interface is equal to the rate of consumption:

$$R_{O_2} 4\pi r_{agg}^2 = N_{O_2}(r_{agg} + \delta_{agg}) 4\pi (r_{agg} + \delta_{agg})^2 \tag{2.118}$$

where R_{O_2} is the reactant consumption rate at the carbon surface per unit area surface:

$$R_{O_2} = \frac{j(c_{O_2,\,f|c}) \cdot A_s}{4F \cdot 4\pi r_{agg}^2} \tag{2.119}$$

Combining equations (2.117), (2.118), (2.119) an expression for $c_{O_2,\,g|f}$ is obtained as:

$$c_{O_2,\,g|f} = c_{O_2,\,g|f}^{eq} - \frac{j(c_{O_2,\,f|c}) \cdot A_s}{16F \cdot \pi (r_{agg} + \delta_{agg})^2 k_o} \tag{2.120}$$

Equation (2.111) can be combined with Henry's Law (2.24) or the derived expression for the non equilibrium boundary case (2.120), linearized and solved using Newton's method. Finally the obtained value for $c_{O_2,\,f|c}$ is used with equation (2.103) to obtain volumetric current density.

2.4.5 Poly Disperse Micro Structure Distributions

A wide range of experimentally measured agglomerate sizes have been reported to date [5]. Values in the range of 50 nm to 1000 nm have been observed. Epting et al. [46] obtained agglomerate radii distribution using x-ray scanning techniques. Based on this work, Epting and Litster [1] calculated micro-scale reaction rates based on a combination of ionomer filled agglomerates, using model developed by Sun et al. [29]. Epting states that poly-disperse agglomerate size distributions have a significant effect on the accuracy of PEFC simulations, and that significant errors are encountered when a mono-disperse system is assumed.

Epting and Litster [1] assume that the boundary oxygen concentration and electric potentials of every agglomerate is the same. With this assumption a connected system of agglomerates is not truly studied, but instead a consolidation of agglomerate models operating in isolation. Crucial features of the multi-scale macro/micro-scale interactions, such as the varying reactant and potential profiles are not considered. Therefore the topic of poly disperse radii distributions warrants further efforts. Furthermore, besides a dimensional distribution of micro structures existing, a distribution of different types of micro structure morphology may also exist, e.g. single carbon particles, bodies of pure nafion, or carbon agglomerates.

In this work a poly disperse agglomerate framework is developed, whereby a combination of different agglomerates can be considered in a MEA simulation. The combination may include any type of micro structure implemented in OpenFCST. Several instances of the same type of micro structure may be described, each with unique structural parameters. Current density i_{tot} for the combination of micro structures is calculated as follows:

$$i_{tot} = \sum_i i_j v_j \tag{2.121}$$

where i_j is the current density produced by corresponding micro structure j and v_j is the corresponding volume fraction that micro structure type.

Using the developed framework, the effects of agglomerate size distributions described by Epting and Litster [1] are considered in a full multi-scale MEA simulation for the first time. Results are presented in Section 3.3.5. Additionally the combination of different micro structural morphologies is explored in 3.6 .

Chapter 3

Results

3.1 Introduction

The purpose of PEFC reaction and transport modelling is to better understand PEFC performance. To this effect micro-scale models are employed to better characterize the mass transport limited operating region. In this section micro-scale mass transport mechanisms are explored, with focus applied to the following questions:

- How do mass transport mechanisms affect micro-scale model performance?
- How does micro-scale model performance affect the macro-scale catalyst layer model?
- For what range of operating conditions and parameters are micro-scale transport phenomena significant?
- Is the mathematical description of MEA structure and transport phenomena an accurate description?

Throughout this section simulation results[1] are performed using parameters described in Section 3.2. Model parameters were experimentally determined for MEA provided by the National Research Council Canada - Institute for Fuel Cell Innovation (NRC-IFCI) [5, 7, 12]. Experimental data for this MEA was published previously by [5]. MEA performance data is available as polarization curves sets for given operating conditions (varying relative humidity, operating temperatures, and pressures).

[1] Areas of analysis performed in Sections 3.3.2, 3.3.4 have been published in reference [67], and were contributions by the author of this work. Moore was primarily responsible for kinetics, and non equilibrium boundary conditions, whilst Wardlaw was responsible for analysis of proton conductivity and comparison of numerical and analytical agglomerate models.

3.2 Base Parameters

The following parameters are used in individual agglomerate and multi-scale MEA simulations, unless otherwise stated. As discussed in the previous section MEA parameters are determined experimentally [5, 7, 12], and corresponding polarization curves are available for comparison [5]. Layer and micro structural properties described in Table 3.4 are results of the agglomerate assumption and properties described in Tables 3.2, and 3.3.

Unless otherwise stated the anode catalyst layer is typically described using a multi-scale catalyst layer model with embedded ionomer filled agglomerates, using the dual path kinetics model to determine HOR rates. The cathode catalyst layer is typically described using a multi-scale catalyst layer model with embedded ionomer filled agglomerates, using the double trap kinetics model to determine ORR rates. All kinetic parameters are described in Table 2.2.

Table 3.1 – Electrode geometry

Parameter	**Value**
Channel width	0.1 cm
Current collector width	0.1 cm
GDL thickness, L^{gdl}	250 μm
MPL thickness, L^{mpl}	50 μm
CCL thickness, L^{ccl}	10 μm
ACL thickness, L^{acl}	3.33 μm
Membrane thickness, L^{m}	25 μm

Table 3.2 – GDL, MPL, and CL physical properties

Parameter	**Value**
Constants	
ρ_{Pt}	21.5 g/cm^3, [43]
ρ_c	1.25 g/cm^3, estimated in-house using MIP
ρ_N	2.0 g/cm^3, [43]
Membrane Properties	
EW	1100 g/mol
GDL physical properties	
ϵ_{th}	0.118
μ_{XX}	0.785 [80]
μ_{YY}	0.521 [80]
ϵ_V^{gdl}	0.6
MPL physical properties	
ϵ_V^{mpl}	0.4
ϵ_{th}	0.118
μ	2 [81]
CL physical properties	
ϵ_{th}	0.25884, estimated from [82]
μ	2.0
Nafion® loading,	30 %wt
$Pt\|C$	0.46
m_{Pt}	400 mg/cm^3

Table 3.3 – Electrochemical, transport, and global constants for the agglomerate simulations.

Description	Variable	Value
Agglomerate structure		
Agglomerate radius	r_{agg}	100 nm
Agglomerate porosity	ϵ_{agg}	0.17 [12]
Electrochemical constants		
CL Active surface area of Pt	A_v	2.00×10^5 cm^2 Pt/cm^3 CL [67]
Ionomer transport constants		
Bulk Oxygen diffusion coef.	$D_{O_2,N}$	9.726×10^{-6} cm^2/s, [83]
Bulk proton diffusion coef.	$D_{H^+,W}$	9.2×10^{-5} cm^2/s, [12]
Henry's constant O_2	$H_{O_2,N}$	3.1664×10^{10} Pa cm^3/mol, [29]
Henry's constant H_2	$H_{O_2,N}$	6.69×10^{10} Pa cm^3/mol
Relative permittivity	ϵ_r	20.0
Density	ρ	2.0 g/cm^3
Equivalent weight	EW	1100.0 $mol\ SO_3^-/g_{dry}$
Water transport constants [5]		
Bulk oxygen diffusion coef.	$D_{O_2,W}$	9.19×10^{-5} cm^{2}s
Bulk proton diffusion coef.	$D_{H^+,W}$	9.2×10^{-5} cm^{2}s
Relative permittivity	ϵ_r	60.0
Global constants		
Universal constant	R	8.314 J/mol K
Faraday's constant	F	96485 C/mol
Permittivity of free space	ε_0	8.854×10^{-14} C^2/J cm
Boltzmann constant	K	$8.617332478 \times 10^{-5}$ eV/K

Table 3.4 – Layer and micro structural properties resulting from micro structural assumptions and other properties described in Tables 3.2, and 3.3.

Description	Variable	Model	Value
Agglomerate film thickness	δ_{film}	Water Filled	11.6628 nm
		Ionomer Filled	6.91945 nm
Catalyst Layer Porosity	ε_v	Water Filled	0.338656
		Ionomer Filled	0.419408

Table 3.5 – Local operating conditions

	Low Current Density	High Current Density
ϕ_s	0.77 V	0.3 V
ϕ_m	-0.005 V	-0.2 V
x_{O_2}	0.15 V	0.15 V

3.3 Ionomer Filled Agglomerate

In this section geometric features, mass transport phenomena, and electrochemical phenomena, described using the improved ionomer filled agglomerate model are assessed for there significance to PEFC performance, and their potential in explaining PEFC mass transport limited behaviour. In this section analysis is performed for a full MEA, with key focus on the cathode catalyst layer. The anode catalyst layer is studied in greater detail in Section 3.5.

3.3.1 Kinetics

The Tafel and double trap kinetics models, as described in Section 2.3, are evaluated to determine reaction rates, using the parameters described in Table 2.2. Local operating condition as described in Table 3.5 were chosen based upon maximum and minimum overpotentials observed in CCL. Values for current per unit of platinum catalyst surface are shown in Figure 3.1. It can be seen that the Tafel model is more sensitive to overpotential as compared to the double trap model, and predicts significantly higher reaction rates.

The high sensitivity of the Tafel kinetics model to overpotential is due to the standard value of the cathodic transfer coefficient α_c being equal to 1.0. Parthasarathy et al. [74, 75] reported a value of 0.5 at high current densities, an apparent doubling of Tafel slope. It is hypothesized that the doubling of the Tafel slope occurs due to a change of significant reaction path way - see Section 2.3. The operating conditions and rate at which α_c changes from 1.0 to 0.5 is difficult to implement using the Tafel kinetics equation. The double trap kinetics is favourable in this regard, since it naturally exhibits a doubling of Tafel slope [7].

Simulations of individual numerical ionomer filled agglomerates for base case parameters as described in Tables 3.3 and 3.4 were performed using both the Tafel and double trap kinetics models, at operating conditions described in Table 3.5. Figure 3.2 shows reaction rate profiles within ionomer filled agglomerate cores. At high overpotentials, high reaction rates for the Tafel kinetics case, as shown in Figure 3.3(b)

leads to severe reactant starvation within the ionomer agglomerate core as seen in Figure 3.3.

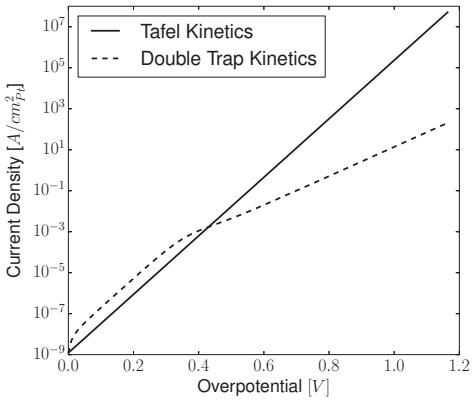

Figure 3.1 – Current density per unit area of platinum calculated using double trap and Tafel kinetics models for typical range of overpotential observed in CCL. Note how the Tafel model is more sensitive to over potential. $c_{H^+} = 0.001818$ mol/cm^3 , $c_{O_2} = 4.8 \times 10^{-7}$ mol/cm^3

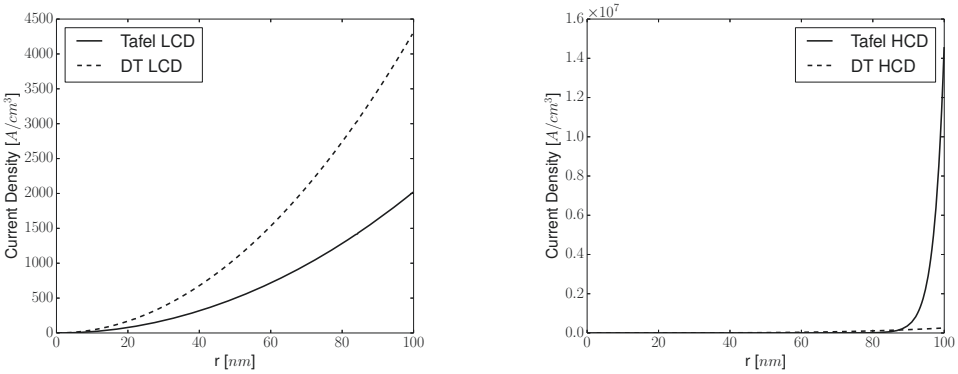

(a) Low Current Density

(b) High Current Density

Figure 3.2 – Current density profiles across ionomer filled agglomerate cores using double trap and Tafel kinetics models.

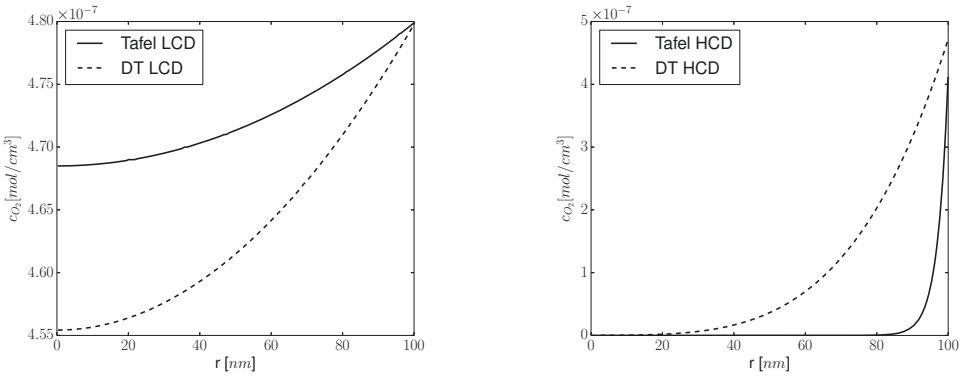

(a) Low Current Density (b) High Current Density

Figure 3.3 – Oxygen concentration profiles across ionomer filled agglomerate cores using double trap and Tafel kinetics models.

Figure 3.4 shows that the use of double trap kinetics model leads to lower reaction rates at high overpotentials as compared to the Tafel kinetics case. Agglomerate effectiveness, equation (2.86), describes how effectively catalyst surface area is utilized considering mass transport limitations. Figure 3.4 shows that the Tafel kinetics case exhibits relatively low effectiveness as compared to the double trap kinetics case.

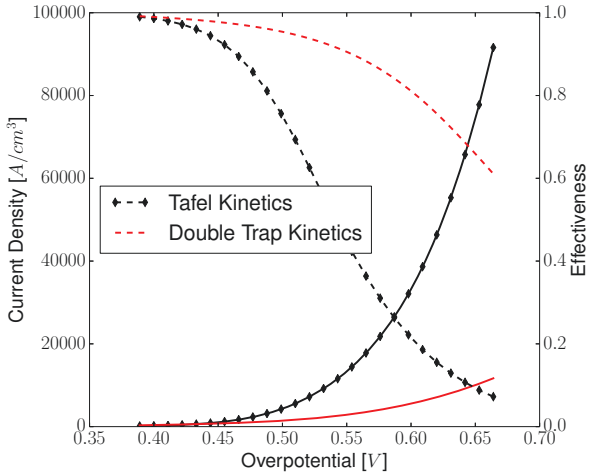

Figure 3.4 – Parametric study of individual ionomer filled agglomerates using double trap and Tafel kinetics. Solid lines correspond to current density, dashed lines correspond to agglomerate effectiveness.

The poor effectiveness observed for the Tafel case in Figure 3.4 is due to the rapidity of the reaction rates predicted by the Tafel kinetics model, leading to reactant starvation in the core as seen in Figure 3.3. The more subtle rate of reaction as predicted by the double trap kinetics model permits oxygen to diffuse within the agglomerate core more easily at high current densities, as seen in Figure 3.3, allowing reaction to occur at inner platinum sites, increasing agglomerate effectiveness.

MEA simulations were performed using a MEA model with multi-scale cathode catalyst layer and embedded ionomer filled agglomerates. Simulations were performed using both the Tafel and double trap kinetics models for comparison purposes. Figure 3.5 shows polarization curves for the simulated cases, and experimental data for comparison. It can be seen that the double trap kinetic case produces less current as compared to the Tafel kinetics case, and produces simulation results more similar to experimentally observed. Since the presented MEA model does not account for the formation of liquid water, the value of RH in the solution may exceed 100 %. Simulation results after this point should be heeded with caution, since the inclusion of liquid water would impose significant gaseous transport losses. However due to choice of parameters in this work (temperature and relative humidity of input gas), over saturation only occurs at very large current densities.

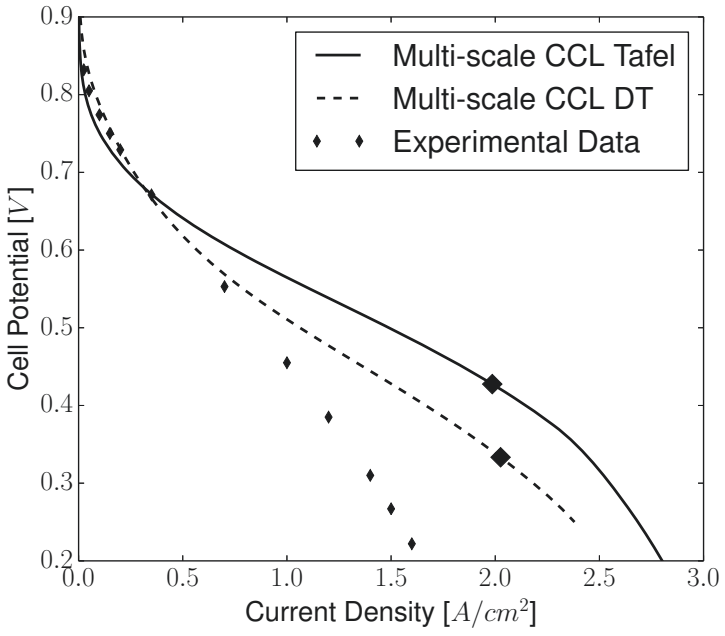

Figure 3.5 – Polarization curve for PEFC using ionomer filled agglomerates using double trap and Tafel kinetics. Diamond markers signify point at which MEA simulation exceeds 100% RH.

The presented micro-scale results seen in Figure 3.4 show a large difference in predicted current density, greater than a factor of 8, when comparing the Tafel kinetics and double trap kinetics cases. However, when considered in a multi-scale simulation, as seen in Figure 3.5, the effect of kinetic model choice is more subtle. The parametric study of agglomerates as shown in Figure 3.4 considers agglomerates operating at identical oxygen concentration, not truly accounting for the local variations in oxygen concentration that occur throughout the MEA domain as shown in Figure 3.6.

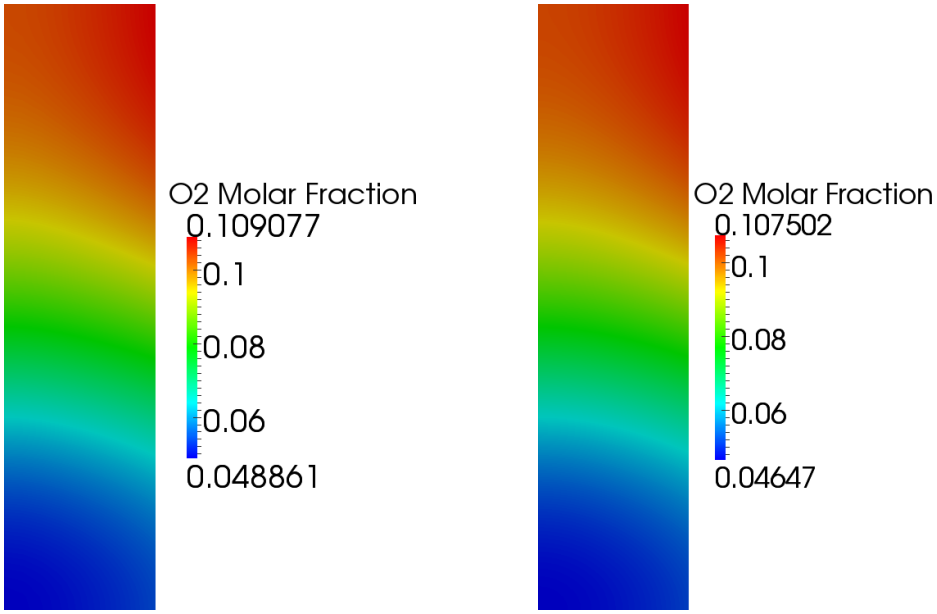

(a) Tafel Kinetics (b) Double trap kinetics

Figure 3.6 – Oxygen concentration profiles across CCL at 1.5 A/cm^3 cell current density with different kinetics models.

Figure 3.7 shows reaction rate contours across the CCL at 1.5 A/cm^3 cell operating potential. It can be seen that for the Tafel kinetics case reaction rates are more intensely concentrated at the left hand side of the cell, as compared with the Double trap Kinetics case. Additionally it can be seen in Figure 3.8 that the double trap kinetic case predicts more effective catalyst utilization. This result is consequential for CCL design: a common optimization strategy for the reduction of expensive platinum catalyst is to improve agglomerate effectiveness, but when the CCL is considered using the Double trap kinetics model the potential for improvements in effective catalyst utilization are diminished.

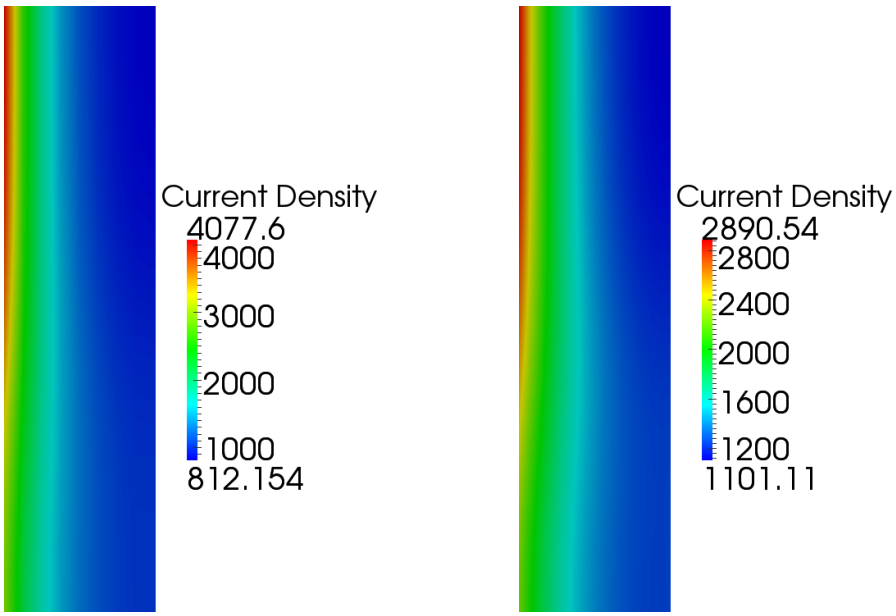

(a) Tafel Kinetics (b) Double trap kinetics

Figure 3.7 – Current density profiles across CCL at 1.5 A/cm^3 cell current density with different kinetics models.

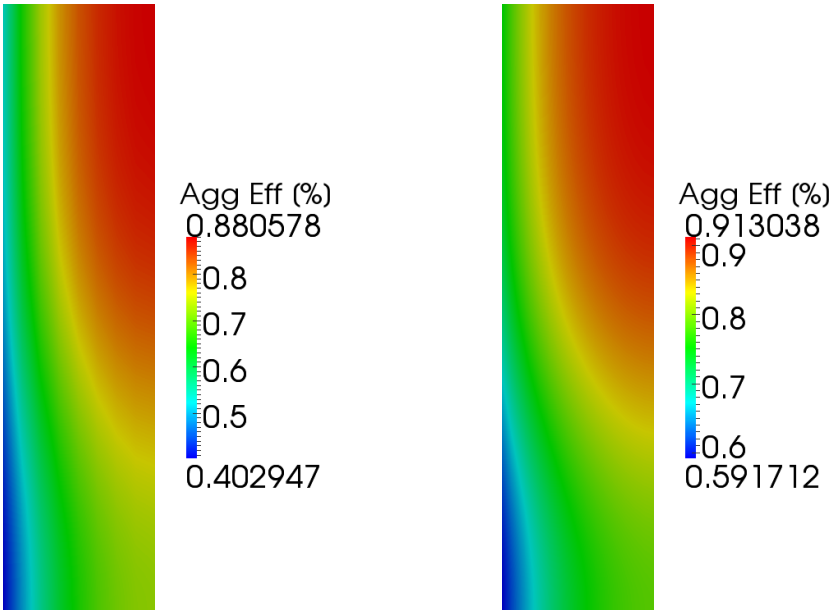

(a) Tafel Kinetics (b) Double trap kinetics

Figure 3.8 – Agglomerate effectiveness profiles across CCL at 1.5 A/cm^3 cell current density with different kinetics models.

The significance of multi-scale catalyst layer model with embedded agglomerate model for both kinetic cases is quantified. Identical MEA simulations were performed using a macro homogeneous CCL model instead of the multi-scale layer model. Polarization curves are compared in Figure 3.9. It can be seen that for the Tafel and double trap kinetic cases, the multi-scale catalyst layer model predicts lower reaction rates, due to the inclusion of agglomerate mass transport limitations. The multi-scale CCL cases, with agglomerate radius $r_{agg} = 100$ nm, differs significantly ($\geq 5\%$) from the macro homogeneous CCL case at 0.6 OCV and 0.48 OCV respectively - Figure 3.10. These difference occur within the ohmic region due to micro scale oxygen mass transport limitations, therefor the model highlights that oxygen transport mechanisms may be limiting not only in the mass transport region. It can be seen for lower agglomerate radii the significance of the multi scale model is diminished.

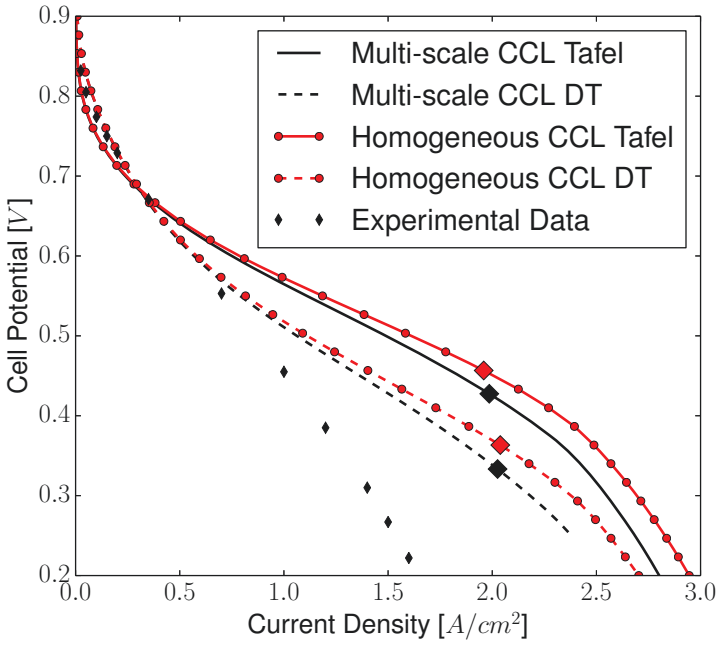

Figure 3.9 – Polarization curve for PEFC using ionomer filled agglomerates model, with homogeneous CL case for comparison. Diamond markers signify point at which MEA simulation exceeds 100% RH.

Figure 3.11 shows current density profiles across the CCL for the multi-scale and macro homogeneous cases using the double trap kinetic model at 1.5 A/cm^3 current density. It can be seen that due to the micro-scale mass transport limitations imposed by the agglomerate model, reaction rates are more evenly distributed across the layer for the multi-scale case, and a larger drop in cell potential is required to pro-

duce the same amount of current. To summarize, based on results presented in this section, the inclusion of micro-scale models will affect predicted cell reaction rates, resulting in lower predicted cell performance, and different distributions of reaction rate throughout the CCL. Additionally the double trap kinetics model predicts more realistic reaction rates as compared to the Tafel kinetics model, and therefore the double trap model [7, 54] is used to describe the ORR in proceeding sections.

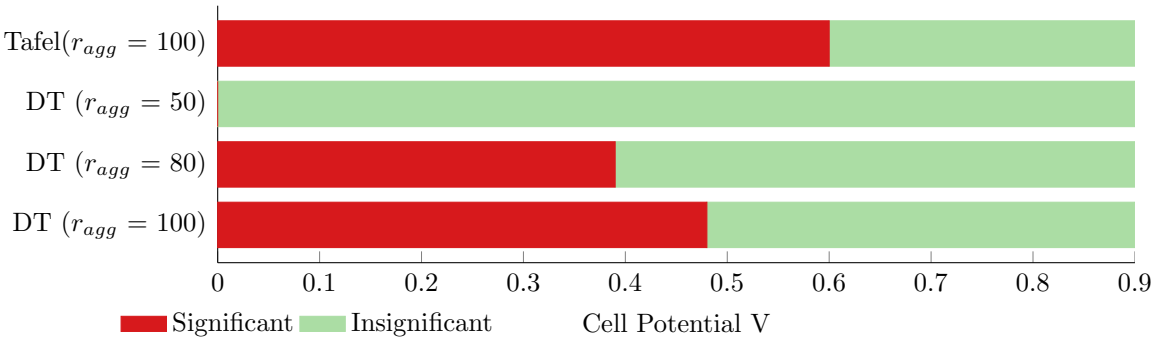

Figure 3.10 – Operating cell voltage ranges where multi-scale CCL case differs significantly (5%) from the homogeneous CCL case, for both kinetic cases.

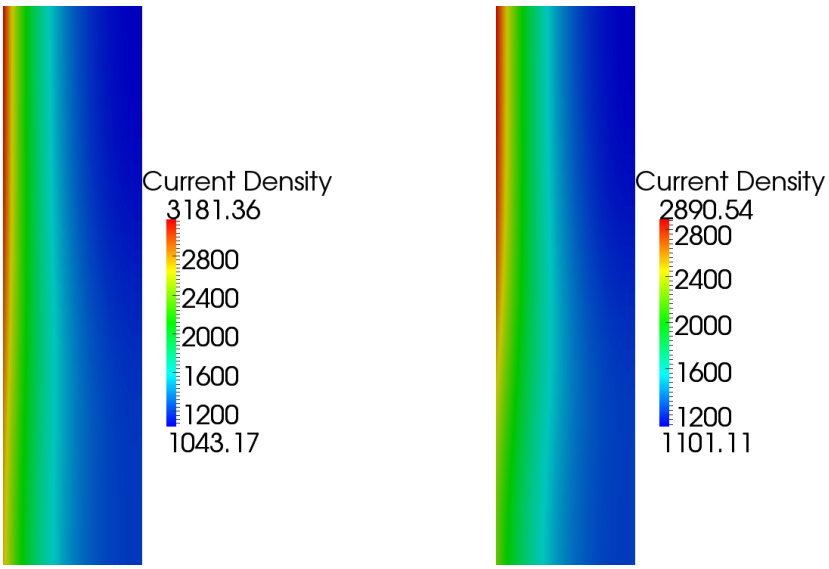

(a) Macro Homogeneous CL

(b) Multi Scale CL (ionomer filled agglomerates)

Figure 3.11 – Current density profiles across CCL at 1.5 A/cm^3 using the double trap kinetics model, and different CCL models.

3.3.2 Proton Conductivity

As mentioned in section 2.4, proton charge transport within the ionomer filled agglomerate domain is described using Ohm's law - equation (2.88). Typically, in analytical expressions for ionomer filled agglomerates, such as equation (2.85), proton charge transport is not modelled and it is assumed that protonic potential remains constant [24, 25, 29].

Values for proton conductivity in Nafion® taken from [60] are described for bulk Nafion, however Modestino et al. [84] showed that conductivity can be 100 times smaller in the case of thin films (in the range of 10 nm). Therefore in this work values of proton conductivity are scaled by several orders of magnitude in order to assess the sensitivity of the ionomer agglomerate to proton transport mechanisms and effective conductivity values.

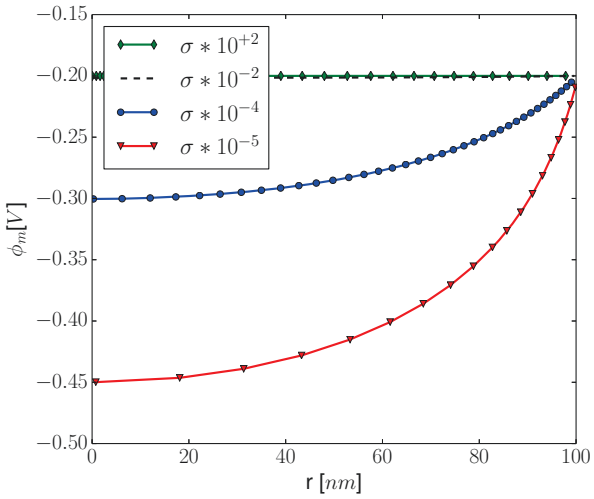

Figure 3.12 – Protonic potential across the agglomerate domain with varying proton conductivity.

Simulations of individual numerical ionomer filled agglomerates with parameters as described in Tables 3.2 and 3.3 and high current density surface conditions described in Table 3.5 were performed with varying proton conductivities, using double trap kinetics. Figure 3.12 shows that by decreasing σ_m (which appears in equation (2.88)) by a factor of 10^{-5}, significant effects on the electrolyte potential profile across the agglomerate core can be observed. The increase in protonic potential in the centre of the agglomerate is similar to results reported by Yoon and Weber [23]. Figure 3.13 shows that the change in the electrolyte potential across the agglomerate significantly affects the overpotential profile, in turn affecting the rate of the reaction, leading to lower agglomerate current and platinum utilization.

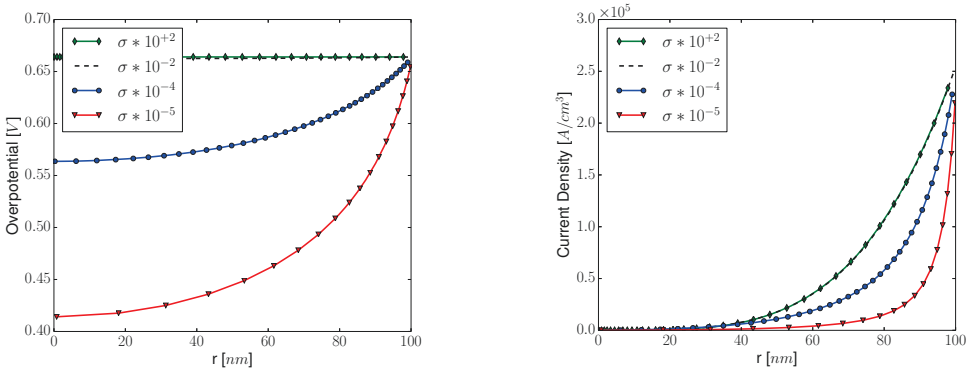

(a) Overpotential Profiles

(b) Current Density Profiles

Figure 3.13 – Agglomerate overpotential and current density across the agglomerate domain for varying proton conductivity.

Figure 3.14 shows results for a parametric study of ionomer filled agglomerates carried out for different proton conductivity values. It can be seen that when σ_m is decreased by 4 or more orders of magnitude, current density and agglomerate effectiveness are significantly impaired: at high overpotentials $\geq 0.65V$ the current produced by individual agglomerates is reduced by up to 33% as compared to standard case.

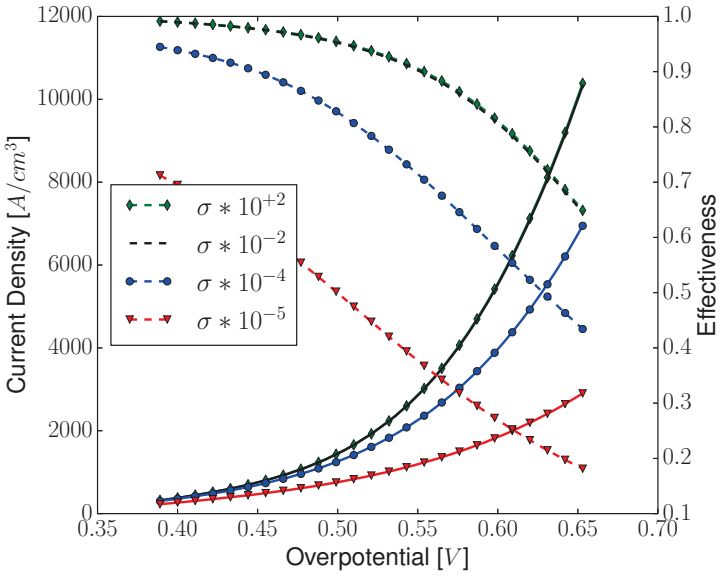

Figure 3.14 – Parametric study of individual ionomer filled agglomerates simulated for a range of σ_m.

To investigate the effect of micro-scale proton conductivity on PEFC performance MEA simulations were performed using the multi-scale catalyst layer, with embedded ionomer filled agglomerates. Figure 3.15 shows polarization curves for performed simulations. It can be seen that predicted performance of a PEFC is not significantly affected until values of σ_m are reduced by 4 orders of magnitude. At values of σ_m reduced by 10^{-4} a reduction of up to 9% in current density is observed. This reduction in current density is more subtle than previously observed for individual agglomerates. The result is similar to previously discussed result in Section 3.3.1: difference in micro scale performance are more subtle when considered in a multi-scale system. Additionally it can be seen that as current densities become large, $\geq$2.0 A/cm^3, polarization curves for cases 10^{-4} and 10^{-2} begin to converge, as oxygen transport become more limiting.

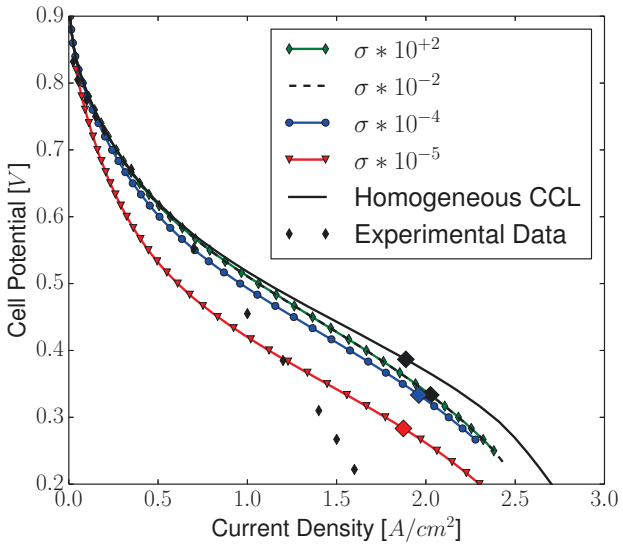

Figure 3.15 – Results demonstrating the effect of reducing the proton conductivity within the agglomerate. Note that the curves remain practically identical for a wide range of σ_m. Diamond markers signify point at which MEA simulation exceeds 100% RH.

In summary the value of proton conductivity does not have a significant effect on PEFC performance until it is reduced by four orders of magnitude, therefore the assumption of iso protonic potential in micro-scale models appears reasonable. Figure 3.16 shows the range of operating potentials for which the presented micro scale conductivity cases differ significantly from the homogeneous CCL case.

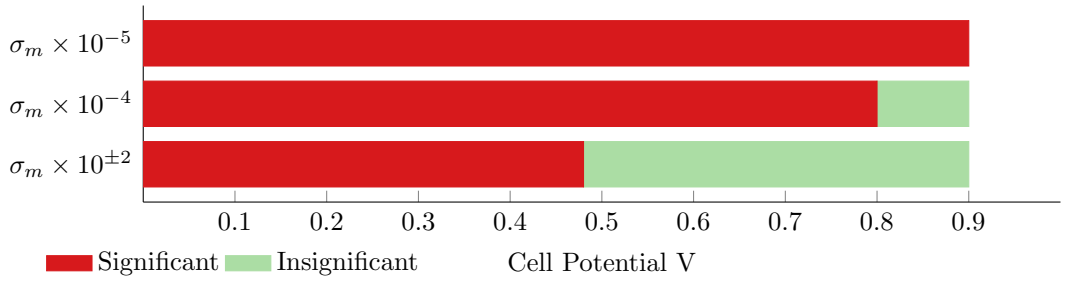

Figure 3.16 – Operating cell voltage ranges were multi-scale CCL case differs significantly (5%) from the homogeneous CCL case.

3.3.3 Catalyst Grading

Banham et al. [77, 78] reported that platinum may reside on the surface or within the carbon support material as discrete particles, depending on choice of catalyst support material. To correctly represent catalyst distributions the ionomer and water filled agglomerate models were modified in Section 2.4.2.3. An improved description of catalyst distribution within the agglomerate core can help improve current density predictions for MEA mass transport limited operating conditions [27]. In this section the effects of non uniform catalyst distributions on agglomerate and MEA current density predictions are investigated.

3 different grading profiles were used in this work to investigate the effects of catalyst distribution:

1. **[1,0,0]:** all of the platinum catalyst is confined to the inner third of the agglomerate core, i.e. at $r \leq \frac{r_{core}}{3}$. In this case the outer two thirds of the agglomerate core will not contain active catalyst, and the reactants must diffuse into the inner third of the agglomerate radius in order to be reacted.

2. **[0,1,0]:** all of the platinum catalyst resides at $\frac{r_{core}}{3} < r \leq \frac{2r_{core}}{3}$. In this case the inner and outer third of the agglomerate core will not contain active catalyst and reactants must diffuse into the central third of the agglomerate radius in order to be reacted.

3. **[0,0,1]:** all of the platinum catalyst resides in the outer third of the agglomerate core, i.e at $\frac{2r_{core}}{3} < r \leq r_{core}$

Between these three cases, the best and worst catalyst distributions scenarios are represented: clearly case [0,0,1] will be the most effective since the catalyst is ideally located close to the agglomerate surface, minimizing mass transport requirements.

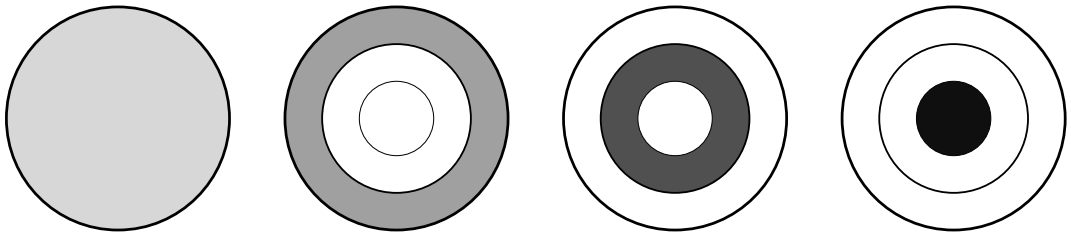

(a) Non-Graded (b) [0,0,1] (c) [0,1,0] (d) [1,0,0]

Figure 3.17 – Representation of graded cores studied in this work.

Case [1,0,0], where the catalyst is located deep within the agglomerate core structure, will incur larger mass transport losses since reactant must diffuse through the tortuous porous network to first reach the catalyst. The method described in Section 2.4.2.3 is used to determine the amount of platinum catalyst per unit volume for each case, conserving the amount of catalyst per agglomerate. Active area loading weights calculated using these methods are show in Table 3.6. Note the weights shown correspond to the inverse of the volume ratios of each core region.

Table 3.6 – Graded core active area $A_{v,\,i}$.

Grading \ **Domain**	0 nm - 33.33 nm	33.33 nm - 66.66 nm	66.66 nm- 100 nm
[1,0,0]	$27.8264 \cdot A_v$	0.0	0.0
[0,1,0]	0.0	$3.9752 \cdot A_v$	0.0
[0,0,1]	0.0	0.0	$1.4035 \cdot A_v$

Simulations of individual ionomer filled agglomerates using parameters as described in Section 3.2 and grading profiles as described in this Section were performed. Figure 3.18 shows current density profiles across the graded agglomerate cores. For low current densities operating conditions the highest intensity of current density is observed for the [1,0,0] case, since active area is highly concentrated within the central third of the core. At high current densities it can be observed that the cases [1,0,0] and [0,1,0] exhibit poorer reaction profiles as compared to case [0,0,1]. Figure 3.19 shows the reason for these poorer performances: the redistribution of catalyst imposes greater diffusion losses, as oxygen is required to diffuse further through the porous agglomerate core before reaching platinum catalyst reaction sites.

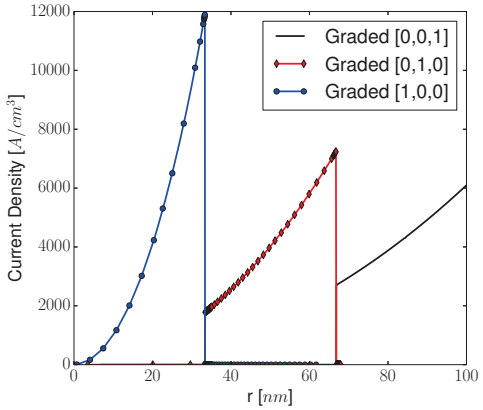

(a) Low Current Density OC

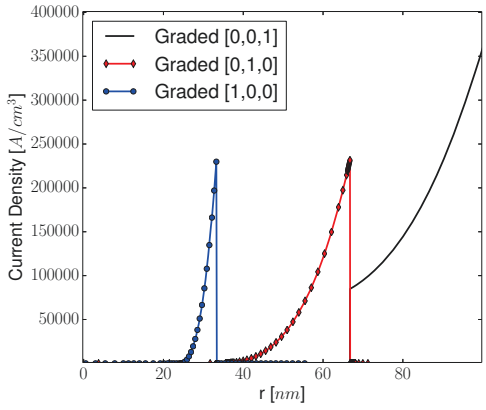

(b) High Current Density OC

Figure 3.18 – Current density profiles across graded agglomerate cores, as seen in Figure 3.17.

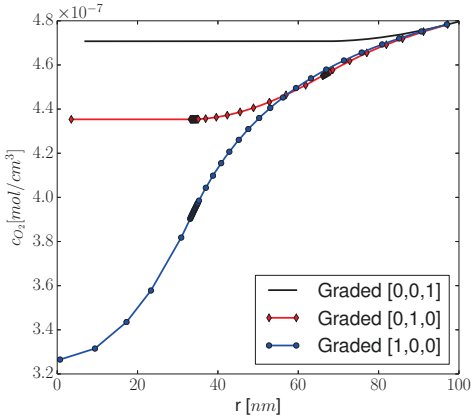

(a) Low Current Density OC

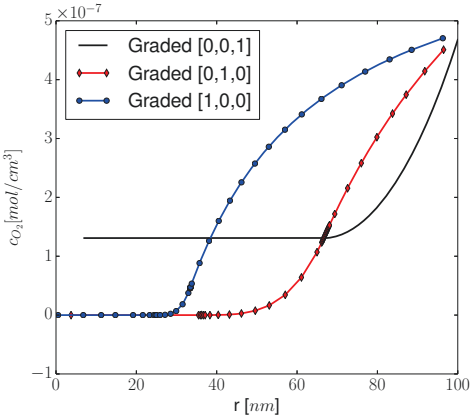

(b) High Current Density OC

Figure 3.19 – Oxygen concentration profiles across graded agglomerate cores, as seen in Figure 3.17.

A parametric study of the three ionomer filled agglomerates described above was performed for operating condition range described in Table 3.5. Results for said study are show in Figure 3.20. It can be seen that the grading cases [1,0,0] and [0,1,0] significantly decrease the current density prediction and effectiveness of the agglomerate models.

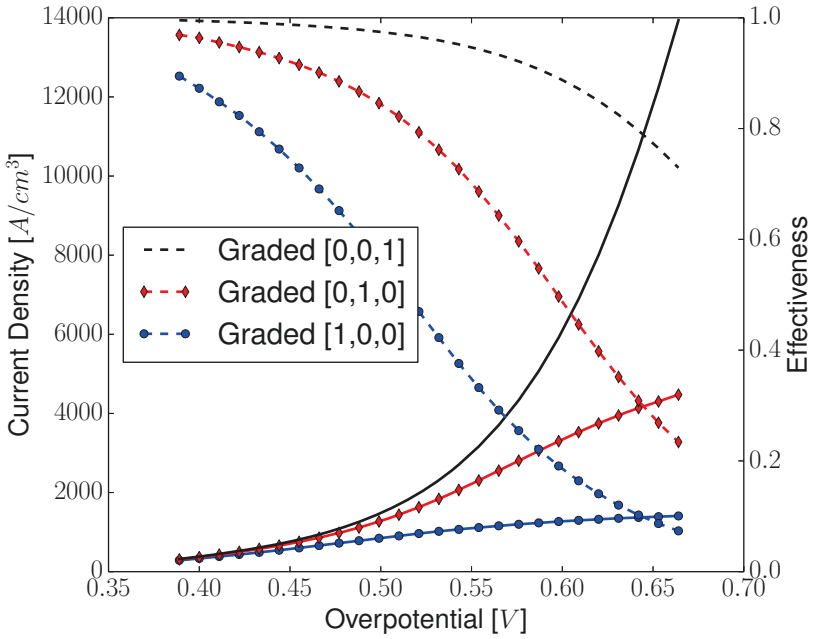

Figure 3.20 – Parametric study of individual ionomer and water filled agglomerates. Solid lines correspond to current density, dashed lines correspond to agglomerate effectiveness.

MEA simulatons were performed, using multi-scale catalyst layers, with embedded ionomer filled agglomerate, using loading profiles as described in Table 3.6. Figure 3.21 show polarization curves for performed MEA simulations. A significant reduction in current density is observed for two graded cases: for grading case [0,1,0] predicted MEA current density approaches that of experimental data, and for grading profile [1,0,0] agglomerate performance is so impaired that the model predicts poorer MEA performance than experimentally observed. Therefore when considered in a MEA simulations it can be concluded that micro-scale mass transport losses due to the distribution of active catalyst sites are extremely significant, and a potential further explanation for mass transport limited behaviour. Coupled with improved imaging techniques and micro structure characterization , the model presented in this work can be used to model PEFC CL with greater accuracy than before.

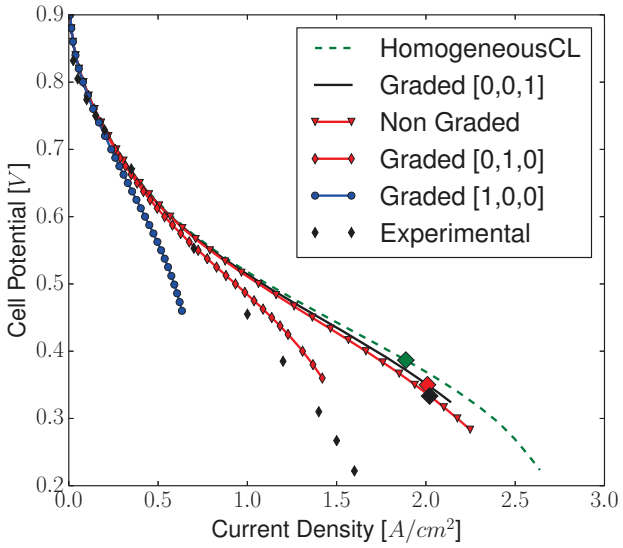

Figure 3.21 – Polarization curve for PEFC using graded ionomer filled agglomerates and double trap kinetics. Diamond markers signify point at which MEA simulation exceeds 100% RH.

The graded formulation and cases presented here represent extreme cases of micro structure, illustrating the impact catalyst distributions, and the need for these quantities to be more accurately represented. Figure 3.22 shows the range of operating potentials for which the 3 presented cases significantly differ from the homogeneous CCL case. Furthermore the [0,0,1] case shows improved performance over the non graded ionomer base case, highlighting that if micro structures can be engineered to position catalyst within micro structure close to the gas phase, then significant improvements in platinum utilization can be achieved.

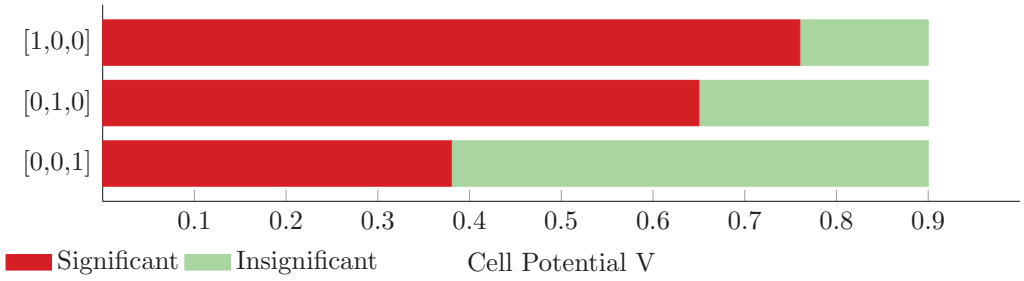

Figure 3.22 – Operating cell voltage ranges were multi-scale CCL case differs significantly (5%) from the homogeneous CCL case

3.3.4 Film Transport Losses

As described in Section 2.4 the ionomer and water filled agglomerate models include an ionomer thin film. The consequence of including the Nafion® thin film in the agglomerate model is additional mass transport losses, since oxygen must diffuse through the film in order to react in the catalyst loaded core. The mechanism by which oxygen dissolves from the gaseous phase into the thin film is typically described using Henry's law - equation (2.24). Suzuki et al. [48] however recently proposed a non equilibrium process for the dissolution of oxygen, which shall be investigated later in this section.

A simulation of an ionomer filled agglomerates with parameters as described in Tables 3.3 and 3.4 was performed at high current density operating conditions as describe in Table 3.5, using the Henry's law boundary condition, so that the mass transport limiting effect of the thin film could be appreciated. Figure 3.23 shows oxygen profiles across the ionomer core and thin film. It can be seen that even at high current operating conditions the thin film has relatively little effect on oxygen transport into the ionomer filled core, as O_2 concentration only drops by 2.3%.

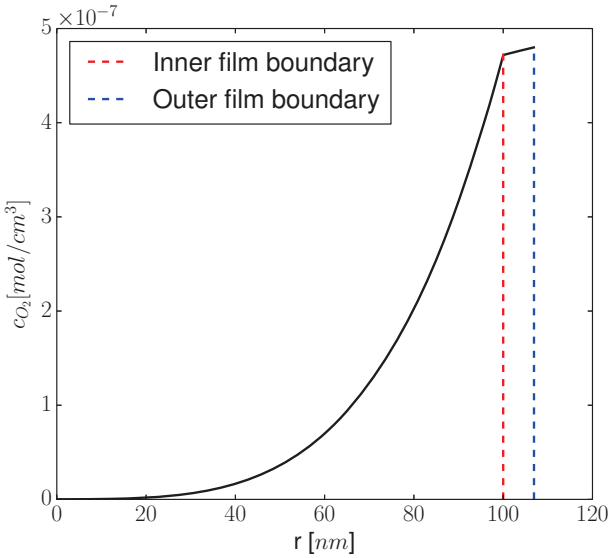

Figure 3.23 – Oxygen concentration profile across a individual ionomer filled agglomerate with ionomer thin film.

A parametric study was performed w.r.t. overpotential of the previously discussed ionomer filled agglomerate, with and without the inclusion of the ionomer thin film. It can be seen in Figure 3.24 that the addition of the ionomer thin film has minimal effects on the current density effectiveness of the ionomer filled agglomerate model. MEA simulations with and without the inclusion of the ionomer thin film were also performed. Figure 3.25 shows polarization curves for MEA simulations. It can be seen that the ionomer thin film has practically no effect on predicted PEFC performance, as simulation results match within 0.5%.

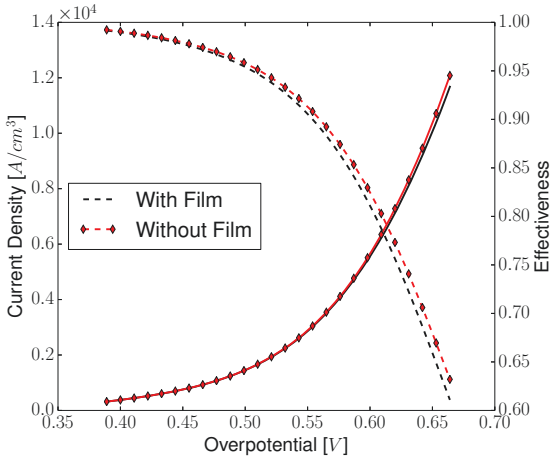

Figure 3.24 – Parametric study of individual ionomer filled agglomerates, with and without ionomer thin film.

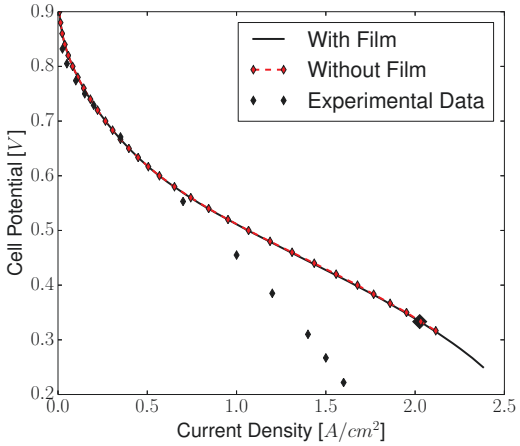

Figure 3.25 – Polarization curve for PEFC with and without ionomer thin film. Diamond markers signify point at which MEA simulation exceeds 100% RH.

Simulations were performed using the non-equilibrium agglomerate boundary con-

dition proposed by Suzuki et al. [48] described in Section 2.4.2.2. Firstly simulations of individual ionomer filled agglomerates with high current density operating conditions $\{\phi_m, \phi_s, x_{O_2}\}$ = {-0.2 V , 0.3 V, 0.15 } were performed for various values of the reaction rate constant k_{O_2} . A reaction rate coefficient based on the work by Suzuki et al. [48] was calculated as $k_{O_2} = 0.13$. Figure 3.26 shows oxygen profiles across individual agglomerates, and corresponding reaction rate profiles. It can be seen that for $k_{O_2} = 0.13$ oxygen transport predicted by the non-equilibrium boundary condition is as effective as described by Henry's law (surface c_{O_2} match within 2%), hence the non-equilibrium boundary condition provides no significant effect over the traditional assumption of an equilibrium dissolution process.

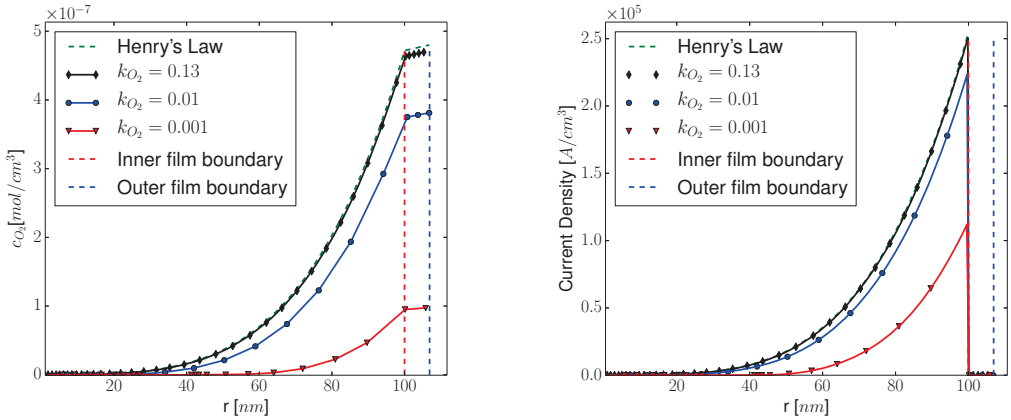

(a) Oxygen concentration profiles

(b) Current density profiles

Figure 3.26 – Oxygen concentration and current density profiles across agglomerate cores for different values of oxygen dissolution reaction coefficient.

The value, $k_{O_2} = 0.13$ m/s, from Suzuki et al. [48] is experimentally determined using ionomer films of approximately 200 nm and larger. To find coefficient values for films of the order of 10 nm extrapolation is required. Consequently, there is much uncertainty in k_{O_2}'s value. Further experiments are required in order to fully characterize the ionomer thin films. Theoretically however, the order of magnitude of significant reaction coefficients can be determined, and the effect of the non-equilibrium boundary condition for these values can be explored.

Figure 3.26 shows simulation results for individual agglomerates with values $k_{O_2} =$ 0.01 and 0.001 m/s. It can be seen that the reduced reaction coefficients k_{O_2} cause the non-equilibrium boundary condition to impose significant mass transport limiting effects. For lower values of k_{O_2}, poorer oxygen profiles across the ionomer film can be observed, resulting in poorer rate of reaction.

A parametric study of ionomer filled agglomerates w.r.t. overpotential with non-equilibrium boundary condition values was performed. Results for agglomerate current density and effectiveness can be seen in Figure 3.27. For $k_{O_2} = 0.001$ m/s significant rate limiting behaviour is observed: at overpotential values from 0.55 V to 0.6 V an inflection in the current density:overpotential curve is observed. The cause is as follows: as reaction rates increase, and hence oxygen flux through the ionomer|gas interface increase, the non-equilibrium dissolution process becomes more sluggish, retarding reaction rates.

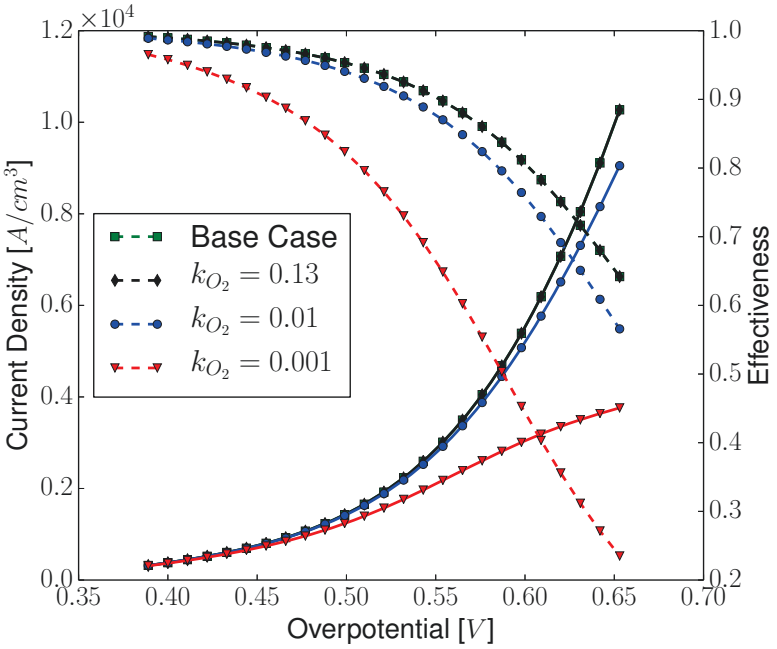

Figure 3.27 – Parametric study of individual ionomer filled agglomerates with non-equilibrium oxygen boundary condition, for varying k_{O_2}. Henry's law was used as the agglomerate oxygen boundary condition for "Base case" scenario. Note that base case and $k_{O_2} = 0.13$ case are identical.

MEA simulations with a multi-scale CCL including ionomer filled agglomerates using the non equilibrium boundary condition for varying k_{O_2} were performed. Figure 3.28 shows polarization curves for performed MEA simulations. When considered in a multi-scale MEA simulation the non-equilibrium boundary conditions become noticeably significant at $k_{O_2} = 0.01$ m/s, and at $k_{O_2} = 0.001$ m/s micro-scale mass transport limitations at the ionomer|gas interface results in a large decrease in MEA performance, producing results similar to experimentally observed.

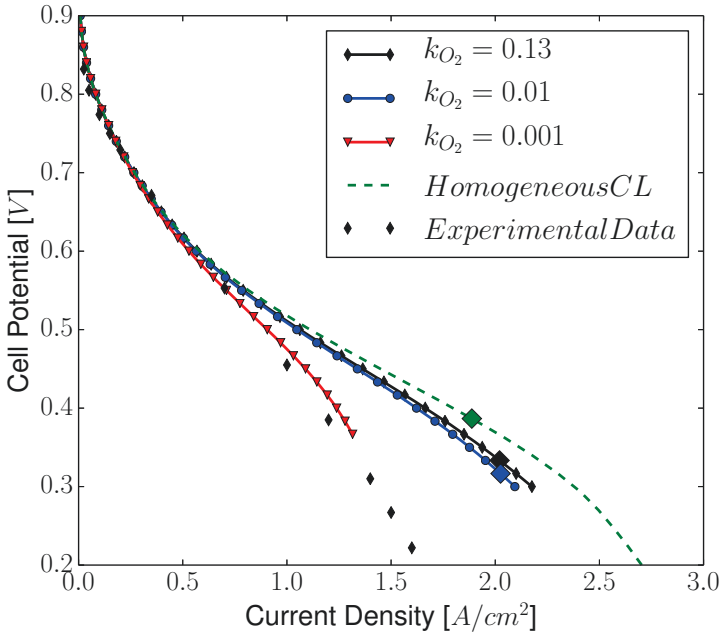

Figure 3.28 – Non equilibrium boundary condition polarization curves.

In conclusion the non-equilibrium dissolution process described by Suzuki et al. [48] was found to be significant for $k_{O_2} \leq 0.01$ m/s. There is still much experimental uncertainty at this time regarding the value of reaction coefficient k_{O_2}. Further experimental work combined with the presented multi-scale MEA model can be used to definitively answer the question regarding the significance of this transport phenomenon. Significance of the multi-scale CCL with varying agglomerate boundary conditions versus the homogeneous CCL is summarized in Figure 3.29.

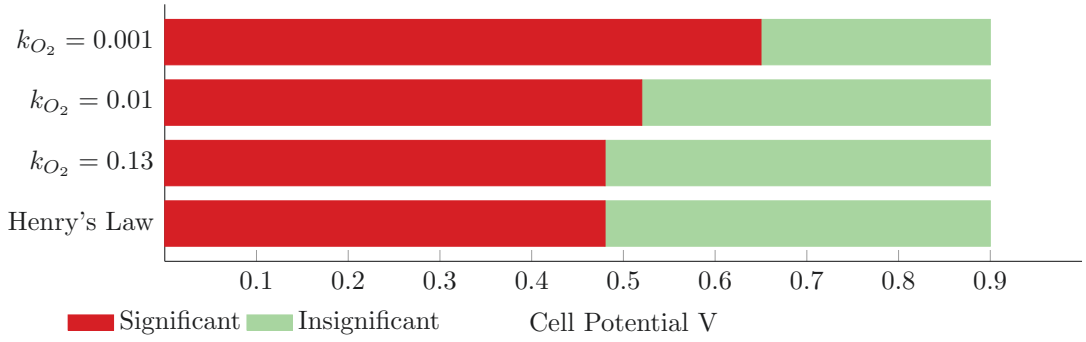

Figure 3.29 – Operating cell voltage ranges were multi-scale CCL case differs significantly (5%) from the homogeneous CCL case

3.3.5 Agglomerate Size Polydispersion

A wide range of experimentally measured particle sizes have been reported to date [5]. Epting et al. [46] reported a polydisperse size distribution of agglomerates exists within the CL. A typical simplifying assumption in PEFC multi-scale modelling is to use a single representary particle size. Epting and Litster [1] state that the assumption of a agglomerate single agglomerate size is an invalid modelling assumption as it leads to large errors in current prediction.

Table 3.7 – Agglomerate size distributions taken from Epting and Litster [1].

Agglomerate Radius, nm	Agglomerate Film, nm	Volume fraction, %
23	1.67	11.50
40	2.77	14.80
56	3.9	11.20
72	5.03	16.20
88	6.15	14.00
105	7.27	12.20
121	8.40	11.20
137	9.53	5.60
154	10.6	2.10
170	11.78	1.20

Epting et al. [46] determined agglomerate size distributions using nano-CT reconstructions of PEFC catalyst layers. Agglomerate size distributions and corresponding volume fractions are shown in Table 3.7 based on data reported by Epting and Litster [1]. To determine the volumetric current density of a catalyst layer slice Epting and Litster [1] considered the contributions of each individual agglomerate size as described in Table 3.7. Epting and Litster report significant disagreement in reaction rates predicted by simulations where a polydisperse agglomerate size distribution is not considered.

Simulations of an agglomerate polydispersion using developed polydisperse framework explained in Section 2.4.5 were performed using the agglomerate distribution described in Table 3.7. Analysis is performed using the Tafel and double trap kinetics models, and parameters as described in Tables 3.5 – 3.2. It should be noted that the measured agglomerate radii in Table 3.7 include ionomer thin film, as they were determined using nano-CT techniques in which the ionomer phase cannot be distinguished from the platinum loaded carbon phase. However in this work these dimensions are considered as the dimension of the agglomerate core. Film thicknesses are calculated using equation (2.77).

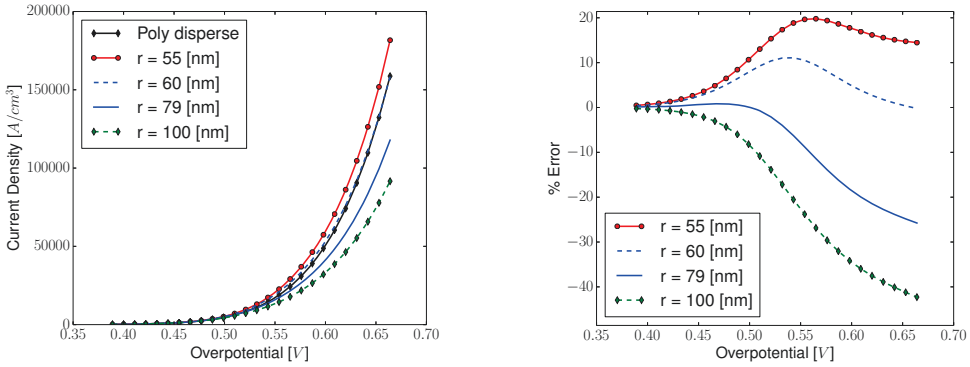

(a) Current Density (b) % Error

Figure 3.30 – Current density predictions of poly and mono dispersions performed using Tafel kinetics, and associated errors.

Figure 3.30 shows simulation results for performed parametric study of poly and mono dispersed agglomerates using Tafel kinetics. It can be seen that at moderate to high overpotentials large errors in current prediction exist between the polydisperse and mono disperse cases. A mean agglomerate radius based on volume fractions in Table 3.7 was calculated as 79 nm. Typically such a mean radius would be used to describe all agglomerates in the CL, however it can clearly be seen from Figure 3.30 that when considering agglomerates individually the assumption of a single agglomerate size can lead to large errors. Calculated % error profiles as seen in Figure 3.30 are similar compared to values reported by Epting and Litster [1].

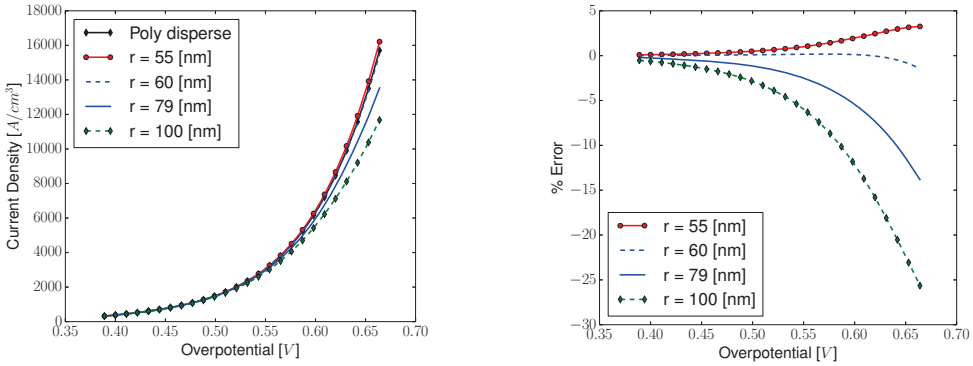

(a) Current Density (b) % Error

Figure 3.31 – Current density predictions of poly and mono dispersions performed using double trap kinetics, and associated errors.

Simulation results for performed parametric study of poly and mono dispersed agglomerate models using the double trap kinetic are shown in Figure 3.31. Similar to the Tafel kinetics case Figure 3.31 shows that large errors in predicted current density occur due to the assumption of a mono agglomerate size dispersion, however compared to the Tafel kinetics case, % errors for the double trap kinetics case are more subtle.

MEA simulations were performed using a multi-scale cathode catalyst layer with embedded ionomer filled agglomerates, using the Tafel and double trap kinetics model. At each quadrature point agglomerates as described in Table 3.7 are evaluated and their contributions summed based on their relative volume fraction - equation (2.121). Simulations were performed using parameters as described in Tables 3.2 and 3.3. Simulations for mono agglomerate distributions where also performed for comparison purposes. Figures 3.32 and 3.33 show polarization curves for performed simulations and corresponding % error. It can be seen that for both kinetic cases the % errors for mono disperse cases are insignificant, contrary to results seen previously for individual agglomerates.

When considered for individual agglomerates, as done in reference[1], correct representation of agglomerate size distribution is significant. However as show in Figure 3.33 when considered in a MEA multi-scale system, the difference in predicted reaction rates between polydisperse and mono disperse systems are insignificant.

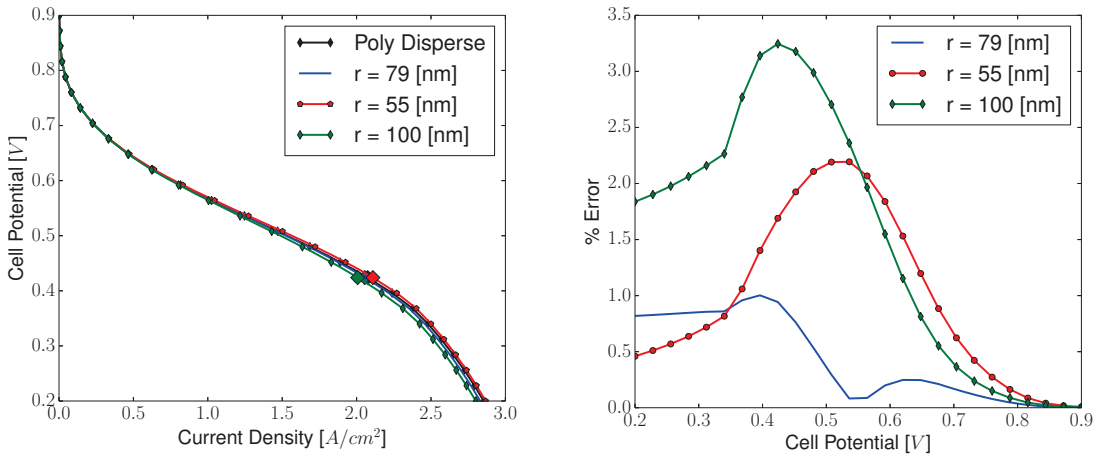

(a) Polarization curve

(b) % Error

Figure 3.32 – Polarization curves for MEA simulations performed using poly dispersion and mono dispersion, using Tafel kinetics. Associated errors of mono disperse assumption versus poly disperse are shown on right.

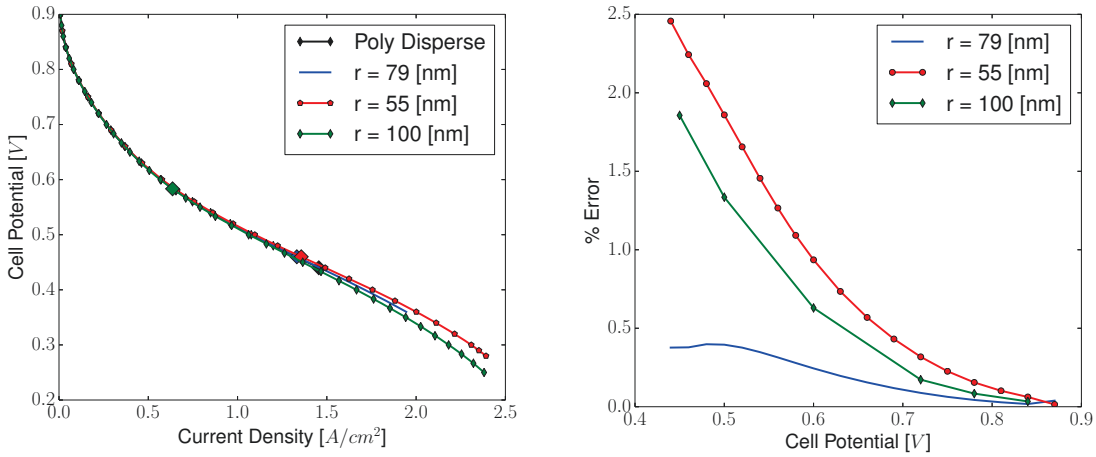

(a) Polarization curve

(b) % Error - **To be improved**

Figure 3.33 – Polarization curves for MEA simulations performed using poly dispersion and mono dispersion, using double trap kinetics. Associated errors of mono disperse assumption versus poly disperse are shown on right.

Results from previous sections highlight that the MEA model with multi-scale CCL can be insensitive to small/moderate changes in micro-scale performance. For the presented agglomerate distribution in Table 3.7, the weighted mean value and standard deviation of agglomerate dimensions are 79.9 nm and 40.1 nm respectively. It can be seen that the MEA model is relatively insensitive to agglomerate sizes within this standard deviation: polarization curves for double trap kinetics case as seen in Figure 3.32 with r equal to 55 nm and 100 nm differ at most by 5.25 %. Similarly reaction contour plots across the CCL for double trap kinetics case are seen to be quite alike for different agglomerate radii, as seen in Figure 3.34.

In summary the effect of agglomerate size polydispersion was investigated for the first time, thanks to multi-scale framework implemented as part of this work, in a multi-scale MEA simulation. It was found that agglomerate size polydispersion is not a significant as previously thought [1], and small errors in current prediction occur due to the assumption of a mono disperse agglomerate size distribution.

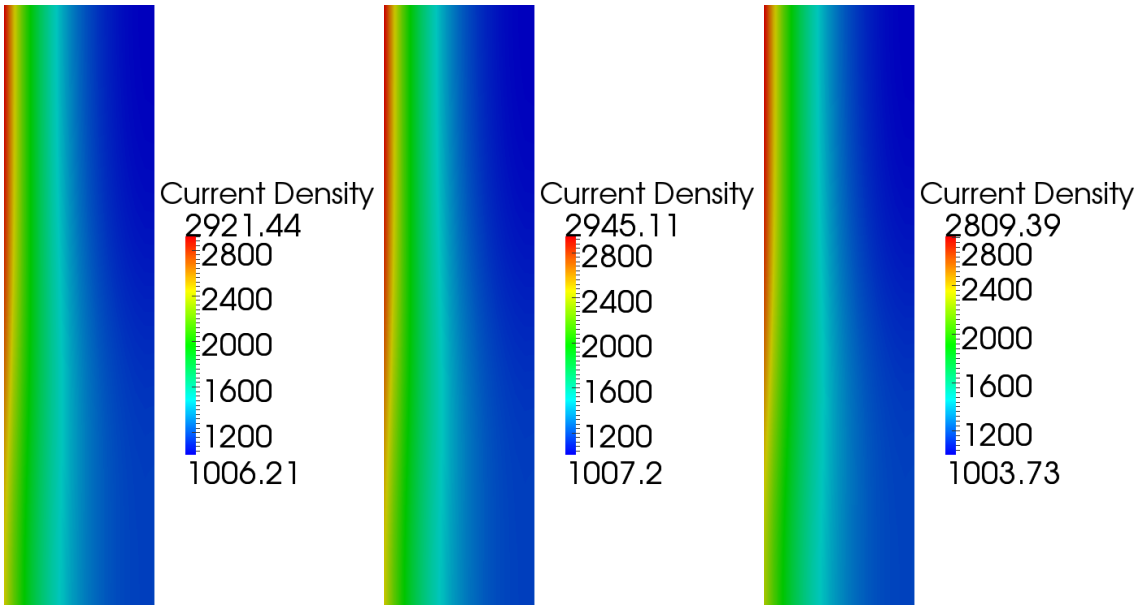

(a) Poly Disperse (b) r = 55 nm (c) r = 79 nm

Figure 3.34 – Current density contour plots for polydisperse and monodisperse cases, using double trap kinetics, at 1.5 A/cm^3.

3.4 Water Filled Agglomerate

3.4.1 Comparison with Ionomer Filled Agglomerate

Previous multi-scale comparisons between the water and ionomer filled agglomerate models by Dobson [5] were limited due to model convergence issues. Several improvements implemented as part of this work, such as the initial solution framework developed for numerical micro-scale models (Sections 3.7 and Appendix A:), allow for comparison of the water and ionomer filled agglomerate models over a wider range of operating conditions than previously possible. Furthermore, in order to compare the models using the double trap kinetics model instead of the Tafel model, as done by Dobson [5], the double trap model was reformulated to include sensitivity to protons in Section 3.3.1. Therefore in the following sections a comparison between the two assumptions is performed, in order to better appreciate electrochemical behaviour of the two models due to their differing mass transport descriptions.

3.4.1.1 Comparison Using Tafel Kinetics

Simulations of individual water and ionomer filled agglomerates were performed at high current density (HCD) and low current density (LCD) operating conditions

shown in Table 3.5 using the Tafel kinetics model, and fuel cell parameters shown in Tables 3.2 and 3.4.

Figure 3.35 shows oxygen concentrations across the water and ionomer filled cores. Improved oxygen profiles are observed for the water filled case, due to the higher diffusivity of oxygen in water than in Nafion® ($D_{O_2,W} > D_{O_2,Nafion}$). Note the lower concentration of oxygen at the exterior of water filled agglomerate core. This is due to the thicker ionomer film for the water filled case - see Table 3.4. In Section 3.3.4 it was shown that the drop in oxygen concentration across the ionomer thin film was negligible when considered using the double trap kinetics model. The high current density reaction rate predicted by the water filled agglomerate model using Tafel kinetics versus the ionomer filled agglomerate model using Double trap kinetics discussed in Section 3.3.4 is over 13 times greater. At these high reaction rates the concentration drop in oxygen across the thin film becomes significant. However the large reaction rates predicted using the Tafel kinetics model are unrealistic at HCD operating conditions, due to the oxygen reaction order γ_{O_2} being equal to 1. This illustrates how the choice of kinetics model may emphasize different aspects of the agglomerate model.

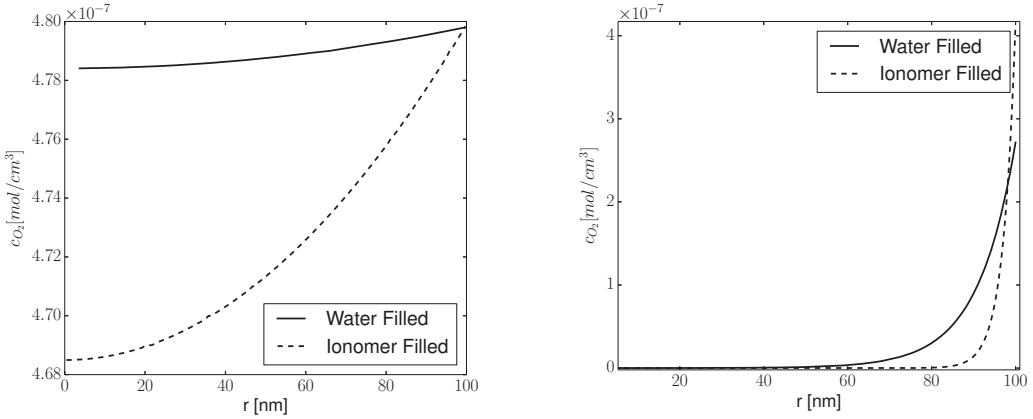

(a) Low Current Density

(b) High Current Density

Figure 3.35 – Oxygen concentration profiles across agglomerate cores.

The fundamental difference between the water and ionomer filled models is that the cores are filled with different electrolyte material. The electrochemical transport implications of this difference results in differing proton transport mechanism for either model. For the ionomer filled assumption proton concentration is assumed constant due to the presence of sulphonic groups in Nafion, and the potential of the electrolyte is described using Ohm's law. In the water filled agglomerate however,

proton concentration varies. Proton transport is described using the Nernst-Plank equation, and electrolyte potential is described using Poisson's equation.

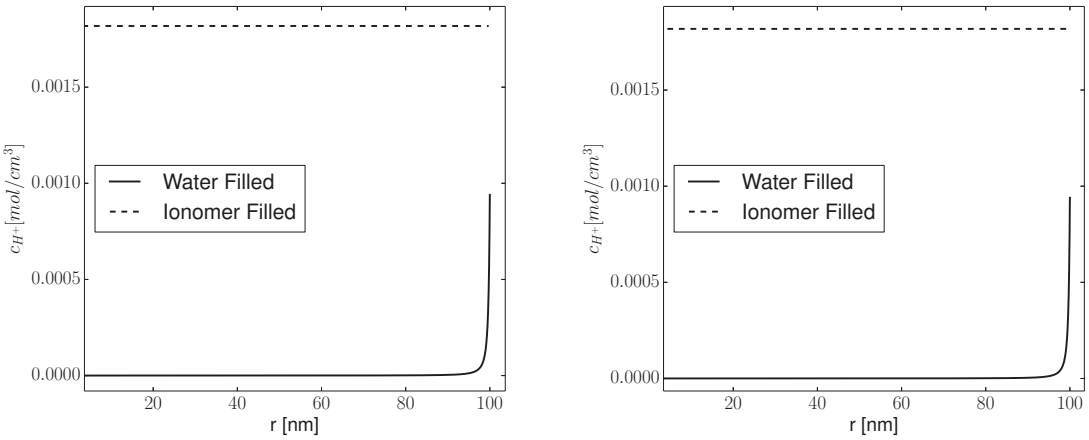

(a) Low Current Density

(b) High Current Density

Figure 3.36 – Proton concentration profiles across agglomerate cores.

Figure 3.36 shows proton concentration across the water and ionomer filled cores. It can be seen that for the water filled case effective proton transport is very poor, resulting in low concentration of protons within the water filled core. Figure 3.37 shows overpotentials across the ionomer and water filled cores. Similar to previous Sections 3.3.2, it is seen that overpotential remains constant throughout the ionomer filled core, due to highly effective proton charge transport in Nafion® . For the water filled case however, larger overpotentials are observed, due to the difference in electrolyte and charge transport mechanisms.

The combination of different oxygen concentration, proton concentration, and overpotential profiles across the water and ionomer filled cores result in different reaction rate profiles for both models. Figure 3.38 shows reaction rate profiles across the agglomerate cores. One would expect, that due to low proton concentrations observed for the water filled case, reactions rates would be smaller in comparison to the ionomer filled case. However as seen in Figure 3.38 this is not the case. Reaction rate diminishment due to low proton concentration is counterbalanced by higher over potentials and higher oxygen concentration within the water filled core. Note that this counterbalance due in part to Tafel kinetics's high sensitivity to overpotential due to the standard value of γ_c equal to 1.0.

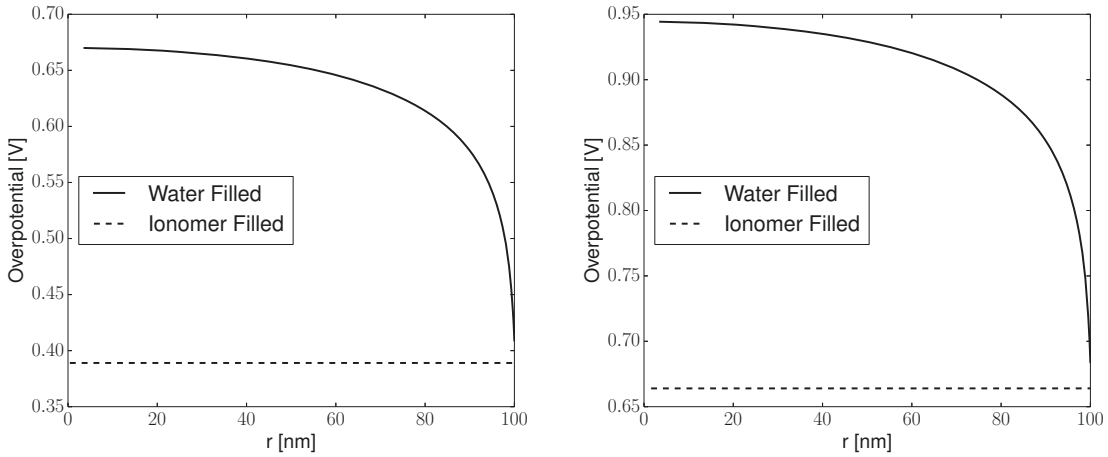

(a) Low Current Density (b) High Current Density

Figure 3.37 – Overpotential profiles across agglomerate cores.

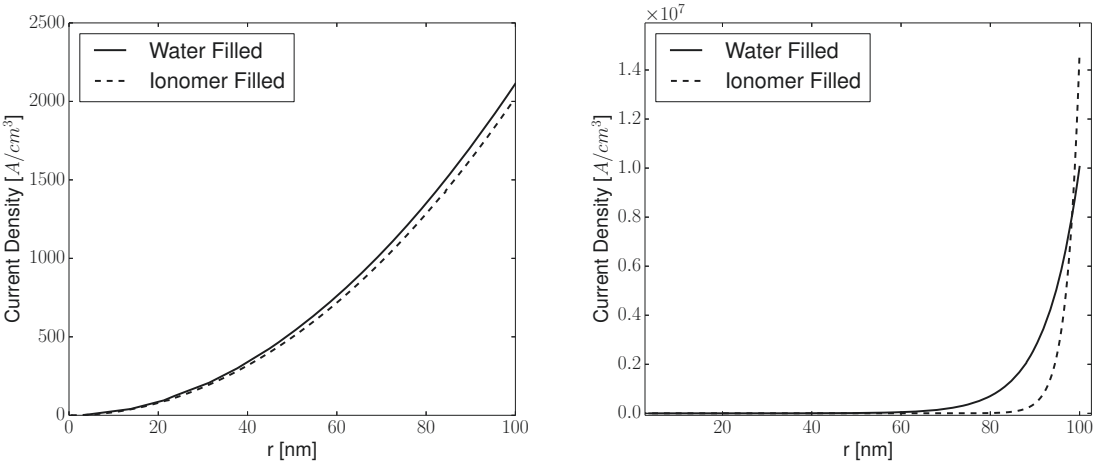

(a) Low Current Density (b) High Current Density

Figure 3.38 – Current density profiles across agglomerate cores.

A parametric study of discussed ionomer and water filled agglomerates over operating conditions as described in Table 3.5. Results of parametric study can be seen in Figure 3.39, showing current density and agglomerate effectiveness across a range of overpotential. It can be seen the water filled model predicts higher reaction rates and improved effectiveness compared to the ionomer filled case. This is due in combination to the increased overpotentials, increased oxygen concentration, and reduced proton concentration as previously discussed.

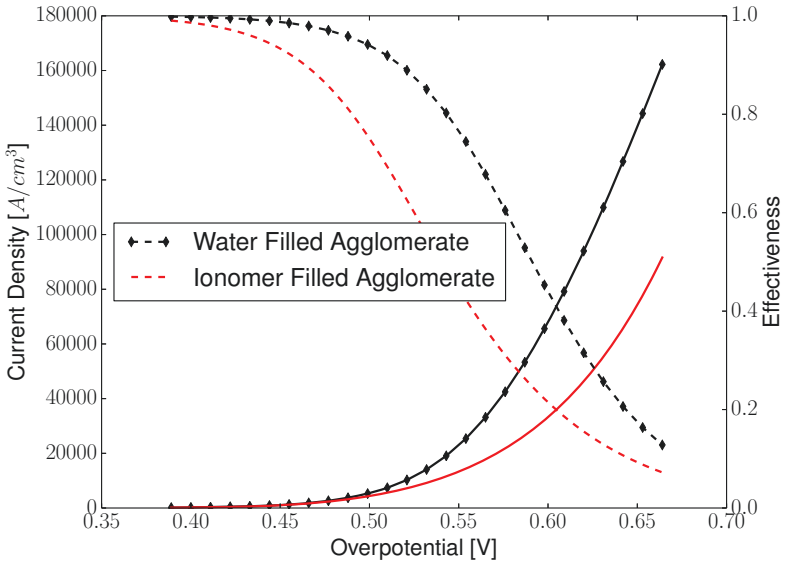

Figure 3.39 – Parametric study of individual ionomer and water filled agglomerates using Tafel Kinetics. Solid lines correspond to current density, dashed lines correspond to agglomerate effectiveness.

When considered individually the water filled agglomerate is highly more reactive and effective than the ionomer filled agglomerate. However throughout this work it has been observed that when considered in a full MEA simulation results may be more subtle. MEA simulations were performed using a multi-scale CCL with water and ionomer filled agglomerate models, using the Tafel kinetics model. Figure 3.40 shows PEFC polarization curves, comparing water and ionomer filled cases. Polarization curves are seen to be very similar, differing at most by 4% in the ohmic region. An early onset of "mass transport" knee can be seen for the water filled case, due to lower layer porosity for the water filled case - this will be discussed in greater detail later.

The large difference in reaction rates of the water and ionomer filled agglomerates when considered individually are less significant when considered in a multi-scale

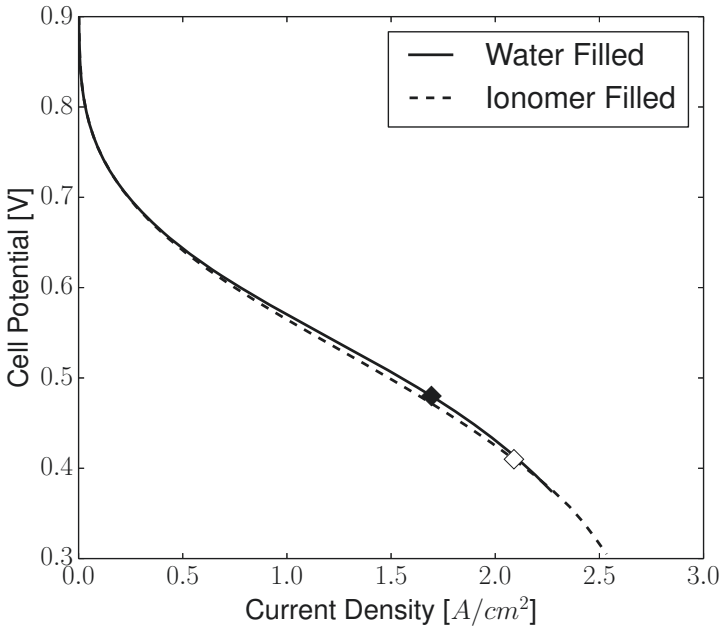

Figure 3.40 – Polarization curve for PEFC using water filled and ionomer filled agglomerates. Diamond markers signify point at which MEA simulation exceeds 100% RH.

MEA simulation, similar to results from previous sections. Figure 3.41 shows reaction rate profiles across the CCL for both water and ionomer filled cases. For the water filled case it can be seen that reaction rate is more intensely concentrated at the left hand side of the CCL, and reaction rates are more evenly distributed across the CCL for the ionomer filled case. This is due in part to the differences in concentration of oxygen across the CCL for the water filled and ionomer filled cases. Figure 3.42 shows oxygen concentration profiles across the CCL for both cases. A greater depletion of oxygen is observed for the water filled case in the lower left hand corner of the CCL. This is due to a combination the reduced porosity of the macro structure due to the water filled assumption as explained in Section 2.4.3.1. The assumption of water filled agglomerates reduces catalyst layer porosity by 20% as compared to the ionomer filled case - Table 3.4.

As noted previously, the assumption of a waterfilled agglomerate reduces catalyst layer porosity, due to the conservation of water within the agglomerate core. In performed simulations macro-scale CL porosity is reduced by 20% for the water filled case compared to the ionomer filled case - Table 3.4. The reduced porosity affects macro-scale mass transport of gaseous oxygen in the CL as observed in Figure 3.42.

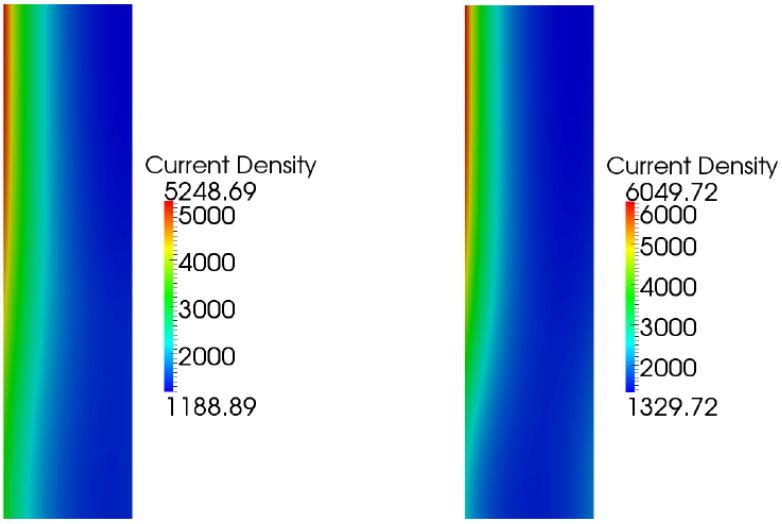

Figure 3.41 – Current density profile in CCL at 2 A/cm^3 for ionomer filled agglomerates (left), and water filled agglomerates (right).

To better appreciate the effect of change in macro-scale porosity caused by micro-scale assumptions, a MEA simulation was performed using the water filled agglomerate, whilst neglecting the water filled agglomerates negative contribution to macro-scale porosity. By neglecting this volume fraction the layer becomes as porous as for the ionomer filled CCL case. Figure 3.43 shows polarization curves for performed simulation. It can be seen that due to increased macro-scale porosity, simulations neglecting the additional volume fraction imposed by the water filled agglomerate demonstrated improved PEFC performance in the mass transport limited region.

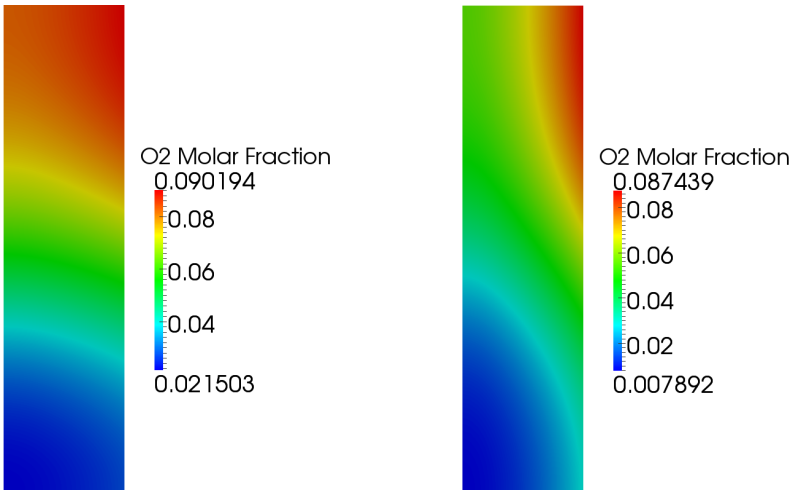

Figure 3.42 – Oxygen concentration profiles in CCL at 2 A/cm^3 for ionomer filled agglomerates (left), and water filled agglomerates (right).

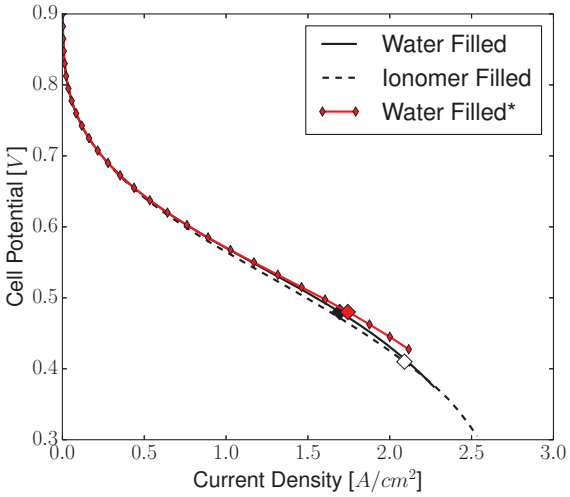

Figure 3.43 – Polarization curves for simulations performed with and without* the water filled assumption's macro-scale volume fraction contribution.

Figure 3.44 shows oxygen concentration profiles across the CCL for the ionomer filled case, water filled case, and water filled neglecting addition volume fraction case. It can be seen that for the water filled case significantly lower oxygen concentrations are experienced across the CCL. Results clearly demonstrate the significance of the additional volume constraint imposed by the water filled case. Thus macro-scale porosity resulting from micro formation is a significant feature of the water filled model.

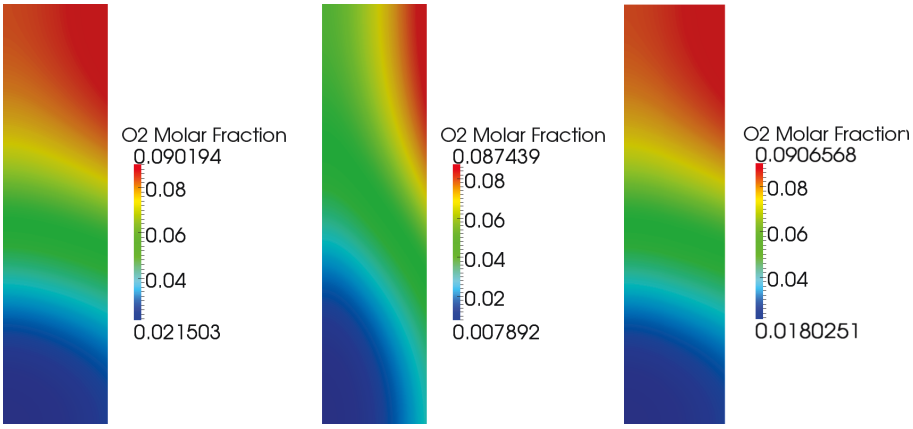

Figure 3.44 – Oxygen concentration profiles in CCL at 2 A/cm^3 for ionomer filled case (left), water filled case (center), and water filled case with no porosity contribution (right).

3.4.1.2 Comparison Using Double Trap kinetics

Before in Section 3.4.1.1 it was shown that water filled agglomerate are more reactive than the ionomer filled agglomerate model when considered using Tafel kinetics. Previously, in Section 3.4.1.1, Figure 3.36 showed how due to the different proton transport mechanisms within ionomer and water filled domains, proton concentration across the agglomerate core is extremely low for the water filled case. Reduced current due to these low proton concentrations was compensated by a large increase in agglomerate overpotential as seen in Figure 3.37.

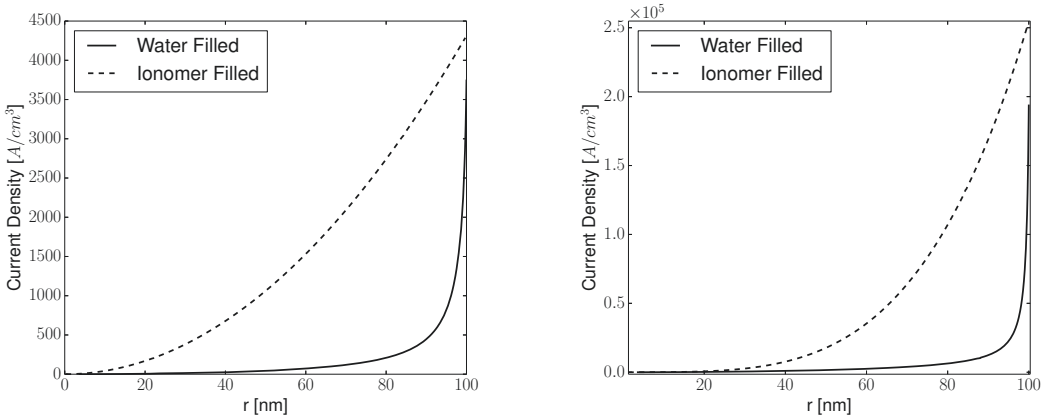

(a) Low Current Density (b) High Current Density

Figure 3.45 – Current density profiles across agglomerate cores using double trap kinetics.

Simulations of individual ionomer and water filled agglomerates were performed, similar to as before in Section 3.4.1.1, except using the double trap kinetic model in order to determine reaction rates of the ORR. Reaction rates across the agglomerate cores for low and high current density operating conditions are show in Figure 3.45. It can be seen that reaction rates within the water filled agglomerate are very low as compared to the ionomer filled model. Reaction diminishment due to low proton concentrations within the water filled agglomerate core is not compensated by higher overpotentials, since the DT kinetics model is not as sensitive to overpotential as the Tafel kinetics model - see Figure 3.1.

A parametric study of ionomer and water filled agglomerates was performed for a range of operating conditions as described in Table 3.5 using the double trap kinetics model. Figure 3.46 shows results of said parametric study. It can be seen that the water filled agglomerate performance is severely diminished over the entire range

of over potentials. Low values of effectiveness highlight the poor proton transport characteristics of the water filled agglomerate, as proton concentration approach zero inside the agglomerate core immediately after the ionomer|core interface as seen in Figure 3.36.

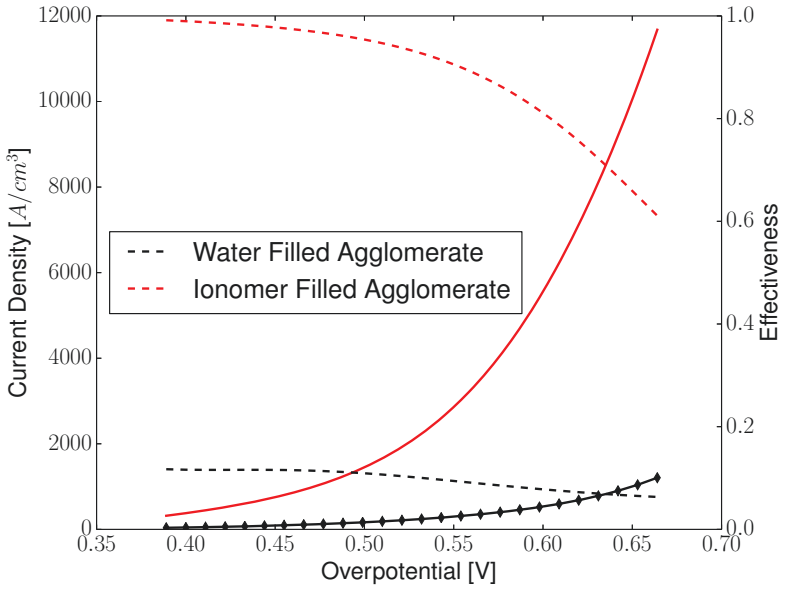

Figure 3.46 – Parametric study of individual ionomer and water filled agglomerates using double trap kinetics. Solid lines correspond to current density, dashed lines correspond to agglomerate effectiveness.

MEA simulations using the multi-scale CCL model with embedded water and ionomer filled agglomerate models, using parameters as described in Tables 3.2 and 3.3, and using double trap kinetics, were performed. Figure 3.47 shows polarization curves of performed simulations. It can be seen that the severely diminished performance of the water filled agglomerate when considered with the double trap kinetics model leads to unrealistically low PEFC performance.

Agglomerate models describe physical characteristics of CL micro structure, which impose mass transport limitations, in turn diminishing FC performance in high current operating regimes. At low current densities mass transport mechanisms are typically insignificant to fuel cell performance as reactant consumption rates are very low. However it can be seen in Figure 3.47 that at low current densities the water filled agglomerate model predicts very low cell potentials, and is in poor agreement with experimentally data.

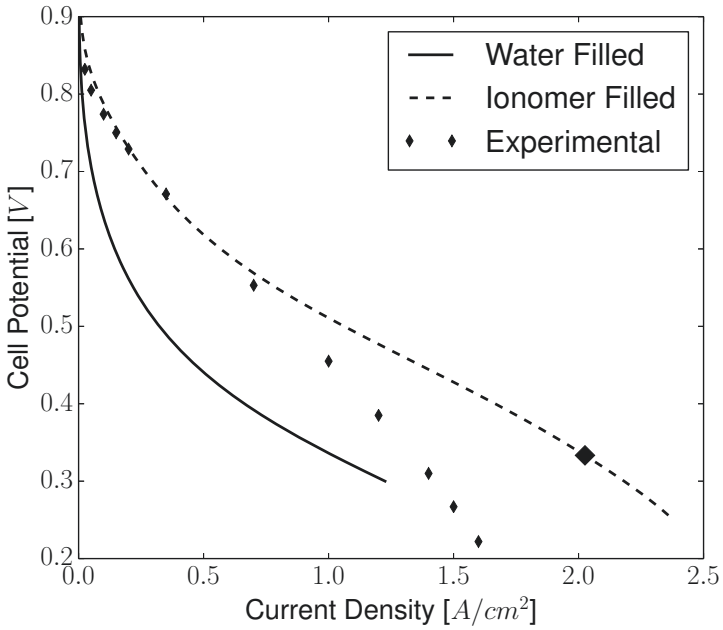

Figure 3.47 – Polarization curve for PEFC using water filled and ionomer filled agglomerates using double trap kinetics. Diamond markers signify point at which MEA simulation exceeds 100% RH.

The unrealistic behaviour of the water filled agglomerate under the presented conditions begs one to question its validity. Primary pores within CCL micro structure have been experimentally observed via porosimetry [71, 72], showing the likelihood of the existence of water filled agglomerates. The presented mathematical description of the water filled agglomerate model proposed by Wang et al. [25] may not accurately describe transport phenomena occurring within.

Poisson's equation describes electrolyte potential in a continuous electrolyte medium due to ionic interactions, however within a platinum loaded carbon core there also exists charged metallic surfaces which may have large effects on proton transport. Therefore the author hypothesizes that the presented water filled agglomerate model may be an incomplete description of electrochemical phenomena occurring within CCL micro structure. Several models have recently appeared in literature [26, 51] that assume water filled cylindrical or conical pores with a charge density applied to the pore walls based on the pore materials potential of zero charge. Available negative volumetric is therefore likely to exist in these agglomerates.

Whilst the existing water filled model does not describe proton mechanisms due to charged carbon surfaces, the effect improved proton transport mechanisms on the

presented multi-scale MEA model may be appreciated by imposing a negative ionic species concentration c_{I^-} inside the water filled core. This negative ionic species will act to increase internal proton concentration. Additional PEFC simulations were performed, in which c_{I^-} was set to a fraction of the concentration of sulphonic groups in Nafion $c_{SO_3^-}$. Figure 3.48 shows polarization curves for performed MEA simulations. It can be seen that if improved proton transport mechanism where to exist within the water filled agglomerate core, PEFC current density predictions would be more similar to ionomer filled and experimental observations. Therefore such a water filled agglomerate transport phenomena seem plausible, and a model which describes such phenomena should be explored within the presented multi-scale framework. The water pore agglomerate model developed by Sadeghi et al. [26] does consider the presence of charged surfaces, and therefore may be a more accurate representation of the PEFC micro structure. Therefore the water pore agglomerate model detailed in reference [26] should be considered within the multi-scale framework developed in this work.

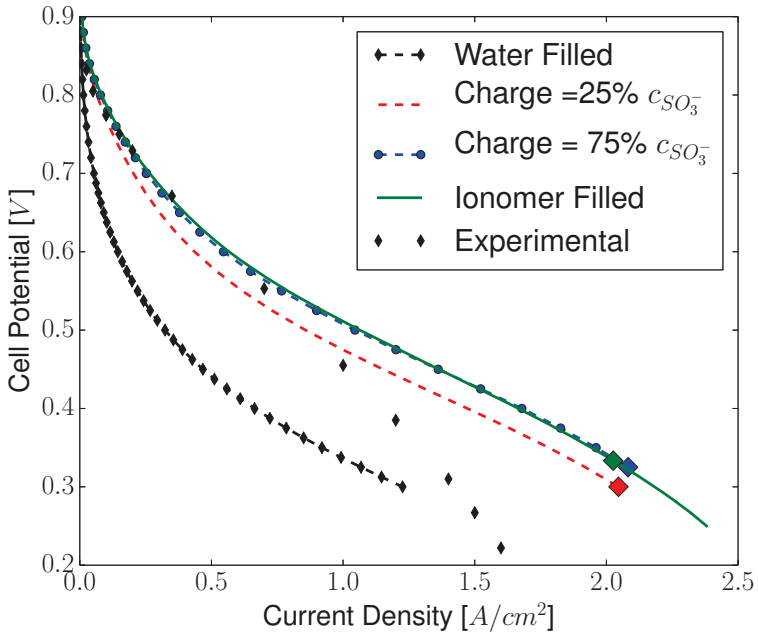

Figure 3.48 – Polarization curve for PEFC using water filled agglomerates with varying core charge densities and the double trap kinetics model. Diamond markers signify point at which MEA simulation exceeds 100% RH.

3.5 Anode Catalyst Layers Agglomerates

In this section the impact of micro structural mass transport losses are assessed using a multi-scale anode catalyst layer model with embedded ionomer filled agglomerates using the double trap kinetics model. Compared to the ORR, the HOR is more rapid, due to the kinetic favourablity of the reaction. Typically it is assumed that the sluggish ORR is responsible to the majority of PEFC potential losses.

Table 3.8 – Operating conditions for anode agglomerates

	Low Current Density	**High Current Density**
ϕ_s	-1.1e-5	-0.02
ϕ_m	-2.6e-5	-0.2
x_{H_2}	0.8	0.8

Typical operating conditions for anode catalyst layer micro structure are described in Table 3.8. Simulations of individual ionomer filled agglomerates using parameters as described in Table 3.3 and the dual path kinetics model were carried out. Figures 3.49 and 3.50 show reaction rate and reactant concentration profiles across the ionomer filled agglomerate cores. It can be seen that at medium and high current densities, reaction rate and reactant profiles are similar. Coupled with the fact that agglomerate reaction rates only increase very gradually below overpotentials if -0.04 V (see Figure 3.51) it can be said that anode catalyst layer micro structure reaches near limiting current at overpotentials equal to $\sim$ -40 mV.

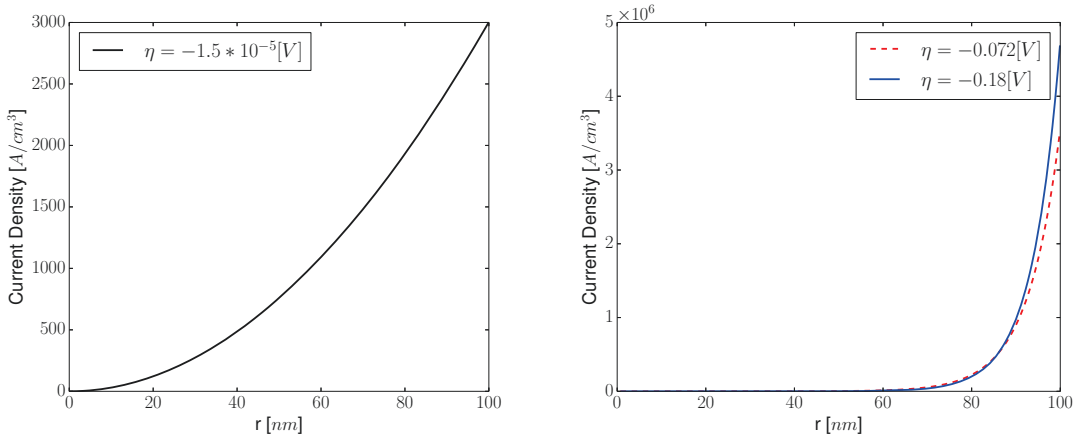

(a) Low Current Densities

(b) Medium and High Current Densities

Figure 3.49 – Current density profiles across anode agglomerate cores.

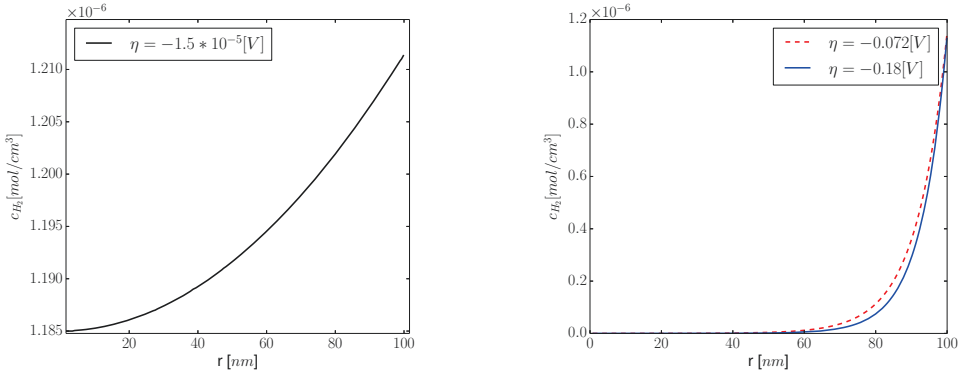

(a) High Current Density

(b) Low Current Density

Figure 3.50 – Hydrogen concentration profiles across anode agglomerate cores.

A parametric study of ionomer filled agglomerates using parameters as described in Table 3.3 w.r.t. overpotential was performed. Result are shown in Figure 3.51. Severe mass transport limited behaviour is observed(low effectiveness), caused by the rapidity of the HOR. Observing Figures 3.46 and 3.51, it can be seen that for the more sluggish ORR, mass transport effects are more subtle (poor effectiveness is only observed at relatively large departure from equilibrium potential).

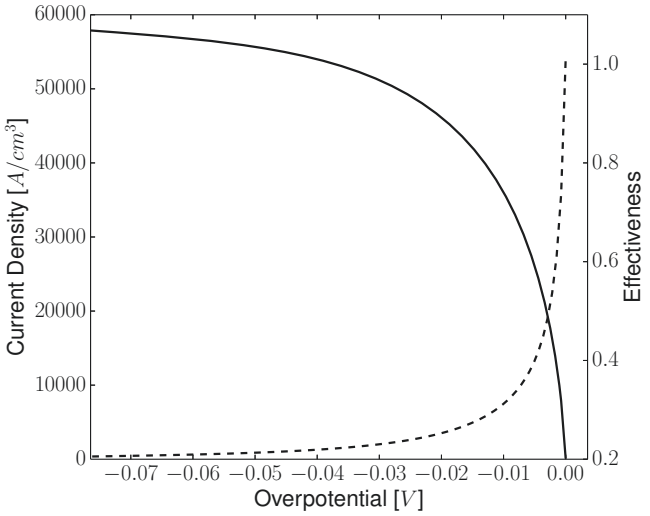

Figure 3.51 – Parametric study of individual ionomer filled anode agglomerates. Solid lines correspond to current density, dashed lines correspond to agglomerate effectiveness.

MEA simulations were performed, using a multi-scale anode CL with embedded ionomer agglomerates and the dual path kinetics model, for parameters as described in Tables 3.2 and 3.3.

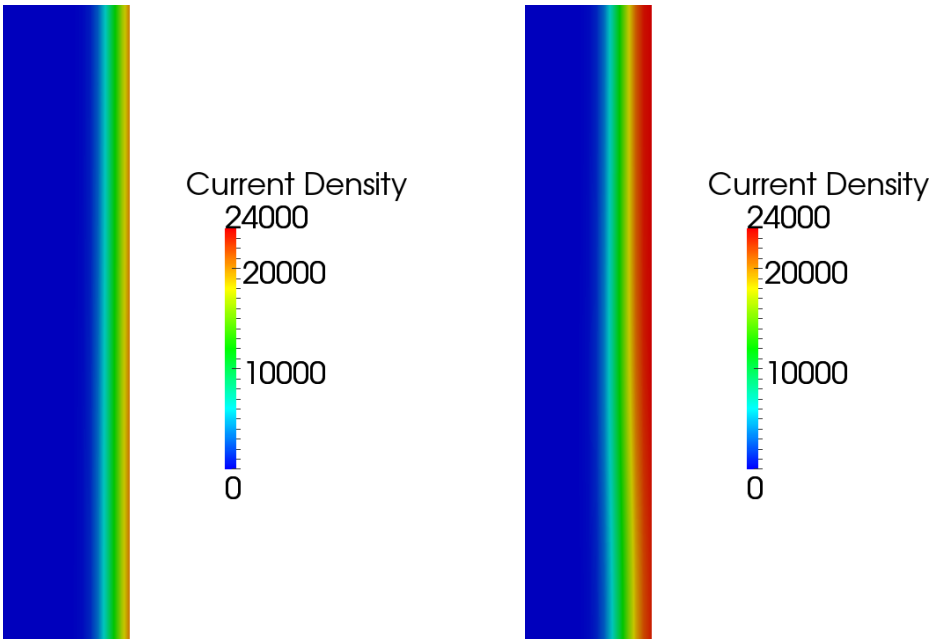

(a) 1.0 A/cm^2 (b) 2.0 A/cm^2

Figure 3.52 – Current density profiles across ACL at 1.0 and 2.0 A/cm^3

Figure 3.52 shows reaction rate profiles across the ACL at various cell current densities. The implications of micro structural mass transport limitations on anode catalyst layer reaction rate profiles are as follows: as current requirements for the anode increase, more of the layer must become active, since the already active micro structure will be already severely mass transport limited. This behaviour can be clearly seen in Figure 3.52 comparing the 1.0 to 2.0 A/cm^3 case. Maximum reaction rate intensities remain relatively similar, but the reaction occupies far more catalyst layer for the 2.0 A/cm^3 case. Figure 3.53 shows overpotential profiles for the two cases. While for the 2.0 A/cm^3 case much higher overpotential are observed close to the membrane as compared to the 1.0, maximum reaction rate intensities at the right hand side of the layer are similar for both cases - Figure 3.52.

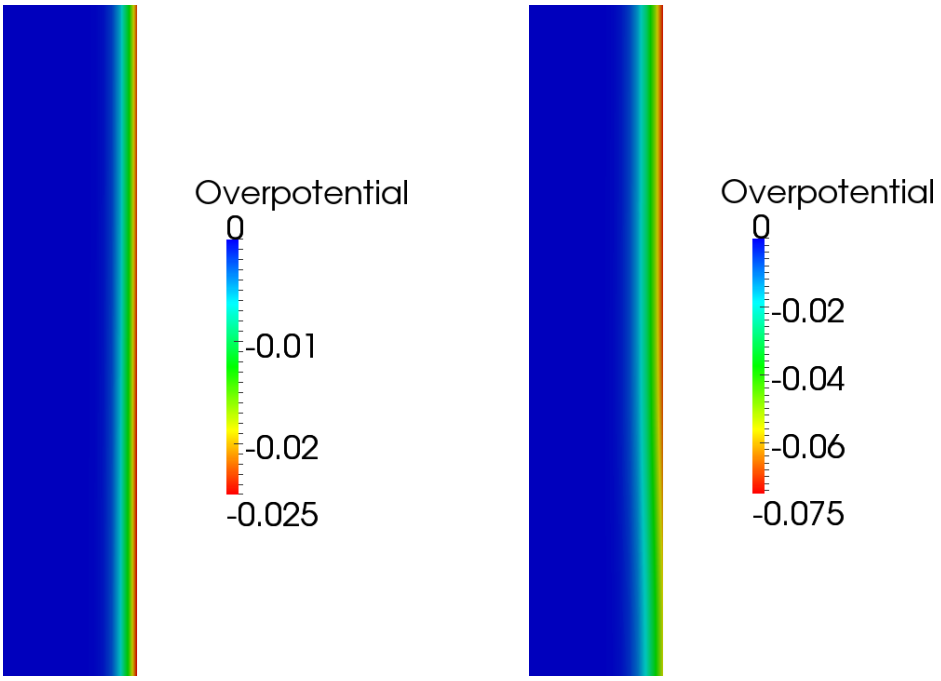

(a) 1.0 A/cm^2 (b) 2.0 A/cm^2

Figure 3.53 – Over potential profiles across ACL at 1.0 and 2.0 A/cm^3

To quantify the significance of ionomer filled agglomerate on total reaction of a MEA several MEA simulations were performed, in which catalyst layer were described using either the homogeneous CL model or the multi-scale CL, as described in Table 3.9.

Table 3.9 – Description of simulations performed to quantify the significance of the multi-scale CL model with embedded micro structure to MEA performance, applied to the ACL and CCL.

Case	Anode CL Model	Cathode CL Model
1	Homogeneous CL	Homogeneous CL
2	Homogeneous CL	Multi Scale CL
3	Multi Scale CL	Homogeneous CL
4	Multi Scale CL	Multi Scale CL

Polarization curves for performed simulations are shown in Figure 3.54. It can be seen by comparing cases 1 and 2, and cases 1 and 3, that the mass transport limiting effects of the ACL micro structure are more significant to PEFC performance that the mass transport limiting effects of the CCL. This is clearly demonstrated by the drastically lower agglomerate effectiveness values presented in this Section, as

compared to previous sections when the cathode was studied. The reason for such ineffective agglomerates in the anode CL compared the cathode CL is the rapidity of the HOR as compared to the ORR.

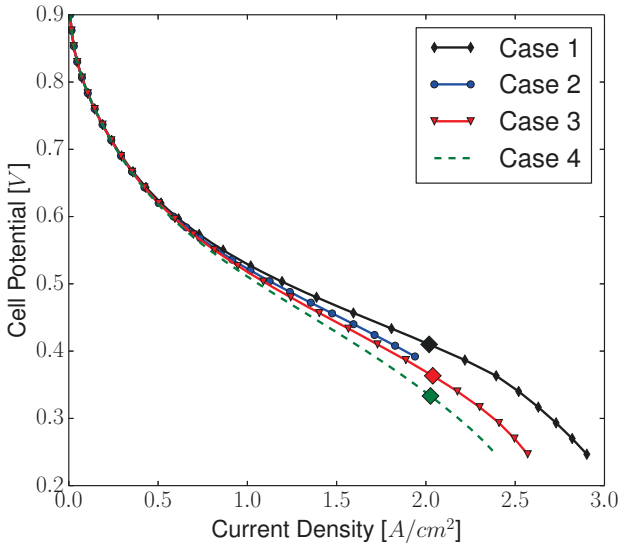

Figure 3.54 – Polarization curves for PEFC cases described in Table 3.9. Diamond markers signify point at which MEA simulation exceeds 100% RH.

Due to the almost immediate mass transport limitations of the agglomerate model due to the acute rate of the HOR it would indicate that efforts in improving anode catalyst layer reaction rates by focusing on micro structural properties may be a fruitless pursuit. Instead the layer should be optimized in order to improve ionomer phase charge transport, so that more of the layer can become electrochemical active. Secanell et al. [2] performed such optimizations and was able to predict a decrease in potential losses of the ACL.

Secanell et al. [2] reports a voltage drop across the anode of ∼22 mV at 2.0 A/cm^3 electrode current density, far smaller than this work, equal to 42 mV. The primary reason for this large difference is effective proton conductivity of the ACL. Secanell et al. [2] use a bulk proton conductivity value σ_m equal to 0.079628 S/cm. In this work for a ACL humidified with input gasses at 50% RH bulk proton conductivity is calculated equal to 0.03297 S/cm. Hence material properties used by Secanell et al. [2] provide greater proton conductivity. Additionally layer volume fractions used by Secanell et al. [2] shown in Table 3.10 provide greater proton and electrical conductivity.

Voltage losses in ACL simulated in this work can be reduced by improving pro-

Table 3.10 – ACL volume fractions reported by Secanell et al. [2], and used in this work (as a result of input parameters from Table 3.2)

Anode Electrode Layer Property	Secanell	This work
Sold %	0.3186	0.2956
Void %	0.2624	0.5645
Electrolyte %	0.419	0.1397

ton conductivity. Proton conductivity is a function of ionomer humidifcation, and therefore can be improved by increasing the humidity of the input gas to the anode. MEA multi-scale simulations were performed with input anode gasses fully humidified (100% RH), whilst keeping all other operating conditions the same as before. Figure 3.55 shows polarization curves for 50% RH and 100% RH cases. It can be seen that cell potential is greatly improved by humidifying the input gas. Figures 3.55 3.56 show overpotential and current density profiles across the ACL at 2.0 A/cm^3. It can be seen that for the 100% RH case more of the ACL is electrochemically active, due to improved overpotential profiles resulting from improved proton conductivity. At 2 A/cm^3 the voltage drop across the anode, dV, is reduced from 42 mV to 26 mV by increasing the input gas RH.

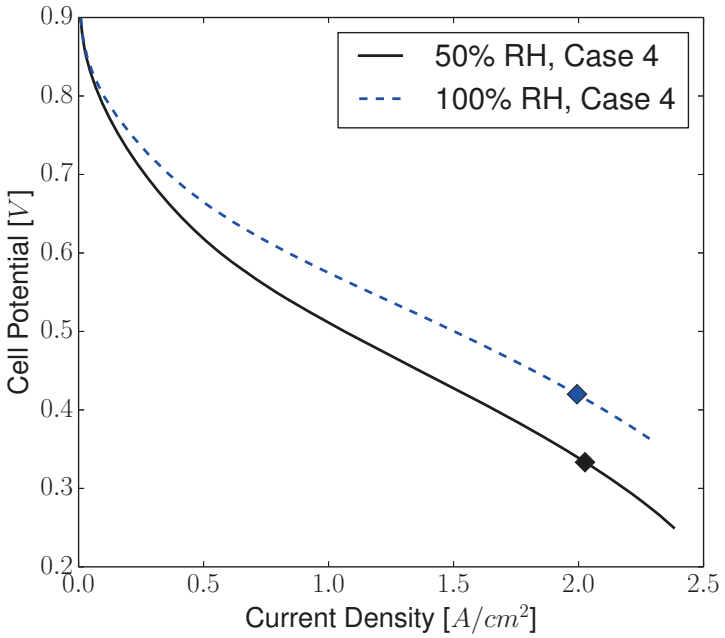

Figure 3.55 – Polarization curve for PEFC with varying anode input gas RH. Diamond markers signify point at which MEA simulation exceeds 100% RH.

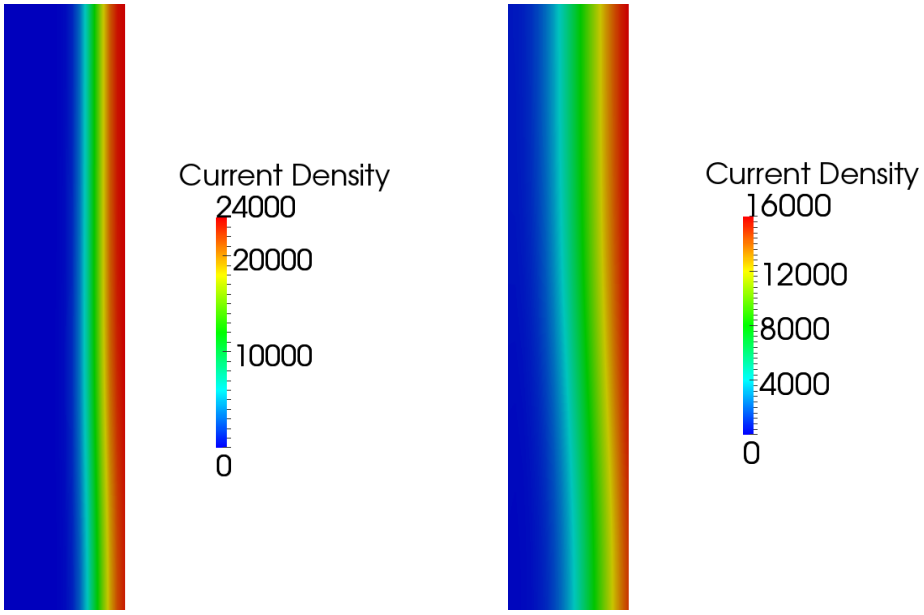

(a) 50 % RH (b) 100 % RH

Figure 3.56 – Current density profiles across ACL with varying input gas RH, at 2.0 A/cm^3

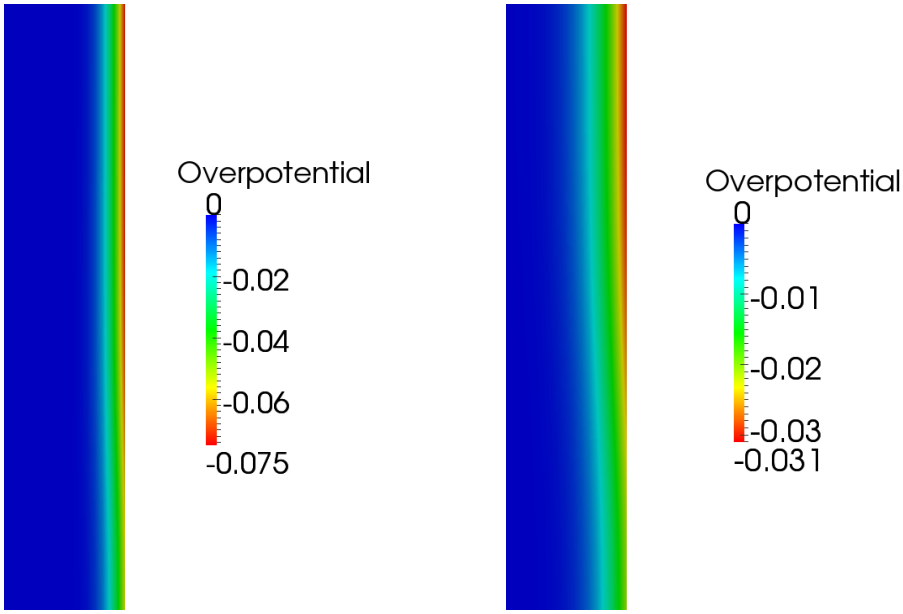

(a) 50 % RH (b) 100 % RH

Figure 3.57 – Over potential profiles across ACL with varying input gas RH, at 2.0 A/cm^3

3.6 Ionomer Covered Catalyst Particle

In this section the Ionomer Covered Catalyst Particle (ICCP) model developed in Section 2.4.4 is investigated as a potential method for describing micro scale mass transport limitations of PEMFC micro structure. Input model parameters used the ICCP are the same as for the ionomer and water filled agglomerates, shown in Table 3.3. Given a particle radius of 100 nm, the film thickness of the ionomer film is calculated as 11.66 nm due to the assumption of zero porosity of the ICCP core . This is the same value as the water filled agglomerate - Table 3.4.

Mass transport in the ICCP is primarily limited by the ionomer thin film. Both the Henry's law and non equilibrium boundary condition proposed by Suzuki et al. [48] are implemented. A parametric study of the ICCP model for the operating condition range described in Table 3.5, using the double trap kinetics model, was performed. Simulation results are shown in Figure 3.58. Both boundary conditions are considered for comparison purposes.

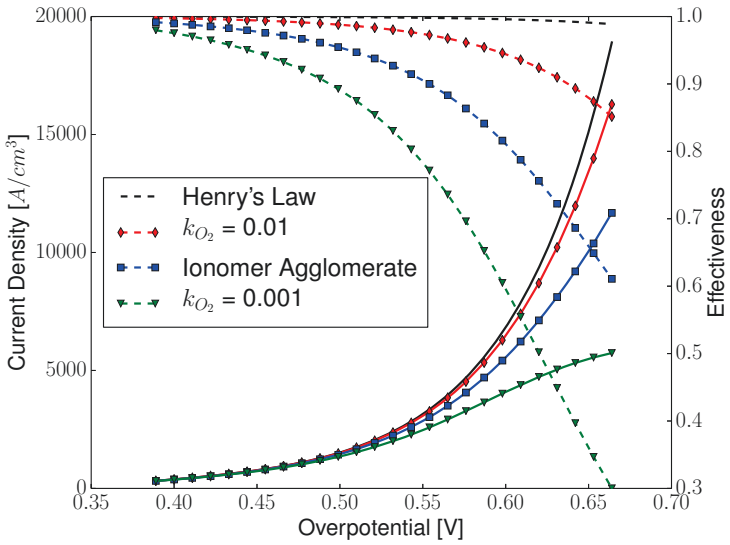

Figure 3.58 – Parametric study of individual ICCP for different boundary conditions. Solid lines correspond to current density, dashed lines correspond to effectiveness.

Figure 3.58 also shows results for an ionomer filled agglomerate using the Henry's law boundary, and double trap kinetics, for comparison. It can be seen that the ICCP with Henry's law boundary condition predicts significantly larger current density compared to the ionomer filled agglomerate model. Similar to results in Section 3.3.4, it can be seen here that the contribution of the ionomer thin film is insignificant, since

the effectiveness of the ICCP at HCD is 99 %. When the ICCP is considered using the non equilibrium boundary condition however a significant drop in current density and micro structural effectiveness are observed. For $k_{O_2} = 0.001$ m/s current density of the ICCP is reduced substantially.

MEA simulations were performed using a MEA model with multi-scale cathode catalyst layer and embedded ICCP model using the double trap kinetics. Polarization curves are shown in Figures 3.59 and 3.60. It can be seen for the ICCP case using Henry's law boundary condition, simulation results are identical to homogeneous CCL case, since the ICCP model using Henry's law boundary condition imposes virtually zero micro scale mass transport losses. For $k_{O_2} = 0.001$ m/s significant losses in predicted current density are observed, and the cell approaches a limiting current of ~ 1.8 A/cm^3.

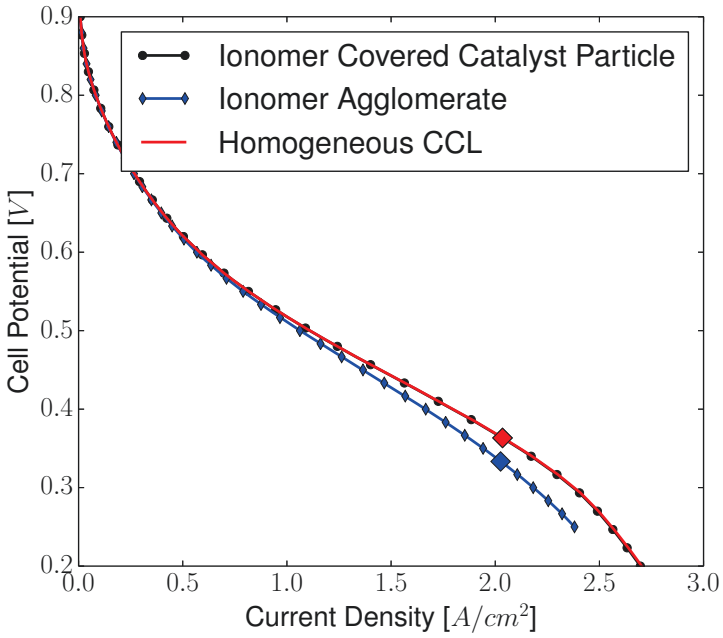

Figure 3.59 – Polarization curve for PEFC using various micro structure models. Diamond markers signify point at which MEA simulation exceeds 100% RH.

Based on results from Figures 3.58 - 3.60 it can be seen specific cases the ICCP model can represent significant mass transport losses. Due to the model's high reliance on the value of k_{O_2} further experimental characterization of the non-equilibrium oxygen dissolution mechanism in ionomer thin films is required to definitively quantify transport limitations incurred by the existence the ICCP morphology.

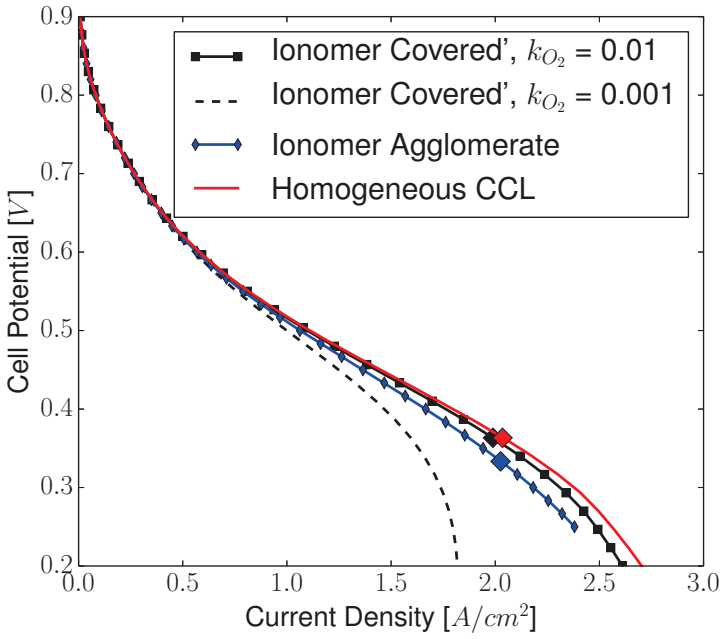

Figure 3.60 – Polarization curve for PEFC using various micro structure models. Diamond markers signify point at which MEA simulation exceeds 100% RH.

Experimentally a range of dimensions of micro scale morphology have been shown to exist within PEFC CL [1, 46]. In this work an agglomerate size polydispersion has already been considered, and it was found that the MEA model was insensitive to the reported range of dimensions. Given the fact a combination of different micro scale dimensions occur within fabricated PEFC CLs, one may postulate that a combination of different morphologies also exists i.e. agglomerates and individual particles. Using the multi scale, polydisperse frameworks and micro scale models developed in this work a combination of micro scale morphologies may be considered for the first time.

An arbitrary demonstration of the discussed polydisperse morphology concept is presented. It is hypothesized that due to the dimension of primary catalyst particles ($\sim$ 20 nm), micro scale structures in size smaller than a certain dimension have morphology similar to the ICCP. In this work it is assumed that CL micro structures with radii $\approx$ 25 nm have a ICCP morphology, and structures larger than $\approx$ 25 nm are water filled agglomerates. Based on these assumptions and using the micro structural dimensions described by Epting and Litster [1], a combination of micro scale morphologies as described in Table 3.11 is obtained.

MEA simulations were performed considering the combination of micro structures

Table 3.11 – Agglomerate size distributions taken from Epting and Litster [1] with hypothesized morphologies type.

Radius, nm	Film, nm	Volume fraction, %	Type
23	2.74	11.50	Ionomer covered catalyst particle
40	4.67	14.80	Water filled agglomerate
56	6.57	11.20	Water filled agglomerate
72	8.37	16.20	Water filled agglomerate
88	10.36	14.00	Water filled agglomerate
105	12.26	12.20	Water filled agglomerate
121	14.17	11.20	Water filled agglomerate
137	16.07	5.60	Water filled agglomerate
154	17.96	2.10	Water filled agglomerate
170	19.8618	1.20	Water filled agglomerate

detailed in Table 3.11, using parameters described in Tables 3.2,3.3 and the double trap kinetics model. Additionally two different cases are presented: in the first case the negative ionic species concentration c_{I^-} inside the water filled agglomerates is equal to 0, and for the second case is equal to $0.4 \times c_{SO_3^-}$. All micro scale models assume equilibrium oxygen boundary conditions.

Polarization curves for performed simulations are presented in Figure 3.61. Results for standard water and ionomer filled agglomerate models, using Double trap kinetics, presented in previous section are included for comparison. It can be seen for case 1, that the combination of the highly reactive ICCPs with water filled agglomerates improves model predictions in the kinetic and ohmic operating regions as compared to the standard water filled case. Case 2 produces results in better agreement with the ionomer filled agglomerate case due to the inclusion of negative ionic species concentration in water filled agglomerates equal to $0.4 \times c_{SO_3^-}$.

The performed demonstrations, whilst perhaps not being truly representative of actual PEFC CL micro-structural morphology, illustrates the flexibility of the implemented multi-scale and polydisperse framework. Coupled with more detailed experimental characterization of PEFC CLs the developed framework can be utilized to provide a more detailed description of PEFC mass transport limited behaviour.

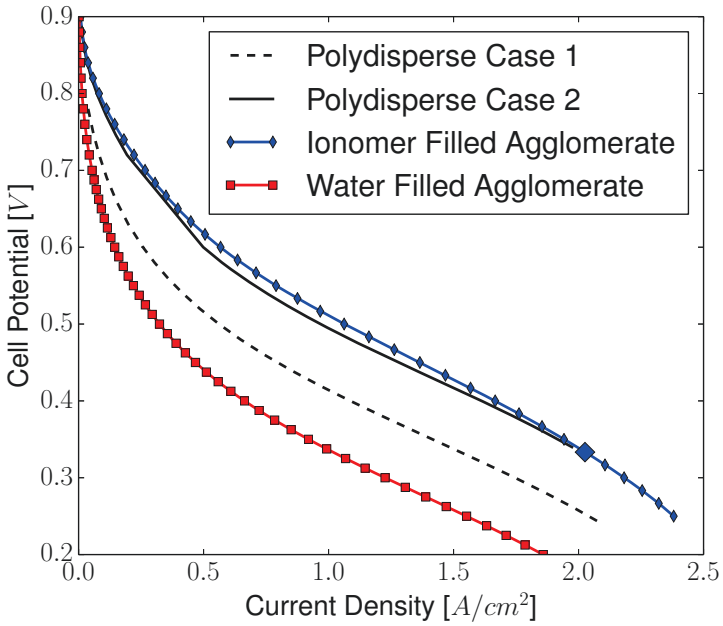

Figure 3.61 – Polarization curve for PEFC considering polydisperse micro scale morphology. Diamond markers signify point at which MEA simulation exceeds 100% RH.

3.7 Model Convergence and Speed Improvements

Several benchmarks were performed to quantify the improvements to convergence and speed of execution of agglomerate and MEA multi-scale simulations, due to implementation of the agglomerate initial solution framework and parallelization of the multi-scale catalyst layer model.

Dobson [5] reported difficulty in gaining convergence of the water filled agglomerate at medium to large overpotentials. In this work several approaches were investigated to improve convergence of the numerical agglomerate models, including reformulation of said models, and implementation of a more robust initial solution framework as described in Section Appendix A:. A parametric study of water filled agglomerates for parameters described in Tables 3.2 and 3.3, using Tafel kinetics, for operating conditions described by Table 3.5 was performed. Simulation results may be seen in Figure 3.62. Without the initial solution framework developed as part of this work it can be seen that the water filled agglomerate model experiences convergence issues at very low over potentials ($\sim$0.425 V), whilst with the new initial solution framework a complete parametric study up to 0.65 V is possible.

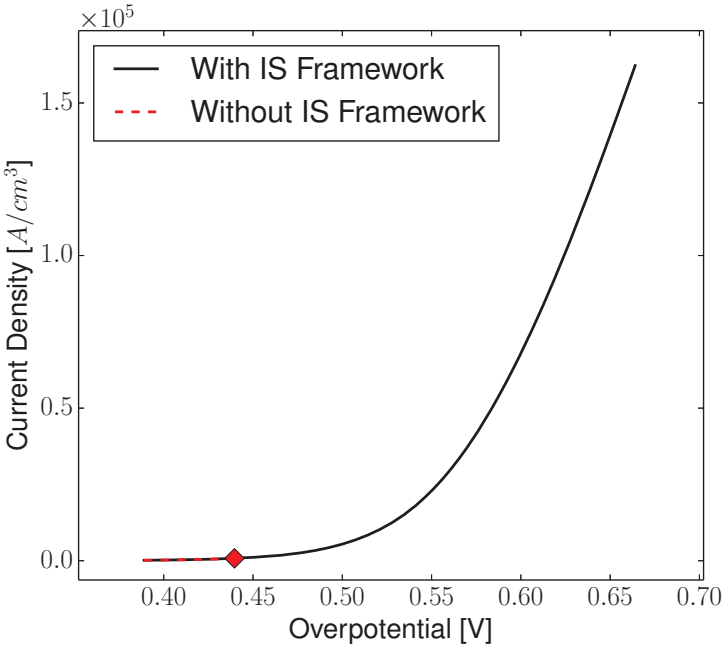

Figure 3.62 – Parametric study of water filled agglomerate model, with and without the use of the initial solution framework developed as part of this work. Without the initial solution framework the water filled model fails to converge at overpotentials above 0.44 V .

MEA simulations using the water filled agglomerate model were carried out in Section 3.4.1.1. Polarization curves for Tafel kinetic case are shown in Figure 3.40. Using the new initial solution framework convergence of this simulation was possible to an operating cell potential of 0.375 V . However, without the initial solution framework, convergence is only possible to an operating cell potential of 0.7 V . These results clearly demonstrate the value of the initial solution framework implemented as part of this work, as it allows one to explore simulated phenomena over a larger range of operating conditions.

Multi scale simulations with embedded numerical agglomerates can be very time consuming, since to evaluate cell performance for one point cell potential can require tens of thousands of agglomerate model evaluations and these evaluations can take time on the order of seconds. In order to complete a parametric study of a fuel cell, i.e. produce one entire polarization curve, OpenFCST can take days to weeks of time. As described in Section Appendix B:, as part of this work the multi-scale catalyst layer model was improved so that evaluation of several agglomerates could be perform simultaneously by several processors. The parallel execution of OpenFCST allows for evaluation of developed models in a feasible time frame, which was instrumental for

acquiring results for this work.

Table 3.12 – Simulation benchmarks

Case	Description	Serial [s]	Parallel [s]	Speed-up Factor
1	Poly disperse simulations using analytical ionomer filled agglomerate	18.6	16.3	1.14
2	Mono disperse simulations using numerical ionomer filled agglomerate	16978	6731	2.52
3	Poly disperse simulations using numerical ionomer filled agglomerate	153900	21576	7.13

Several simulations which have already been presented throughout this work were performed in serial and parallel modes in order to appreciate the speed up provided by code parallelization. Comparison of time taken for MEA evaluations at an operating potential of 0.6 V are Tabel 3.12. Benchmarks were performed on a dedicated simulation server: 2 Intel® Xeon CPU E5-2690 v2 @ 3.00GHz, a total 20 individual cores, and 390 GB of random access memory. Large speed up are observed for simulations which require a large number of evaluations of the numerical agglomerate models, specifically the polydisperse simulation which requires ten agglomerate simulations per quadrature point - ten times more than typical. A smaller speed increase is observed for the analytical agglomerate expressions, due to the smaller computational requirements compared to the numerical expression.

Chapter 4

Conclusion and Future Work

4.1 Conclusion

This work focused on improving understanding of mass transport limiting phenomena occurring within the micro-structure of PEFC CL. The existing multi-scale framework was utilized to investigate the mechanism of proton conductivity in ionomer within CL micro-structures, the effect of kinetics on mass transport limited FC operation, and the performance characteristics of the ACL. The multi-scale framework was improved to investigate non equilibrium oxygen dissolution mechanism in ionomer thin films, non homogeneous catalyst distributions throughout CL micro-structures, micro-structure size and morphology polydispersions, and different CL morphologies other than agglomerates. Additionally improved stability of micro scale models and computational speed improvements permit thorough comparisons previously impossible.

The effect of kinetic choice on PEFC performance was thoroughly assessed. Two ORR kinetics models were compared: the Tafel kinetics model and the Double Trap kinetics model. The Tafel kinetics model was shown to be highly sensitive to overpotential, generally predicting larger reaction rates. The large reaction rates predicted by the Tafel kinetics model at high current densities operating conditions, were found to predict current density to be most highly concentrated at the CL:ML interface, and to exaggerate the importance of the ionomer thin film in agglomerate models. The Double Trap kinetics model was found to predict more realistic reaction rates when compared to experimental data. Additionally using the Double Trap model, more evenly distributed current density profiles across the CCL and agglomerate domains are observed. The Double Trap kinetic model is recommended as the ORR kinetic model of choice, since its reaction rate predictions are more accurate than the Tafel

kinetics model, and are less likely to incorrectly emphasize certain micro scale mass transport phenomena.

In this work the Double Trap kinetics model was improved to add sensitivity to proton conductivity. The presented model can now be used to determine reaction rates in domains where constant proton concentration may not exist, i.e. water filled agglomerates. The improved model shows agreement with experimental literature, however the reduction in proton reaction order at overpotentials from 0.3 to 0.6 V requires additional experimental clarification.

The significance of proton transport occurring within ionomer filled CL micro-structures was assessed and found to have an insignificant effect on PEFC performance. In order for appreciable effects to be observed, experimentally measured values of proton conductivity needed to be reduced by four orders of magnitude. Therefore the assumption of iso-protonic potential in micro-scale models appears reasonable. In future, micro scale models developed to describe mass transport limited behaviour of the CL need not describe proton transport mechanism occurring within ionomer.

The non-equilibrium oxygen dissolution process in ionomer thin films described by Suzuki et al. [48] was found to be significant for values of $k_{O_2} \leq 0.01$ m/s. The non-equilibrium dissolution process appears to be a viable contributing factor in the explanation of micro scale mass transport losses in PEFCs. However there is still much experimental uncertainty at this time regarding the value of reaction coefficient k_{O_2}. The presented multi-scale framework coupled with further experimental efforts can be utilized to definitively quantify this phenomenon's significance.

The agglomerate models presented in this work were improved to describe non homogeneous catalyst loading profiles, providing a more accurate representation of experimentally observed structures. An investigation of micro-scale catalyst grading was performed. It was found that PEFC CL performance was strongly dependent on the location of catalyst within the micro-structure. As platinum is pushed to the centre of the agglomerate core the effective diffusion pathway through the agglomerate porous structure become increasingly long, resulting in larger diffusion losses. When considered in a MEA simulations, mass transport limiting micro-scale catalyst loading profiles produce performance predictions that significantly differ from a homogeneous catalyst distribution. The catalyst distribution can be modified to more

accurately match experimental results. Therefore losses incurred due to non homogeneous catalyst distribution in CL micro-structures appear to be a viable contributing factor in the explanation of micro scale mass transport losses in PEFCs.

Epting and Litster [1] reported that describing agglomerate size distribution correctly was a crucial factor for accurately representing PEFC CL micro-structure, and that the representation of CL micro-structure using a single representary agglomerate radii leads to significant errors. Using the multi-scale and polydisperse frameworks developed in this work the effect of an agglomerate size polydispersion on PEFC performance was investigated. It was found that agglomerate size polydispersion is not as significant as previously thought, since the MEA model is insensitive to the range of agglomerate dimensions observed. Other transport phenomena discussed in this work appear to be more significant than the aspect of agglomerate size polydispersion. Therefore a single representary size of micro scale model may be chosen for MEA simulations.

A detailed comparison of the water and ionomer filled model was carried out using Tafel and Double Trap kinetics. For Tafel kinetics it was found that the water filled model predicted significantly higher reaction rates than the ionomer filled model, due to improved oxygen diffusivity in the agglomerate core. However when considered in a multi-scale CL framework the differences in performance between the two micro-scale models did not result in a difference in PEFC performance. Changes in macro scale overpotential and reactant concentration acted to counteract the more reactive water filled agglomerate. Additionally the decreased macro scale porosity due to the assumption of the water filled agglomerate was found to be a significant factor in adversely affecting macro scale gaseous transport.

The water filled and ionomer filled models were compared using Double Trap kinetics model. Drastically decreased performance for the water filled agglomerate model was observed, caused by low proton concentrations existing in the water filled agglomerate core. Previously these low proton concentrations were compensated by increased overpotentials existing in the water filled agglomerate core, but were not compensated in this instance due to the Double Trap model's lower sensitivity to overpotential as compared to the Tafel model. PEFC simulations using the water filled agglomerate and Double Trap kinetics model produced simulation results in poor agreement with experimental data. Therefore it is concluded that the proton transport mechanisms described by the existing water filled agglomerate model are

not truly representative of the proton transport mechanism actually occurring in water filled carbon porous structures. Further work is needed in this area, such as the implementation of a potential dependant metal surface charge, recently proposed in references [26, 51].

Platinum catalyst has been observed to deposit at the surface carbon particles with low internal porosity. In this case the thin film is the major limitation to mass transport. To describe this type of morphology the ionomer covered catalyst particle (ICCP) model was developed. Using the non equilibrium oxygen dissolution boundary condition, with a value of $k_{O_2} \approx 0.001$, the ICCP appears to be a viable explanation of micro scale mass transport losses in PEFC. The validity of this model is highly dependent on the experimental value of k_{O_2}, which is still highly uncertain. It was proposed that multiple types of micro scale morphology may exist within PEFC CLs. A proof of concept simulation was performed, demonstrating the developed frameworks capability of representing such polydisperse morphologies if they were to exist.

Improvements in model stability and speed of execution carried out as part of this work have allowed much of the analysis presented in Section 3 to be performed in a timely manner. Using the improved framework future research is possible over a more comprehensive range of scenarios than previously possible.

Throughout this work it was found that by only considering results of micro scale models, misleading and incorrect conclusions regarding the significance of certain phenomena were easily made. Epting and Litster [1] for instance, report that agglomerate size poly dispersion is crucial in correctly representing CL micro-structures based on assessments of an agglomerate model. This work, as previously discussed, showed the conclusion of Epting and Litster [1] is invalid for full scale PEFC behaviour. Therefore it is concluded that for results to be truly meaningful, micro scale models must be considered within a multi scale framework.

Analysis of the anode catalyst layer highlighted mass transport limiting behaviour occurring on two scales. The diffusion of hydrogen into CL micro-structure is rate limiting due to the rapidity of the HOR, resulting in poor utilization of platinum catalyst. In order to increase current produced by the ACL, more of the ACL domain must become electrochemically active. Poor proton conductivity was found to inhibit the activation of more of the ACL. The humidification of ACL input gasses was demonstrated as a method for significantly improving ACL performance, as it

significantly improved conductivity characteristics of the layer.

In summary the description of many proposed mass transport phenomena have been integrated into the presented multi scale framework, providing a more detailed and accurate description of PEFC mass transport limited behaviour. Coupled with experimental efforts the presented framework can be used to more accurately identify and quantify key performance limiting factors of PEFC operation, improving understanding, and facilitating better design of PEFCs.

4.2 Future Work

Several avenues exist for the improvement of models developed in this work exist. Firstly the integration of a water filled agglomerate model capable of describing proton phenomena in water filled carbon pores accurately should be pursued, so that detailed analysis and comparison with existing models can be performed, to gain a better understanding of said phenomena. The water filled models presented by Sadeghi et al. [26] and Zenyuk and Litster [85] are potentially appropriate for this task.

Many transport phenomena which depend on the geometric description of micro scale morphology, such as the existence of non homogeneous catalyst distribution in CL micro-structures, and the existence of different types of micro structural morphologies, require improved coupling to experimental observations of different catalyst powders. Characterization of images of said micro structure could be coupled with micro scale models developed in this work, improving the accuracy of the model's description, whilst simultaneously providing a platform for experimentally observed micro structures to be directly modeled.

The improved Double Trap kinetic model can now be used to predict reaction rates according to cell potentials, oxygen concentration, and now proton concentration. However further experimental validation of the developed model is required. Specifically, the reduction in proton reaction order at overpotentials 0.3 to 0.6 V warrant further validation.

Finally, further clarification of the non equilibrium oxygen dissolution rate constant k_{O_2} is required. The non equilibrium oxygen dissolution mechanism has been

found in several instances to be significant and a potential explanation for PEFC mass transport limited behaviour, however much uncertainty regarding the value of this parameter still remains.

References

[1] Epting W. K and Litster S. Effects of an agglomerate size distribution on the {PEFC} agglomerate model . *International Journal of Hydrogen Energy*, 37(10): 85058511, 2012. ISSN 0360-3199. doi: 10.1016/j.ijhydene.2012.02.099. International Conference: Photosynthesis Research for Sustainability.

[2] Secanell M, Karan K, Suleman A, and Djilali N. Optimal Design of Ultralow-Platinum PEMFC Anode Electrodes. *Journal of The Electrochemical Society*, 155(2):B125B134, 2008. doi: 10.1149/1.2806171.

[3] Bhaiya M. An open-source two-phase non-isothermal mathematical model of a polymer electrolyte membrane fuel cell. Master's thesis, University of Alberta, 2014.

[4] Mukherjee P. P, Kang Q, and Wang C.-Y. Pore-scale modeling of two-phase transport in polymer electrolyte fuel cells-progress and perspective. *Energy Environ. Sci.*, 4:346369, 2011. doi: 10.1039/B926077C.

[5] Dobson P. Investigation of the Polymer Electrolyte Membrane Fuel Cell Catalyst Layer Microstructure. Master's thesis, University of Alberta, 2011.

[6] Wang J, Uribe F, Springer T. E, Zhang J, and Adzica R. R. Intrinsic kinetic equation for oxygen reduction reaction in acidic media: the double tafel slope and fuel cell applications. *Faraday Discuss.*, 140:347362, 2008.

[7] Moore M. Investigation of the Double-Trap Intrinsic Kinetic Equation for the Oxygen Reduction Reaction and its implementation into a Membrane Electrode Assembly model. Master's thesis, University of Alberta, 2012.

[8] Pyper J. Is 2014 the Year of the Fuel Cell Car?, January 2014.

[9] Wang Y, Chen K, Mishler J, Cho S, and Adroher X. A review of polymer electrolyte membrane fuel cells: Technology, applications, and needs on fundamental research. *Applied Energy*, 88(4):9811007, 2011.

[10] Secanell M, Putz A, Zingan V, Bhaiya M, Moore M, Dobson P, Wardlaw P, and Domican K. *Fuel Cell Simulation Toolbox (FCST): User and Developer's Reference Guide*.

[11] Secanell M. *Computational Modeling and Optimization of Proton Exchange Membrane Fuel Cells*. PhD thesis, University of Victoria, 2007.

[12] Dobson P, Lei C, Navessin T, and Secanell M. Characterization of the PEM Fuel Cell Catalyst Layer Microstructure by Nonlinear Least-Squares Parameter Estimation. *Journal of The Electrochemical Society*, 159(5):B514B523, 2012. doi: 10.1149/2.041205jes.

[13] Wang C.-Y. Fundamental models for fuel cell engineering. *Chemical Reviews*, 104(47274766), 2004.

[14] Grujicic M, Zhao C, Chittajallu K, and Ochterbeck J. Cathode and interdigitated air distributor geometry optimization in polymer electrolyte membrane (PEM) fuel cells . *Materials Science and Engineering: B*, 108(3):241252, 2004. ISSN 0921-5107. doi: 10.1016/j.mseb.2004.01.005.

[15] Eikerling M and Kornyshev A. Modelling the Performance of the Cathode Catalyst Layer of Polymer Electrolyte Fuel Cells. *Journal of Electroanalytical Chemistry*, 453(1-2):89106, August 1998.

[16] Bevers D, Wohr M, Yasuda K, and Oguro K. Simulation of a Polymer Electrolyte Fuel Cell Electrode. *Journal of Applied Electrochemistry*, 27(11):12541264, November 1997.

[17] Kulikovsky A, Divisek J, and Kornyshev A. Modeling the Cathode Compartment of Polymer Electrolyte Fuel Cells: Dead and Active Reaction Zones. *Journal of the Electrochemical Society*, 146(11):39813991, November 1999.

[18] Springer T, Zawodzinski T, and Gottesfeld S. Polymer electrolyte fuel cell model. *Journal of the Electrochemical Society*, 138(8):23342342, August 1991.

[19] Harvey D, Pharoah J, and Karan K. A comparison of different approaches to modelling the PEMFC catalyst layer. *Journal of Power Sources*, 179(1):209219, April 2008.

[20] Broka K and Ekdunge P. Modelling the PEM Fuel Cell Cathode. *Journal of Applied Electrochemistry*, 27(3):281289, March 1997.

[21] Jain P, Biegler L. T, and Jhon M. S. Optimization of Polymer Electrolyte Fuel Cell Cathodes. *Electrochemical and Solid-State Letters*, 11(10):B193B196, 2008. doi: 10.1149/1.2966289.

[22] Jain P, Biegler L. T, and Jhon M. S. Sensitivity of PEFC Models to Cathode Layer Microstructure. *Journal of The Electrochemical Society*, 157(8): B1222B1229, 2010. doi: 10.1149/1.3454725.

[23] Yoon W and Weber A. Z. Modeling Low-Platinum-Loading Effects in Fuel-Cell Catalyst Layers. *Journal of The Electrochemical Society*, 158(8):B1007B1018, 2011. doi: 10.1149/1.3597644.

[24] Secanell M, Karan K, Suleman A, and Djilali N. Multi-variable optimization of PEMFC cathodes using an agglomerate model. *Electrochimica Acta*, 52(22): 63186337, 2007. ISSN 0013-4686. doi: 10.1016/j.electacta.2007.04.028.

[25] Wang Q, Eikerling M, Song D, and Liu Z. Structure and performance of different types of agglomerates in cathode catalyst layers of PEM fuel cells . *Journal of Electroanalytical Chemistry*, 573(1):6169, 2004. ISSN 1572-6657. doi: 10.1016/j.jelechem.2004.06.022.

[26] Sadeghi E, Putz A, and Eikerling M. Hierarchical Model of Reaction Rate Distributions and Effectiveness Factors in Catalyst Layers of Polymer Electrolyte Fuel Cells. *Journal of The Electrochemical Society*, 160(10):F1159F1169, 2013. doi: 10.1149/2.090310jes.

[27] Cetinbas F. C, Advani S. G, and Prasad A. K. A Modified Agglomerate Model with Discrete Catalyst Particles for the PEM Fuel Cell Catalyst Layer. *Journal of The Electrochemical Society*, 160(8):F750F756, 2013. doi: 10.1149/2.017308jes.

[28] Iczkowski R. P and Cutlip M. B. Voltage Losses in Fuel Cell Cathodes. *Journal of The Electrochemical Society*, 127(7):14331440, 1980. doi: 10.1149/1.2129925.

[29] Sun W, Peppley B. A, and Karan K. An Improved Two-Dimensional Agglomerate Cathode Model to Study the Influence of Catalyst Layer Structural Parameters. *Electrochimica Acta*, 50(16-17):33473358, 2005.

[30] Ziegler C, Thiele S, and Zengerle R. Direct three-dimensional reconstruction of a nanoporous catalyst layer for a polymer electrolyte fuel cell. *Journal of Power Sources*, 196(4):20942097, 2011.

[31] Lange K. J, Sui P.-C, and Djilali N. Pore Scale Simulation of Transport and Electrochemical Reactions in Reconstructed PEMFC Catalyst Layers. *Journal of The Electrochemical Society*, 157(10):B1434B1442, 2010. doi: 10.1149/1.3478207.

[32] Lange K. J, Sui P.-C, and Djilali N. Determination of effective transport properties in a {PEMFC} catalyst layer using different reconstruction algorithms . *Journal of Power Sources*, 208(0):354365, 2012. ISSN 0378-7753. doi: 10.1016/j.jpowsour.2011.11.001.

[33] Matsuzaki K, Shikazono N, and Kasagi N. Three-dimensional numerical analysis of mixed ionic and electronic conducting cathode reconstructed by focused ion beam scanning electron microscope. *Journal of Power Sources*, 196(6):30733082, 2011.

[34] Litster S, Hess K, Epting W, and Gelb J. Catalyst Layer Analysis: Nanoscale X-ray CT, Spatially-Resolved In Situ Microscale Diagnostics, and Modeling. *ECS Transactions*, 41(1):409418, 2011. doi: 10.1149/1.3635575.

[35] Malek K, Eikerling M, Wang Q, Titichai N, and Liu Z. Self-organization in catalyst layers of polymer electrolyte fuel cells. *Journal of Physical Chemistry C*, 111(36):1362713634, 2007.

[36] Malek K and Franco A. A. Microstructure-based modeling of aging mechanisms in catalyst layers of polymer electrolyte fuel cells. *The Journal of Physical Chemistry B*, 115(25):80888101, 2011.

[37] Kamarajugadda S and Mazumder S. Generalized flooded agglomerate model for the cathode catalyst layer of a polymer electrolyte membrane fuel cell . *Journal of Power Sources*, 208(0):328339, 2012. ISSN 0378-7753. doi: 10.1016/j.jpowsour.2012.02.063.

[38] Weber A. Z and Newman J. Modeling Transport in Polymer-Electrolyte Fuel Cells. *Chemical Reviews*, 104(10):46794726, October 2004.

[39] Ascher U and Spiteri R. Collocation Software for Boundary Value Differential-Algebraic Equations. *SIAM Journal on Scientific Computing*, 15(4):938952, 1994. doi: 10.1137/0915056.

[40] Moore M, Wardlaw P, Dobson P, Boisvert J. J, Putz A, Spiteri R. J, and Secanell M. Understanding the Effect of Kinetic and Mass Transport Processes in Cathode

Agglomerates. *Journal of The Electrochemical Society*, 161(8):E3125E3137, 2014. doi: 10.1149/2.010408jes.

[41] Neyerlin K. C, Gu W, Jorne J, and Gasteiger H. A. Study of the Exchange Current Density for the Hydrogen Oxidation and Evolution Reactions. *Journal of the Electrochemical Society*, 154(7):B631B635, 2007.

[42] Neyerlin K. C, Gu W, Jorne J, and Gasteiger H. A. Determination of Catalyst Unique Parameters for the Oxygen Reduction Reaction in a PEMFC. *Journal of the Electrochemical Society*, 154(10):A1955A1963, 2006.

[43] Song D, Wang Q, Liu Z, Navessin T, Eikerling M, and Holdcroft S. Numerical optimization study of the catalyst layer of PEM fuel cell cathode. *Journal of Power Sources*, 126(1-2):104111, 2004.

[44] Ma S, Solterbeck C.-H, Odgaard M, and Skou E. Microscopy studies on pronton exchange membrane fuel cell electrodes with different ionomer contents. *Appl Phys A*, 96:581589, 2009.

[45] Madhusudana Rao R and Rengaswamy R. Dynamic characteristics of spherical agglomerate for study of cathode catalyst layers in proton exchange membrane fuel cells. *Journal of Power Sources*, 158:110123, 2006.

[46] Epting W. K, Gelb J, and Litster S. Resolving the Three-Dimensional Microstructure of Polymer Electrolyte Fuel Cell Electrodes using Nanometer-Scale X-ray Computed Tomography. *Advanced Functional Materials*, 22(3):555560, 2012. ISSN 1616-3028. doi: 10.1002/adfm.201101525.

[47] Islam M, Buschatz H, and Paul D. Non-equilibrium surface reactionsa factor in determining steady state diffusion flux . *Journal of Membrane Science*, 204(12): 379384, 2002. ISSN 0376-7388. doi: 10.1016/S0376-7388(02)00064-9.

[48] Suzuki T, Kudo K, and Morimoto Y. Model for investigation of oxygen transport limitation in a polymer electrolyte fuel cell. *Journal of Power Sources*, 222: 379389, 2013.

[49] Kulikovsky A. How important is oxygen transport in agglomerates in a {PEM} fuel cell catalyst layer? . *Electrochimica Acta*, 130(0):826829, 2014. ISSN 0013-4686. doi: 10.1016/j.electacta.2014.03.131.

[50] Ziegler C, Thiele S, and Zengerle R. Direct three-dimensional reconstruction of a nanoporous catalyst layer for a polymer electrolyte fuel cell. *Journal of Power Sources*, 196(4):20942097, 2011.

[51] Chan K and Eikerling M. A Pore-Scale Model of Oxygen Reduction in Ionomer-Free Catalyst Layers of PEFCs. *Journal of The Electrochemical Society*, 158(1): B18B28, 2011. doi: 10.1149/1.3505042.

[52] Karan K. Assessment of transport-limited catalyst utilization for engineering of ultra-low Pt loading polymer electrolyte fuel cell anode . *Electrochemistry Communications*, 9(4):747753, 2007. ISSN 1388-2481. doi: 10.1016/j.elecom.2006.10.057.

[53] Zhang X, Ostadi H, Jiang K, and Chen R. Reliability of the spherical agglomerate models for catalyst layer in polymer electrolyte membrane fuel cells . *Electrochimica Acta*, 133(0):475483, 2014. ISSN 0013-4686. doi: 10.1016/j.electacta.2014.04.060.

[54] Wang J, Zhang J, and Adzic R. R. Double-Trap Kinetic Equation for the Oxygen Reduction Reaction on Pt(111) in Acidic Media. *J. Phys. Chem. A*, 111: 1270212710, 2007.

[55] Moore M, Putz A, and Secanell M. Investigation of the ORR Using the Double-Trap Intrinsic Kinetic Model. *Journal of The Electrochemical Society*, 160(6): F670F681, 2013. doi: 10.1149/2.123306jes.

[56] BekkTech L. In-Plane Conductivity Testing Procedures & Results, 2007. Accessed: August 10, 2010.

[57] Ren X and Gottesfeld S. Electro-osmotic Drag of Water in Poly(perfluorosulfonic acid) Membranes. *Journal of The Electrochemical Society*, 148(1):A87A93, 2001. doi: 10.1149/1.1344521.

[58] Zawodzinski T, Davey J, Valerio J, and Gottesfeld S. The water content dependence of electro-osmotic drag in proton-conducting polymer electrolytes. *Electrochimica Acta*, 40(3):297302, 1995. cited By (since 1996)394.

[59] Motupally S, Becker A. J, and Weidner j. W. Diffusion of Water in Nafion 115 Membranes. *Journal of the Electrochemical Society*, 147(9):31713177, 2000.

[60] Iden H, Sato K, Ohma A, and Shinohara K. Relationship among Microstructure, Ionomer Property and Proton Transport in Pseudo Catalyst Layers. *Journal of The Electrochemical Society*, 158(8):B987B994, 2011.

[61] Domican K, Shukla S, Wunder F, and Secanell M. Low Loading Cathode Catalyst Layer Mathematical Modelling & Experimental Validation. Presented at the Hydrogen + Fuel Cells Congerence 2013, Vancouver, June 16-19 2013.

[62] Bruggeman D. A. G. Calculation of the various phsical constants of heterogeneous substances. I: Dielectric constants and conductivities of mixtures of isotropic substances. *Ann. Physik.*, 25:636664, 1935.

[63] Tomadakis M. M and Sotirchos S. V. Effective Knudsen diffusivities in structures of randomly overlapping fibers. *AIChE Journal*, 37(1):7486, 1991.

[64] Tomadakis M. M and Sotirchos S. V. Ordinary and Transition Regime Diffusion in Random Fiber Structures. *AIChE Journal*, 39(3):397412, 1993.

[65] Liu Y, Murphy M. W, Baker D. R, Gu W, Ji C, Jorne J, and Gasteiger H. A. Proton Conduction and Oxygen Reduction Kinetics in PEM Fuel Cell Cathodes: Effects of Ionomer-to-Carbon Ratio and Relative Humidity. *Journal of The Electrochemical Society*, 156(8):B970B980, 2009.

[66] Wang J. X, Springer T. E, and Adzic R. R. Dual-Pathway Kinetic Equation for the Hydrogen Oxidation Reaction on Pt Electrodes. *Journal of The Electrochemical Society*, 153(9):A1732A1740, 2006. doi: 10.1149/1.2218756.

[67] Moore M, Wardlaw P, Dobson P, Boisvert J. J, Putz A, Spiteri R. J, and Secanell M. Understanding the Effect of Kinetic and Mass Transport Processes in Cathode Agglomerates. *Journal of The Electrochemical Society*, 161(8):E3125E3137, 2014. doi: 10.1149/2.010408jes.

[68] A. Damjanovic M. G. Dependence of the kinetics of O2 dissolution at Pt on the conditions for adsorption of reaction intermediates. *Electrochimica Acta*. doi: 10.1016/0013-4686(70)85021-6.

[69] Sepa D, Vojnovic M, and Damjanovic A. Kinetics and mechanism of {O2} reduction at Pt {IN} alkaline solutions . *Electrochimica Acta*, 25(11):14911496, 1980. ISSN 0013-4686. doi: 10.1016/0013-4686(80)87167-2.

[70] Tashima D, Yoshitama H, Otsubo M, Maeno S, and Nagasawa Y. Evaluation of electric double layer capacitor using Ketjenblack as conductive nanofiller .

Electrochimica Acta, 56(24):89418946, 2011. ISSN 0013-4686. doi: 10.1016/j.electacta.2011.07.124.

[71] Uchida M, Aoyama Y, Eda N, and Ohta A. Investigation of the Microstructure in the Catalyst Layer and Effects of Both Perfluorosulfonate Ionomer and PTFELoaded Carbon on the Catalyst Layer of Polymer Electrolyte Fuel Cells. *Journal of The Electrochemical Society*, 142(12):41434149, 1995. doi: 10.1149/1.2048477.

[72] Uchida M, Fukuoka Y, Sugawara Y, Eda N, and Ohta A. Effects of Microstructure of Carbon Support in the Catalyst Layer on the Performance of Polymer-Electrolyte Fuel Cells. *Journal of The Electrochemical Society*, 143(7):22452252, 1996. doi: 10.1149/1.1836988.

[73] Bird R. B, Stewart W. E, and Lightfoot E. *Transport Phenomena*. J. Wiley and Sons, 2nd edition, 2002.

[74] Parthasarathy A, Srinivasan S, Appleby A. J, and Martin C. Temperature dependence of the electrode kinetics of oxygen reduction at the platinum/nafion(R) interface - a microelectrode investigation. *Journal of the Electrochemical Society*, 139(9):25302537, September 1992.

[75] Parthasarathy A, Srinivasan S, Appleby A. J, and Martin C. Pressure Dependence of the Oxygen Reduction Reaction at the Platinum Microelectrode/Nafion Interface: Electrode Kinetics and Mass Transport. *Journal of the Electrochemical Society*, 139(9):25302537, 1992.

[76] Ascher U. M and Spiteri R. J. Collocation Software for Boundary Value Differential-Algebraic Equations. *SIAM J. Sci. Comput.*, 15(4):938952, 1994. ISSN 10648275.

[77] Banham D, Feng F, Frstenhaupt T, Pei K, Ye S, and Birss V. Effect of Pt-loaded carbon support nanostructure on oxygen reduction catalysis . *Journal of Power Sources*, 196(13):54385445, 2011. ISSN 0378-7753. doi: 10.1016/j.jpowsour.2011.02.034.

[78] Banham D, Feng F, Furstenhaupt T, Ye S, and Birss V. First time investigation of Pt nanocatalysts deposited inside carbon mesopores of controlled length and diameter. *J. Mater. Chem.*, 22:71647171, 2012. doi: 10.1039/C2JM00137C.

[79] SQLITE website, May 2014.

[80] Pharoah J, Karan K, and Sun W. On effective transport coefficients in PEM fuel cell electrodes: Anisotropy of the porous transport layers. *Journal of Power Sources*, 161(1):301313, October 2006.

[81] Eikerling M, Ioselevich A, and Kornyshev A. How good are the electrodes we use in PEFC? (Understanding structure vs. performance of membrane-electrode assemblies). *Fuel Cells*, 4(3):131140, August 2004.

[82] Yu Z, Carter R. N, and Zhang J. Measurements of Pore Size Distribution, Porosity, Effective Oxygen Diffusivity, and Tortuosity of PEM Fuel Cell Electrodes. *Fuel Cells*, 12(4):557565, 2012. ISSN 1615-6854.

[83] Peron J, Mani A, Zhao X, Edwards D, Adachi M, Soboleva T, Shi Z, Xie Z, Navessin T, and Holdcroft S. Properties of Nafion NR-211 membranes for PEMFCs. *Journal of Membrane Science*, 356(1-2):4451, 2010.

[84] Modestino M. A, Paul D. K, Dishari S, Petrina S. A, Allen F. I, Hickner M. A, Karan K, Segalman R. A, and Weber A. Z. Self-assembly and transport limitations in confined nafion films. *Macromolecules*, 46:867873, 2013.

[85] Zenyuk I. V and Litster S. Spatially-Resolved Modeling of Electric Double Layers for the Oxygen Reduction Reaction in Water-Filled Platinum Electrodes. *ECS Transactions*, 58(1):2735, 2013. doi: 10.1149/05801.0027ecst.

Appendices

Appendix A: Initial Solution Framework

As mentioned in Section 2.4.2.2, convergence of numerical agglomerate solved using COLDAE is difficult, especially for high current density operating conditions. Dobson [5] also reported similar difficulties, specifically the water filled agglomerate model. In this work it was found that model convergence was strongly dependent on the initial solution. Previously Dobson [5] developed a simple initial condition strategy which created arbitrary solutions dependent on agglomerate operating conditions. A better alternative would be to use previous model solutions as future initial solutions.

Convergence issues: some explanation to reason for, sensitivity to IS

In this work a robust solution storage and retrieval infrastructure was developed. A relational database is implemented, so that model results (profiles of solution variables across a one dimensional domain) can be stored in categorized manner (by model type, parameters, and operating conditions). The database back-end is developed using the SQLite software library. SQLite is a very small, robust C library, with relatively minimal dependencies and maintenance requirements. *"SQLite is a software library that implements a self-contained, serverless, zero-configuration, transactional SQL database engine. SQLite is the most widely deployed SQL database engine in the world. The source code for SQLite is in the public domain"* [79].

The database structure, implemented in OpenFCST, consists of numerous tables containing simulation solutions and corresponding meta data. The HEAD table contains meta data detailing all stored simulation results (model name, model parameters, operating conditions), and a reference to the table where the solutions are stored.

OpenFCST manages storage and retrieval of solutions produced and requested by the numerical micro-scale models. At the start of an MEA simulation which involves the solving of numerical micro-scale models a solution is read from the database. For best convergence of the numerical model the operating conditions and model parameters of the stored solution should be as similar as possible to the operating conditions and model parameters for which the model is currently be solved. To facilitate this a tolerance based search function is used, which searches the database for simulations results calculated for similar operating conditions. For a given set of operating conditions, if a suitable solution cannot be obtained under a given tolerance it is noted, and the tolerance is expanded until a solution is obtained. When the micro-scale model successfully solves for given operating conditions it will submit the solution to the database, improving the catalogue of stored solutions. Figure 1 shows flow diagram of the initial solution storage and retrieval process from the micro-scale

objects point of view.

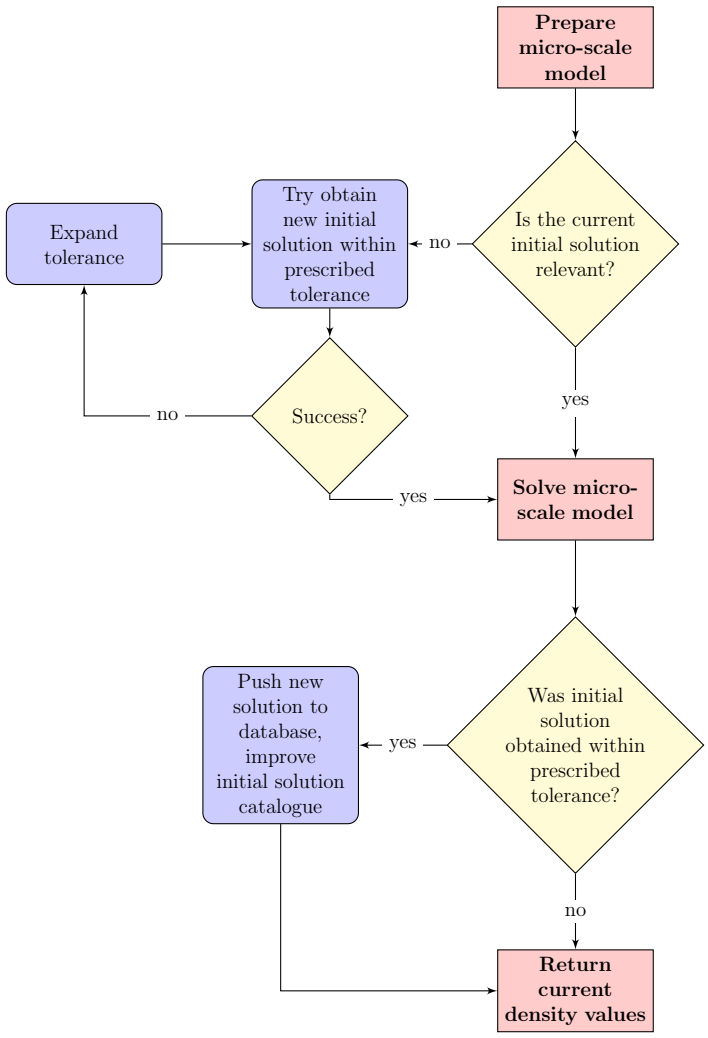

Figure 1 – Initial solution storage and retrieval frame work - from micro-scale model's perspective.

The implemented initial solution framework greatly improves micro-scale and MEA model convergences, allowing for exploration of electrochemical and mass transport phenomena at a greater range of operating conditions - demonstrated in Section 3.7. Additionally the solution storage framework is a convenient way to save micro-scale simulation results, so that they may be analyzed at a later time. The implemented framework can easily be adapted to aid future modelling.

Appendix B: Parallelization

When OpenFCST assembled the FEM LHS and RHS matrices for a multi-scale MEA simulation, the micro-scale model may be solved approximately $10^3 - 10^4$ times depending on choice of finite elements, and CL grid density. The analytical agglomerate expression (2.85) can be evaluated in approximately 200 μs, and therefore imposes relatively low requirements on said multi-scale MEA simulations. The numerical agglomerate models however are more computationally demanding, requiring approximately 1.5 ms to 1.0 s to solve. As a direct result MEA multi-scale evaluations performed using numerical agglomerate models can take *hours*, significantly slower than multi-scale simulations performed using analytical agglomerates, which take less than one *minute*.

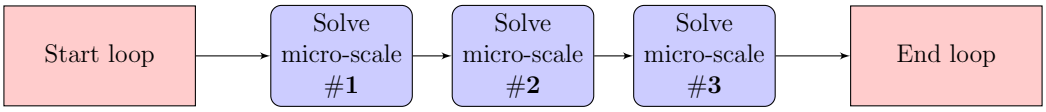

Figure 2 – Solving micro-scale objects: serial for-loop unrolled.

Time requirements associated with multi-scale evaluations performed using numerical agglomerate models hamper research efforts, therefore efforts have been made to decrease computation time. Historically OpenFCST run serially, i.e. on one processor, therefore evaluation of micro-scale models is done one by one as shown in Figure 2. In this work the multi-scale CL was improved so that evaluations of individual agglomerate models can be performed in parallel, as seen in Figure 3.

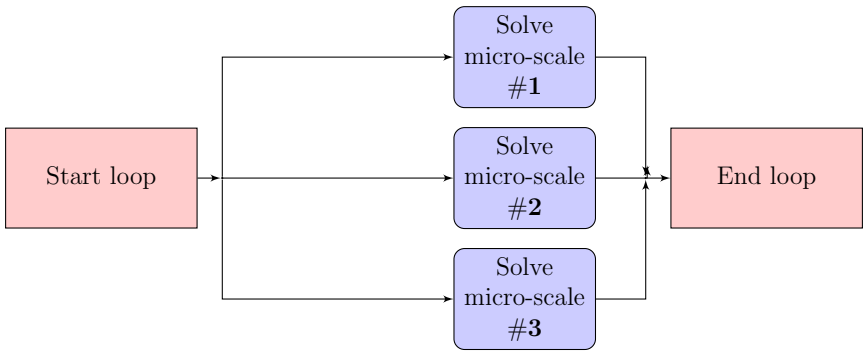

Figure 3 – Solving micro-scale objects: parallel for-loop.

Implementation of parallel micro-scale evaluations was done using OpenMP. OpenMP is multi processor API for programming languages C, C++, and FORTAN. Using OpenMP a program can be written to consist of several threads - independent serial pathways - which can be distributed over several cores of a multi core processor,

utilizing more processing power than a traditional serial program. OpenMP was appropriate for the task of paralleling FCST, as it can be used to easily adapt existing serial code, via the use of pre compiler directives. Using the *#pragma OMP Parallel* and *for* directives, amongst others, serial for loops used to evaluate multiple micro-scale models were transformed to run in parallel. Associated with parallel computing are various challenges, such as race condition. Race condition occurs when two individual threads attempt to modify the same data simultaneously, causing data corruption. To circumvent race condition, many deep copying functions were implemented in OpenFCST, which are used to ensure that the data of each micro-scale model operating in parallel remains exclussive to that model.

The theoretical speed improvement by parallelization is described using Amdahl's law:

$$S(n) = \frac{T(1)}{T(n)} = \frac{T(1)}{T(1)\left(B + \frac{1}{n}(1-B)\right)} = \frac{1}{B + \frac{1}{n}(1-B)} \tag{1}$$

where $T(n)$ is the time taken using n threads, and B is the fraction of the program that is strictly serial. As the number of threads n increases, $T(n)$ the time taken for the program to run will approach $T(1)$ B. In OpenFCST the dimension of the for loops which are parallelized is equal to 9 for second order Lagrange elements, therefore n equals 9. Numerical agglomerate models take longer than analytical agglomerates to compute, therefore for the numerical agglomerate case parallel segments $(1 - B)$ are longer. Parallel program sections are proportionally even larger when an agglomerate polydispersion is considered, since several agglomerates must be computed for each quadrature point. Therefore the greatest speed improvements will occur for the polydisperse case with numerical agglomerates, as $1 - B$ approaches 1.

Additionally the BVP solver COLDAE required modification to execute in parallel safely. Thanks to co-operation from Boisvert and Spiteri, University of Saskatchewan, COLDAE was improved using OpenMP, specifically to avoid race condition issues. Benchmarks quantifying improved performance are described in Section 3.7.